"PERFORMANCE ANALYSIS OF A HEXAGONAL PHOTONIC CRYSTAL FIBER(H-PCF) OVER A BROADBAND RANGE BY VARYING DOPING PARAMETERS"

This thesis is submitted to the Department of Electrical, Electronic and Communication Engineering (EECE) of MILITARY INSTITUTE OF SCIENCE AND TECHNOLOGY (MIST), Mirpur Cantonment, Dhaka – 1216 for partial fulfillment of the requirements for the degree of B.Sc. in Electrical, Electronic and Communication Engineering.

Submitted by

Murtaza Khan, Student ID – 201416076

Shanzida Kabir, Student ID – 201416084

Zafrin Ferdous Mira, Student ID – 201416104

Supervised by

Lt. Col. Md. Jahangir Hossain, te, sigs.

Department of Electrical, Electronic and Communication Engineering

Military Institute of Science and Technology

Mirpur Cantonment, Dhaka – 1216

Department of Electrical, Electronic and Communication Engineering (EECE)

MILITARY INSTITUTE OF SCIENCE AND TECHNOLOGY

Mirpur Cantonment, Dhaka – 1216.

December 2017

APPROVAL PAGE

This thesis paper titled **"Performance Analysis of a Hexagonal Photonic Crystal Fiber (H-PCF) over a broadband range by varying doping parameters"** is submitted by the group as mentioned below has been accepted as satisfactory and met the required standard in partial fulfillment of the requirement for the degree of B.Sc. in Electrical, Electronic and Communication Engineering on December 2017.

Group Members:

Murtaza Khan

Shanzida Kabir

Zafrin Ferdous Mira

SUPERVISOR:

Lt. Col. Md. Jahangir Hossain, te, sigs.
Department of Electrical Electronic and Communication Engineering (EECE)
Military Institute of Science and Technology (MIST)

DEC LA R ATI ON

It is hereby declared that the work presented in this thesis titled "P erformance Anal ysis of a Hexagonal Photonic Cr ystal Fiber (H -PCF) over a broadband range by varying doping parameters" is an outcome of the study carried out by the author under the supervision of Lt. Col. Md. Jahangir Hossain, te, sigs. It is also declared that neither of this thesis paper nor any part therefore has been submitted anywhere else for the award of any degree, diploma or other qualifications.

AUTHORS:

Murtaza

Murtaza khan
Student ID: 201416076

Shanzida

Shanzida Kabir
Student ID: 201416084

Zafrin ferdous Mira

Zafrin Ferdous Mira
Student ID: 201416104

ACKNOWLEDGEMENT

ABSTRACT

This thesis paper presents a novel design of a hexagonal four ring photonic crystal fiber (H-PCF) and its performance for different parameter such as effective mode index, dispersion, effective mode area and non-linearity parameter. COMSOL Multi-physics 4.3 software is used to design and analyze the parameters of H-PCF. The designed H-PCF consists of four layered circular air holes and gradually decreasing refractive index from core to cladding. Doping materials, doping percentage and wavelength are varied to analyze the characteristics of the designed H-PCF. MATLAB 7.6 is used to plot the simulation results. The values of Dispersion, Effective mode index, Effective mode area and Non-linearity parameter are calculated from standard equations and plotted against the wavelength. Nearly flattened dispersion is found for a wide range of wavelength from 1410 nm to 1610 nm for GeO_2 doped silica at 30% doping and for BaF_2 doped silica at 10% doping. An increasing effective mode index of value 1.4038 to 1.4401 is found by varying doping percentage of GeO_2 doped silica and an increasing effective mode index of 1.4038 to 1.4087 is found by varying doping percentage of BaF_2 doped silica which is important for light confinement and total internal reflection. The proposed H-PCF shows nearly zero dispersion and don't display flattened range of dispersion when not doped. But when the model is doped with GeO_2 and BaF_2, then it offers flattened dispersion for a wide range of wavelength from 1410 nm to 1610 nm. Though the effective mode area of the model decreases with increasing doping percentage, but it is in the acceptable range of fiber optic communication. Increasing non-linear parameter from 14.31 $W^{-1}Km^{-1}$ to 27.98 $W^{-1}Km^{-1}$ can be found by varying doping percentage for GeO_2 doping and from 13.5 $W^{-1}Km^{-1}$ to 18.91 $W^{-1}Km^{-1}$ for BaF_2 doping. When the loss parameters of the proposed H-PCF are compared for both type of doping, it is found that for the same percentage of doping concentration, value of effective mode area is higher for BaF_2 doped silica than GeO_2 doped silica and nonlinearity parameter is higher for GeO_2 doping than BaF_2 doping. Increase of effective mode index is higher for GeO_2 doping than BaF_2 doping. In summary, it can be said that the proposed H-PCF displays good performance in terms of effective mode index, effective mode area, non-linear parameter, dispersion etc. with doping of GeO_2 and BaF_2, which is important for optical communication.

TABLE OF CONTENTS

Contents   **Page No**

LIST OF FIGURES

LIST OF TABLES

LISTOF SYMBOLS

A_{eff}	effective mode area
B	birefringence
$D(\lambda)$	chromatic dispersion
a	elliptical core's semi major axis
b	elliptical core's semi minor axis
$\vec{D}$	electric displacement vector
d	diameter of air hole
$\vec{G}$	any vector of the reciprocal lattice
J_{free}	free current
k_0	free space wave number
L_C	confinement loss
$\vec{R}$	lattice vector
$\vec{r}$	spatial vector
X	concentration of doping
β	wave propagation constant
γ	non linear parameter
Δ	relative refractive index difference
n_{eff}	effective refractive index
η_x	refractive index along the x-axis
η_y	refractive index along the y-axis
Λ	pitch

LIST OF ABBREVIATIONS

APD	avalanche photodiode
EMI	electromagnetic interference
EMPs	electromagnetic pulses
FEM	finite element method
FTTH	fiber-to-the-home
FTTP	Fiber-to-the-premise
H-PCF	Hexagonal photonic crystal fibers
LAN	local area network
LASER	light amplification by stimulated emission of radiation
LED	light-emitting diode
MMF	multi mode fiber
NA	numerical aperture
PBG	photonic band-gap
PCF	photonic crystal fibers
PML	perfectly matched layer
RF	radio frequency
SMF	single mode fiber
SNR	signal-to-noise ratio
THz	terahertz

CHAPTER 1

INTRODUCTION

1.1   Introduction

A communication system transmits and receives information from one place to another, whether separated by a few kilometers or by transoceanic distances. Information is often carried over an electromagnetic carrier wave whose frequency can vary from a few megahertz to several hundred terahertz's. Optical fiber can handle all these frequencies most efficiently being a wired means of communication among all the most frequently used transmission media. Broadband optical transmission with wavelength division multiplexing technique is effective for large capacity networks, and optical fibers are widely used as optical signal transmission media.

Fiber-optic communication is a method of transmitting information from one place to another by sending pulses of light through an optical fiber [1]. The light forms an electromagnetic carrier wave that is modulated to carry information.

Modern fiber-optic communication systems generally include an optical transmitter to convert an electrical signal into an optical signal to send into the optical fiber, a cable containing bundles of multiple optical fibers that is routed through underground conduits and buildings, multiple kinds of amplifiers, and an optical receiver to recover the signal as an electrical signal. The information transmitted is typically digital information generated by computers, telephone systems, and cable television companies [2].

Optical fiber is used by many telecommunications companies to transmit telephone signals, internet communication, and cable television signals [3]. Nevertheless, most of the data rates are wrapped below gigabit per second (Gb/s) primarily due to the lack of the available spectrum in the RF (radio frequency) microwave range.

In contrast, due to the enormous bandwidth over several terahertz's (THz) in the second window, the light wave systems can provide an amazing capacity of 100 Tb/s and beyond. In fact, the optical communication systems, or fiber-optic systems in particular, have become indispensable as the backbone of the modern-day information infrastructure. While initial deployment of optical fiber was mainly for long-haul or submarine transmission, light wave systems are currently in almost all metro networks. Fiber-to-the-

premise (FTTP) and fiber-to-the-home (FTTH) are being considered seriously in most parts of the world right now [4].

Optical communication systems have been deployed worldwide since 1980 and have indeed revolutionized the technology behind telecommunications. Indeed, the light wave technology, together with microelectronics, is believed to be a major factor in the advent of the information age.

1.2   Fiber Optic Communication System
1.2.1   The General Concept

An optical fiber communication system is similar in basic concept to any type of communication system. A block schematic of a general communication system is shown in Fig. 1.1, the function of which is to convey the signal from the information source over the transmission medium to the destination.
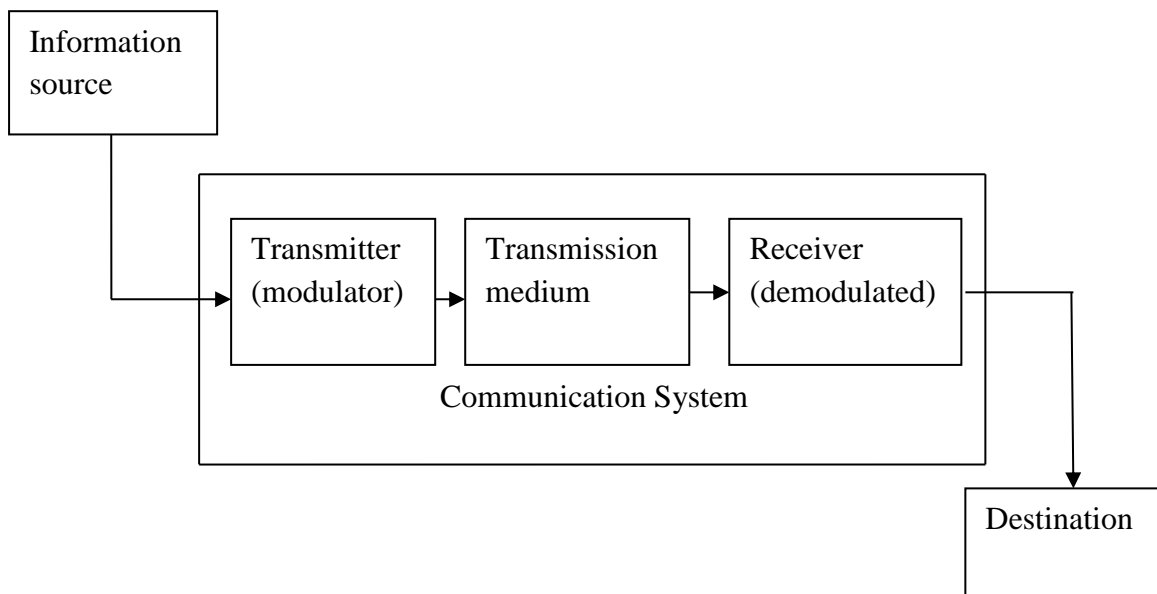
Fig. 1.1: The general communication system. [2]

The communication system therefore consists of a transmitter or modulator linked to the information source, the transmission medium and a receiver or demodulator at the destination point. In electrical communications the information source provides an electrical signal, usually derived from a message signal which is not electrical (e.g. sound), to a transmitter comprising electrical and electronic components which converts the signal into a suitable form for propagation over the transmission medium. For optical fiber

2

communications the system shown in Fig. 1.1 may be considered in slightly greater detail, as given in Fig. 1.2.

```
┌──────────────┐   ┌──────────────┐   ┌──────────────┐   ┌──────────────┐
│ Informatio   │→ │ Electrical   │→ │ Optical      │→ │ Optical      │
│ n source     │   │ transmit     │   │ source       │   │ fiber cable  │
└──────────────┘   └──────────────┘   └──────────────┘   └──────────────┘

        ┌──────────────┐   ┌──────────────┐        ┌──────────────┐
        │ Optical      │→ │ Electrical   │→       │ Destination  │
        │ detector     │   │ receiver     │        │              │
        └──────────────┘   └──────────────┘        └──────────────┘
```
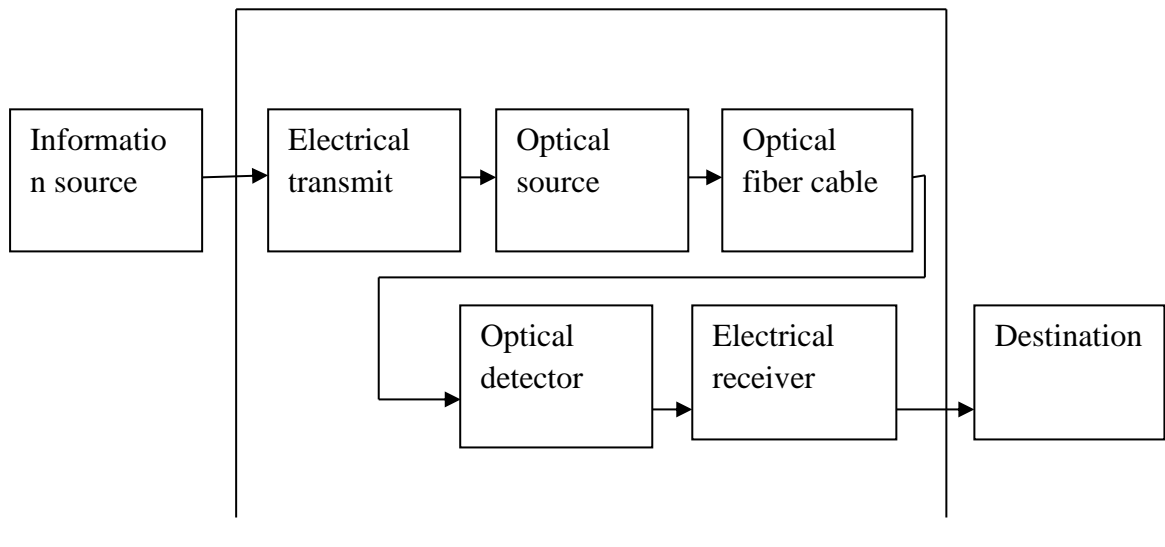
Fig. 1.2: The optical fiber communication system [2]

In this case the information source provides an electrical signal to a transmitter comprising an electrical stage which drives an optical source to give modulation of the light wave carrier. The optical source which provides the electrical–optical conversion may be either a semiconductor laser or light-emitting diode (LED). The transmission medium consists of an optical fiber cable and the receiver consists of an optical detector which drives a further electrical stage and hence provides demodulation of the optical carrier.

The optical carrier may be modulated using either an analog or digital information signal. In the system shown in Fig. 1.2, analog modulation involves the variation of the light, emitted from the optical source in a continuous manner. With digital modulation, however, discrete changes in the light intensity are obtained (i.e. on–off pulses). Although often simpler to implement, analog modulation with an optical fiber communication system is less efficient, requiring a far higher signal-to-noise ratio (SNR) at the receiver than digital modulation. Also, the linearity needed for analog modulation is not always provided by semiconductor optical sources, specially at high modulation frequencies. For these reasons, analog optical fiber communication links are generally limited to shorter distances and lower bandwidth operation than digital links.

Fig. 1.3 shows a block schematic of a typical digital optical fiber link. Initially, the input digital signal from the information source is suitably encoded for optical transmission.
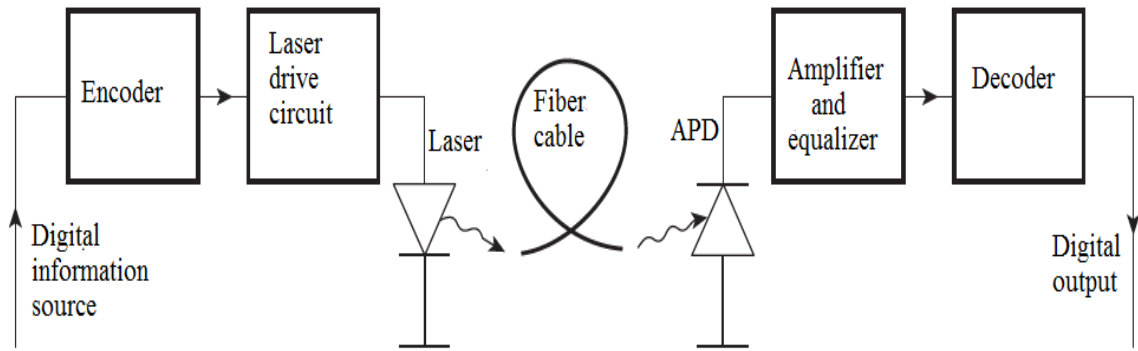
Fig. 1.3: A digital optical fiber link using a semiconductor laser source and an avalanche photodiode (APD) detector [2]

The laser drive circuit directly modulates the intensity of the semiconductor laser with the encoded digital signal. Hence a digital optical signal is launched into the optical fiber cable. The avalanche photodiode (APD) detector is followed by a front-end amplifier and equalizer or filter to provide gain as well as linear signal processing and noise bandwidth reduction. Finally, the signal obtained is decoded to give the original digital information.

1.2.2 Advantages of Optical Fiber Communication

Communication using an optical carrier wave guided along a glass fiber has a number of extremely attractive features, several of which were apparent when the technique was originally conceived. Furthermore, the advances in the technology have surpassed even the most optimistic predictions, creating additional advantages.

I. **Enormous Potential Bandwidth**: The optical carrier frequency in the range 1013 to 1016 Hz. It yields a far greater potential transmission bandwidth than metallic cable systems or even millimeter wave radio systems. Indeed, by the year 2000 the typical bandwidth multiplied by length product for an optical fiber link incorporating fiber amplifiers was 5000 GHz km. Hence at this time optical fiber was already demonstrating a factor of 50,000 bandwidth improvement over coaxial cable while also providing this superior information-carrying capacity over much longer transmission distances [5].

II. **Small Size and Weight:** Optical fibers have very small diameters which are often no greater than the diameter of a human hair. Hence, even when such fibers are covered with protective coatings they are far smaller and much lighter than

corresponding copper cables. This is a tremendous boon towards the alleviation of duct congestion in cities, as well as allowing for an expansion of signal transmission within mobiles such as aircraft, satellites and even ships.

III. **Electrical Isolation:** Optical fibers which are fabricated from glass, or sometimes a plastic polymer, are electrical insulators and therefore, unlike their metallic counterparts, they do not exhibit earth loop and interface problems. Furthermore, this property makes optical fiber transmission ideally suited for communication in electrically hazardous environments as the fibers create no arcing or spark hazard at abrasions or short circuits.

IV. **Immunity to Interference and Crosstalk:** Optical fibers form a dielectric waveguide and are therefore free from electromagnetic interference (EMI), radio-frequency interference (RFI), or switching transients giving electromagnetic pulses (EMPs). Hence the operation of an optical fiber communication system is unaffected by transmission through an electrically noisy environment and the fiber cable requires no shielding from EMI. The fiber cable is also not susceptible to lightning strikes if used overhead rather than underground.

V. **Signal Security:** The light from optical fibers does not radiate significantly and therefore they provide a high degree of signal security. Unlike the situation with copper cables, a transmitted optical signal cannot be obtained from a fiber in a noninvasive manner. Therefore, in theory, any attempt to acquire a message signal transmitted optically may be detected. This feature is obviously attractive for military, banking and general data transmission applications.

VI. **Low Transmission Loss:** The development of optical fibers over the last 20 years has resulted in the production of optical fiber cables which exhibit very low attenuation or transmission loss in comparison with the best copper conductors. Fibers have been fabricated with losses as low as 0.15 dB km^{-1} and this feature has become a major advantage of optical fiber communications. It facilitates the implementation of communication links with extremely wide optical repeater or amplifier spacing. Thus, reducing both system cost and complexity.

VII. **Ruggedness and Flexibility:** Although protective coatings are essential, optical fibers may be manufactured with very high tensile strengths. Furthermore, cable

structures have been developed which have proved flexible, compact and extremely rugged. Taking the size and weight advantage into account, these optical fiber cables are generally superior in terms of storage, transportation, handling and installation to corresponding copper cables, while exhibiting at least comparable strength and durability.

VIII. **System Reliability and Ease of Maintenance:** These features primarily stem from the low-loss property of optical fiber cables which reduces the requirement for intermediate repeaters or line amplifiers to boost the transmitted signal strength. Hence with fewer optical repeaters or amplifiers, system reliability is generally enhanced in comparison with conventional electrical conductor systems. Both these factors also tend to reduce maintenance time and costs.

IX. **Potential Low Cost:** The glass which generally provides the optical fiber transmission medium is made from sand – not a scarce resource. So, in comparison with copper conductors, optical fibers offer the potential for low-cost line communication. Although over recent years this potential has largely been realized in the costs of the optical fiber transmission medium which for bulk purchases has become competitive with copper wires, it has not yet been achieved in all the other component areas associated with optical fiber communications.

1.3   Fiber Optic Technology

1.3.1   Construction of Fiber Optics

The transmission of light via a dielectric waveguide structure was first proposed and investigated at the beginning of the twentieth century. Fiber optic cables carry communication signals using pulses of light generated by small lasers or light-emitting diodes (LEDs).

The cable consists of one or more strands of glass, each only slightly thicker than a human hair. The center of each strand is called the core, which provides the pathway for light to travel.
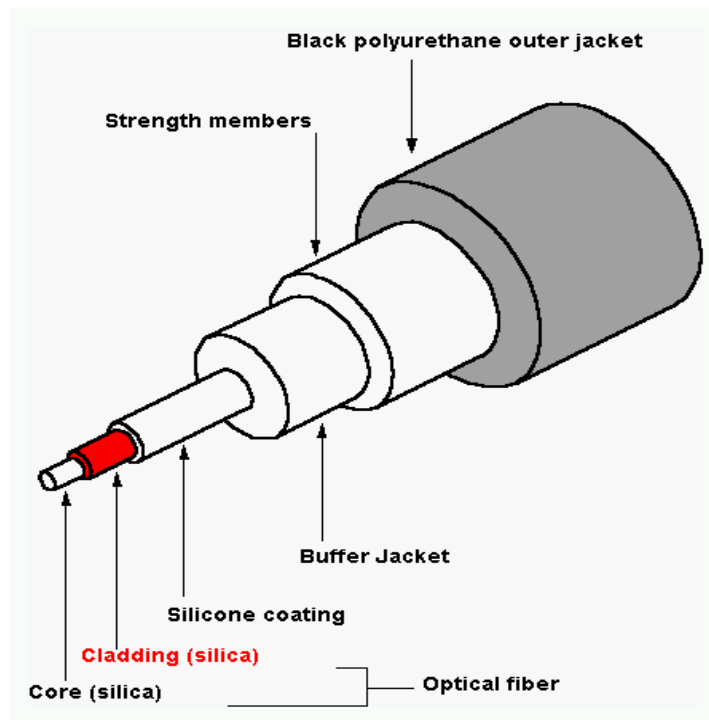
Fig. 1.4: Various parts of optical fiber

The core is surrounded by a layer of glass called cladding that reflects light inward to avoid loss of signal and allow the light to pass through bends in the cable.

1.3.2 Different Types of Optical Fiber

The two primary types of fiber optics are called single mode fiber (SMF) and multi-mode fiber (MMF). Single mode fiber uses very thin glass strands and a laser to generate light while multi-mode fibers use (light emitting diodes) LEDs.

MMF support many propagation paths or transverse modes while SMF support a single mode. MMFs generally have a wider core diameter and are used for short-distance communication links and for applications where high power must be transmitted. Single-mode fibers are used for most communication links longer than 1,000 meters. Again, MMFs can be divided into step index and graded index fibers.

In the first case the refractive index of the core is uniform throughout and undergoes an abrupt change at the cladding boundary. This is called a step-index fiber. In the second case the core refractive index is made to vary as a function of the radial distance from the center of the fiber. This type is a graded index fiber. Multimode Step index fiber is

suitable for short distance (endoscope). Multimode graded index suitable for medium distance (LAN-local area network).
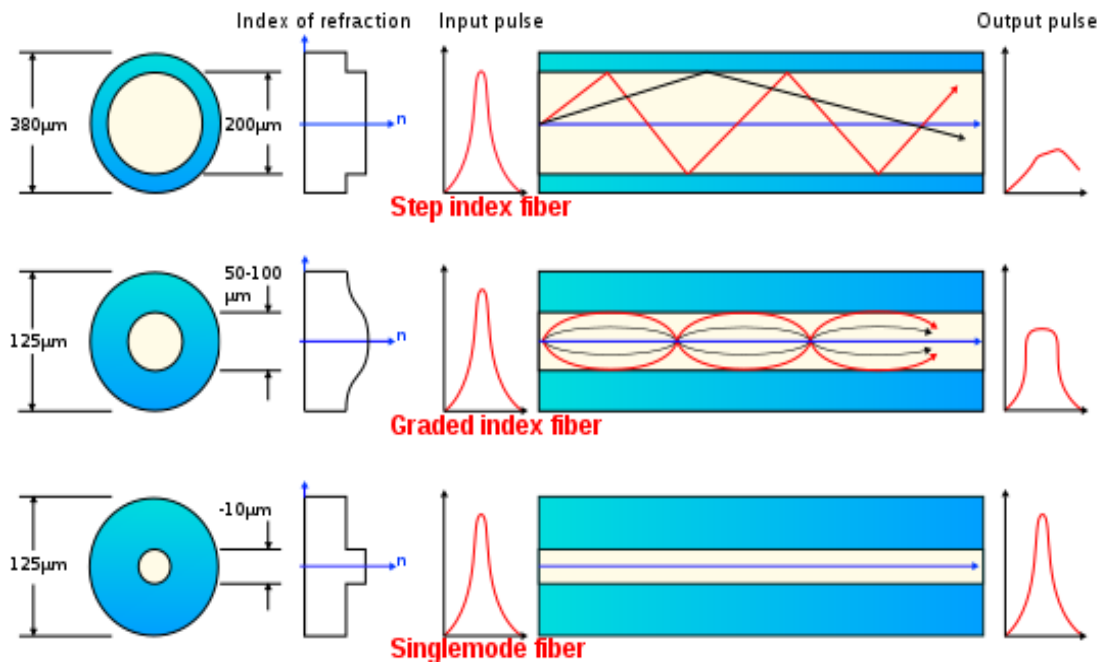
Fig. 1.5: Comparison of multi-mode (step index and graded index) and single-mode optical fiber [3]

1.3.3   Light Propagation Through Fiber Optic

1.3.3.1 Total Internal Reflection

When a light ray encounters a boundary separating two different media, part of ray is reflected back into the first medium and the remainder is bent (or refracted) as it enters the second material.

This is shown in Fig. 1.4 where $n_2 < n_1$. It may be observed that the ray approaching the interface is propagating in a dielectric of refractive index n_1 and is at an angle φ_1 to the normal at the surface of the interface. If the dielectric on the other side of the interface has a refractive index n_2 which is less than n_1, then the refraction is such that the ray path in this lower index medium is at an angle φ_1 to the normal, where φ_2 is greater than φ_1.

The angles of incidence φ_1 and angle of refraction φ_2 are related to each other and to the refractive indices of the dielectrics by Snell's law of refraction.

Reflection law: Angle of incidence= Angle of reflection

According to Snell's law,

$$n_1 \sin \varphi_1 = n_2 \sin \varphi_2 \qquad (1.1a)$$

It must also be noted that the light transmission illustrated in Fig. 1.6 assumes a perfect fiber. Any discontinuities or imperfections at the core–cladding interface would probably result in refraction rather than total internal reflection, with the subsequent loss of the light ray into the cladding.
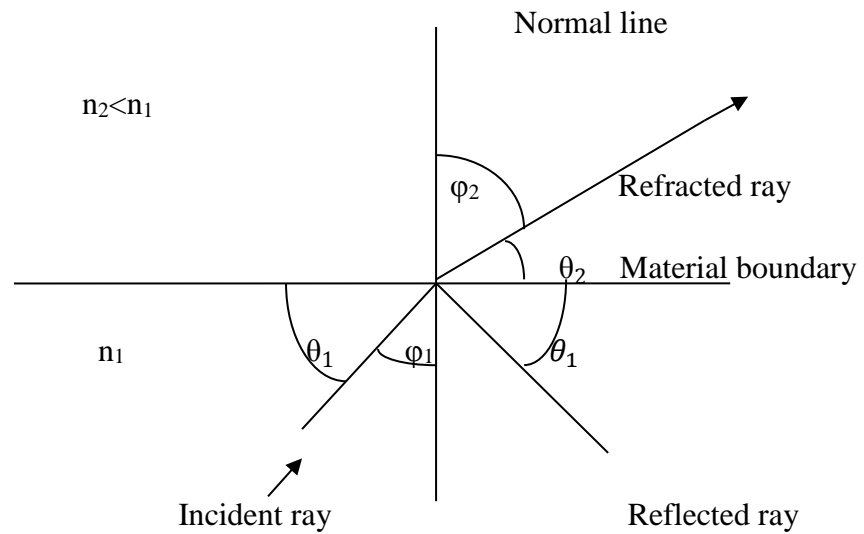
Fig. 1.6: Refraction and reflection of a light ray at a material boundary [3]

Light wave travelling in a denser medium strikes a less dense medium. Depending on the incidence angle with respect to φ_c, which is determined by the ratio of the refractive indices, the wave may be transmitted (refracted) or reflected. It may also be observed in Fig. 1.7(a) that a small amount of light is reflected back into the originating dielectric medium (partial internal reflection). As n_1 is greater than n_2, the angle of refraction is always greater than the angle of incidence. Thus, when the angle of refraction is 90° and the refracted ray emerges parallel to the interface between the dielectrics, the angle of incidence must be less than 90°. This is the limiting case of refraction and the angle of incidence is now known as the critical angle φ_c, as shown in Fig. 1.7(b).

$$\sin \varphi_c = \frac{n_2}{n_1} \quad \text{(Snell's Law)} \qquad (1.1b)$$
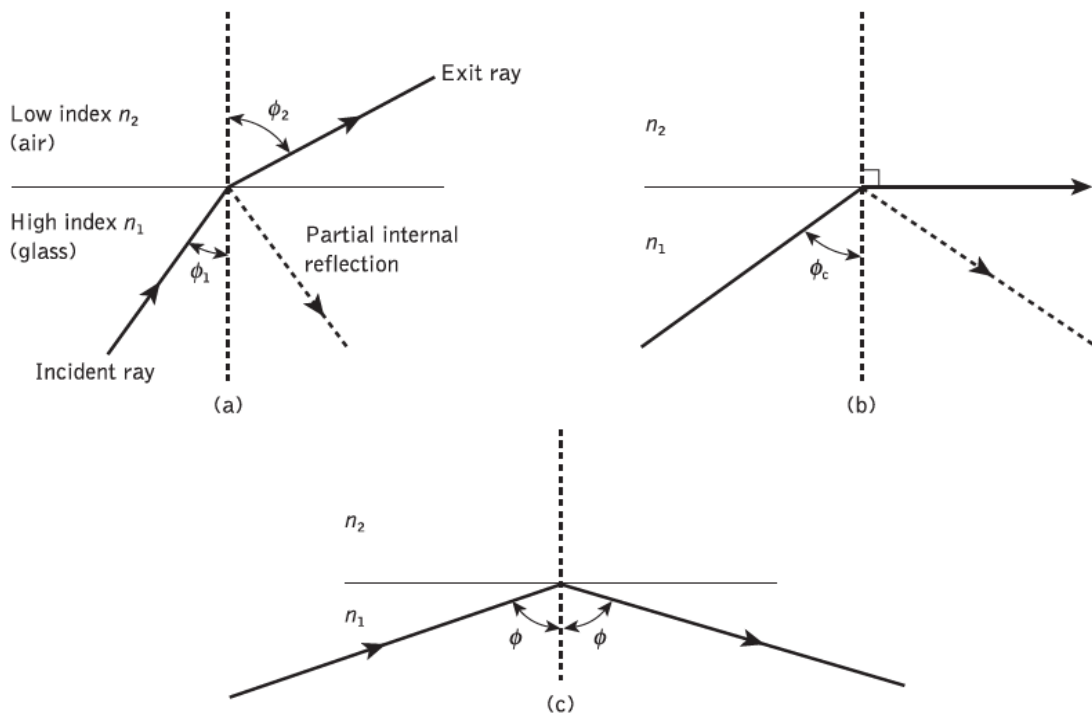
Fig. 1.7: Light rays incident on a high to low refractive index interface (e.g. glass–air): (a) refraction; (b) the limiting case of refraction showing the critical ray at an angle φ_c ; (c) total internal reflection where $\varphi > \varphi_c$ [2]

At angles of incidence greater than the critical angle the light is reflected back into the originating dielectric medium (total internal reflection) with high efficiency (around 99.9%). Hence, it may be observed in Fig. 1.7(c) that total internal reflection occurs at the interface between two dielectrics of differing refractive indices when light is incident on the dielectric of lower index from the dielectric of higher index, and the angle of incidence of the ray exceeds the critical value. This is the mechanism by which light at a sufficiently shallow angle (less than $90° - \varphi_c$) may be considered to propagate down an optical fiber with low loss.

1.3.3.2   Acceptance Angle

Since only rays with a sufficiently shallow grazing angle (i.e. with an angle to the normal greater than φ_c) at the core–cladding interface are transmitted by total internal reflection, it is clear that not all rays entering the fiber core will continue to be propagated down its length. The geometry concerned with launching a light ray into an optical fiber is shown in Fig. 1.8, which illustrates a meridional ray A at the critical angle φ_c within the fiber at the core–cladding interface.
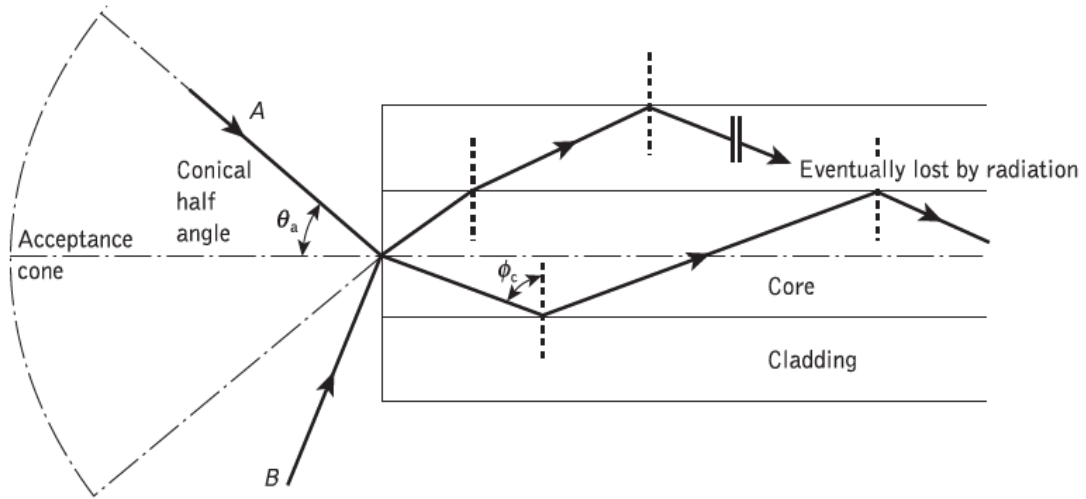
Fig. 1.8: The acceptance angle θ_a when launching light into an optical fiber [2]

It may be observed that this ray enters the fiber core at an angle θ_a to the fiber axis and is refracted at the air–core interface before transmission to the core–cladding interface at the critical angle.

Hence, any rays which are incident into the fiber core at an angle greater than θ_a will be transmitted to the core–cladding interface at an angle less than φ_c, and will not be totally internally reflected. This situation is also illustrated in Fig. 1.8, where the incident ray B at an angle greater than θ_a is refracted into the cladding and eventually lost by radiation. Thus, for rays to be transmitted by total internal reflection within the fiber core they must be incident on the fiber core within an acceptance cone defined by the conical half angle θ_a. Hence θ_a is the maximum angle to the axis at which light may enter the fiber in order to be propagated, and is often referred to as the acceptance angle for the fiber.

1.3.3.3 Numerical Aperture

Numerical aperture (NA) is a relative measurement of how much light a fiber can gather. Fig. 1.9 shows a light ray incident on the fiber core at an angle θ_1 to the fiber axis which is less than the acceptance angle for the fiber θ_a.
NA is expressed as a result of Snell's law.

$$NA = (n_1^2 - n_2^2)^{\frac{1}{2}} = n_0 \sin \theta a \qquad (1.2a)$$

11
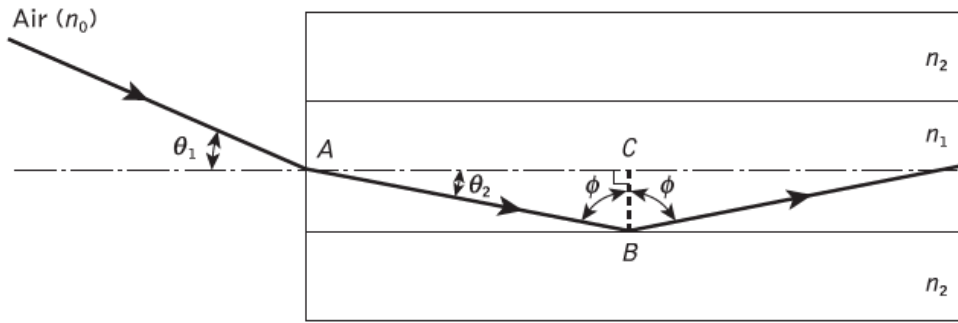
Fig. 1.9: The ray path for a meridional ray launched into an optical fiber in air at an input angle less than the acceptance angle for the fiber [2]

The ray enters the fiber from a medium (air) of refractive index n_0, and the fiber core has a refractive index n_1, which is slightly greater than the cladding refractive index n_2. The NA may also be given in terms of the relative refractive index difference Δ between the core and the cladding which is defined as:

$$NA = n_1 (2\Delta)^{\frac{1}{2}} \qquad (1.2b)$$

1.3.4 Skew Rays

Skew rays are not confined to a single plane, but instead tend to follow a helical type path along the fiber. These rays are more difficult to track as they travel along the fiber.
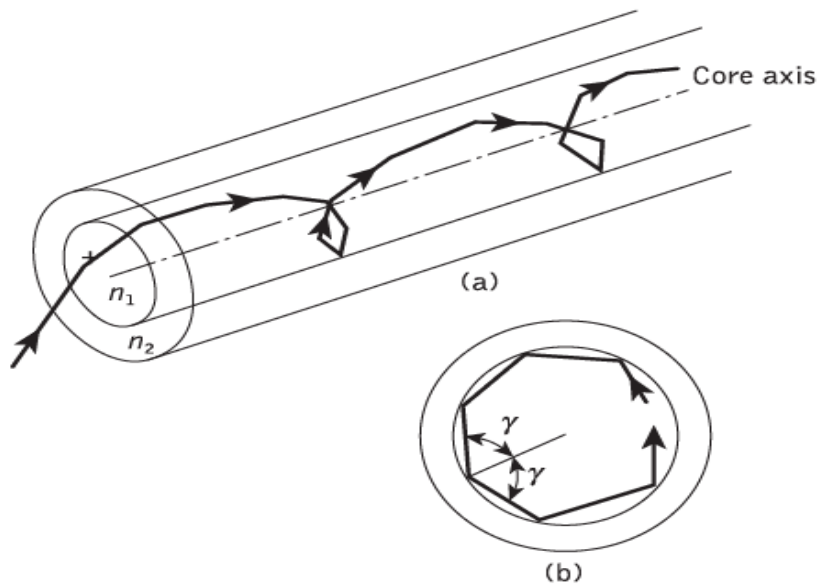
Fig. 1.10: The helical path taken by a skew ray in an optical fiber: (a) skew ray path down the fiber; (b) cross-sectional view of the fiber [2]

It is not easy to visualize the skew ray paths in two dimensions but it may be observed from Fig. 1.10(b) that the helical path traced through the fiber gives a change in direction of 2γ at each reflection, where γ is the angle between the projection of the ray in two dimensions and the radius of the fiber core at the point of reflection.

When the light input to the fiber is non-uniform, skew rays will therefore tend to have a smoothing effect on the distribution of the light as it is transmitted giving a more uniform output. The amount of smoothing is dependent on the number of reflections encountered by the skew rays.

1.4. Optical Transmission Windows

Optical fibers are replacing copper wires to become an important transmission medium. Optical fibers offer over 1,000 times as much bandwidth as a copper wire and can support transmission at gigabits per second.
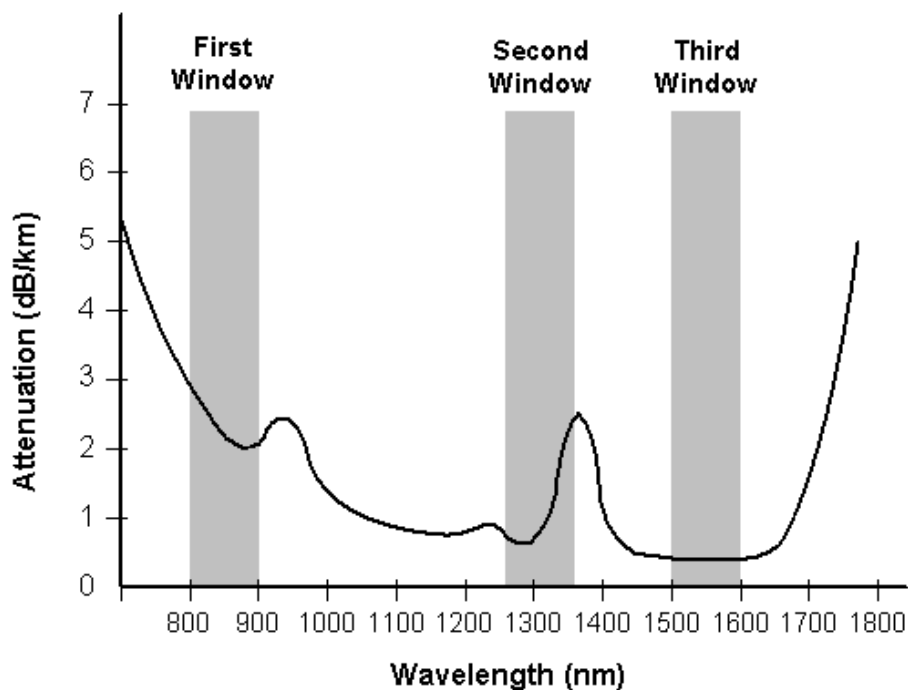
Fig. 1.11: Transmission windows of optical fiber communication system [3]

From Fig. 1.11 and table 1.1, infrared light with wavelengths of 850 nm, 1,310 nm and 1,550 nm is mostly used. Therefore, the most common devices used as the light source in optical transmitters are the Light Emitting Diode (LED) and the Laser Diode (LD). They operate in the infrared radiation (750 nm to 1mm) of the electromagnetic spectrum so that their light output is usually invisible to the human eye.

	Windows Range	Operating Wavelength
First Window	800 nm - 900 nm	850 nm
Second Window	1,260 nm - 1,360 nm	1.310 nm
Third Window	1,500 nm – 1,600 nm	1,550 nm

Table 1.1: Optical transmission window

1.5. Photonic Crystal Fiber (PCF)

1.5.1. Structure of PCF

Photonic Crystal Fibers (PCFs) are a special class of optical fibers with a significant dielectric layout, which incorporates unique optical properties [6]. They are also known as holey fibers, hole-assisted fibers or microstructure fibers. It has a central core in which the light is guided, embedded in an outer cladding of slightly lower refractive index. PCFs are a new class of optical fibers. Combining properties of optical fibers and photonic crystals they possess a series of unique properties impossible to achieve in classical fibers.
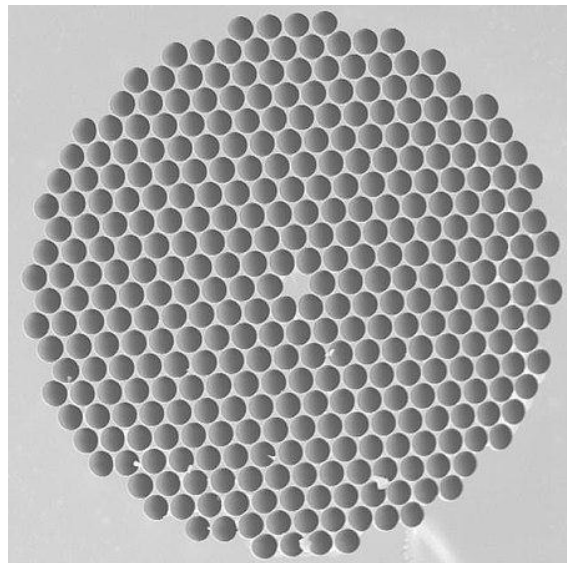
Fig. 1.12: Microscopic view of a photonic crystal fiber (PCF) [6]

PCFs are constructed using one of two basic design types, containing either a solid or hollow core.

- **Solid core PCF:** Solid core PCFs generally have higher refractive index for the core compared to the cladding. It has more degrees of freedom in the fiber design namely, the hole diameter, distance between the center of two adjacent holes, hole location and

refractive index of solid medium which ultimately result in various novel properties of the fiber. Because of the presence of holes in the cladding, the index contrast between core and cladding increases which is unimaginable in conventional fiber.

- **Hollow core PCF:** Hollow core fibers guide light in a hollow core that is surrounded by a micro-structured cladding. Unique features of hollow-core fibers include small nonlinearities, low light loss, and the option to fill air cores with gases and liquids.

(a)　　　　　　　　　　　　　　　　**(b)**
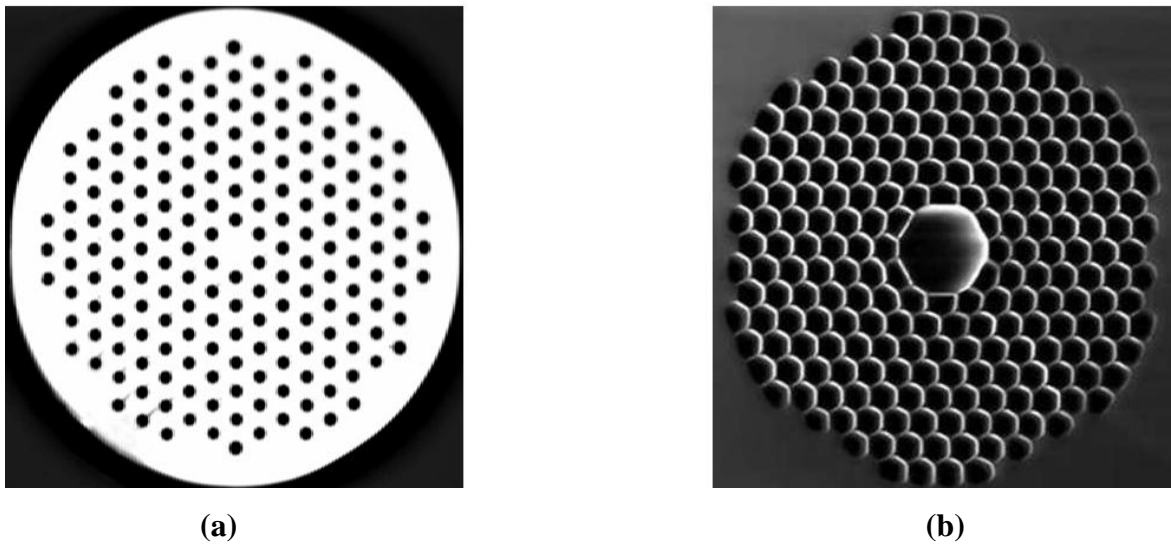
Fig. 1.13: Solid-core (a) and hollow-core (b) fiber [7]

The design of PCFs is very flexible. There are several parameters to manipulate: lattice pitch, air hole shape and diameter, refractive index of the glass, and type of lattice. All the propagation characteristics such as effective mode index, confinement loss, chromatic dispersion, mode field diameter is measured by varying the structural parameters (like-hole diameter, lattice pitch, doping etc.) by researchers around the globe [7].

1.5.3. History of PCF

Optical fibers were discovered in the 1970s and are now the backbone of telecommunication systems due to the large amount of information they can carry. Specially designed optical fibers are also used for a variety of other applications, including sensors, fiber lasers, medicine, illumination and much more. A short overview of PCF development is presented in the Table 1.2 [8].

1978	Idea of the Bragg fiber
1992	Idea of the photonic crystal fiber with air
1996	Fabrication of a single-mode fiber with photonic coating
1997	Endlessly single mode PCF
1999	PCF with photonic band-gap and air core
2000	Highly birefringent PCF
2000	Supercontinuum generation with PCF
2001	Fabrication of a Bragg fiber
2001	PCF laser with double cladding
2002	PCF with ultra-flattened dispersion
2003	Bragg fiber with silica and air core

Table 1.2: Overview of photonic crystal fibers development.

1.5.2. Different Types of PCF

Although the principles of guidance and the characteristics of index-guided PCFs are similar to those of conventional fiber, there is greater index contrast since the cladding contains air holes with a refractive index 1 in comparison with the normal silica cladding index of 1.457 which is close to the germanium-doped core index of 1.462. A fundamental physical difference, however, between index-guided PCFs and conventional fibers arises from the manner in which the guided mode interacts with the cladding region [2].

- **Index-guided microstructures:** A fundamental physical difference, however, between index-guided PCFs and conventional fibers arises from the manner in which the guided mode interacts with the cladding region. Whereas in a conventional fiber this interaction is largely first order and independent of wavelength, the large index contrast combined with the small structure dimensions cause the effective cladding index to be a strong function of wavelength.

  For short wavelengths the effective cladding index is only slightly lower than the core index and hence they remain tightly confined to the core. At longer wavelengths, however, the mode samples more of the cladding and the effective index contrast is larger. This wavelength dependence results in a large number of unusual optical properties which can be tailored.

16

Fig. 1.14: Two index-guided photonic crystal fiber structures. The dark areas are air holes while the white areas are silica [2]

- **Photonic band-gap fibers:** Photonic band-gap (PBG) fibers are a class of micro-structured fiber in which a periodic arrangement of air holes is required to ensure guidance. This periodic arrangement of cladding air holes provides for the formation of a photonic band-gap in the transverse plane of the fiber.

(a)   (b)

Fig. 1.15: Photonic band-gap (PBG) fiber structures in which the dark areas are air (lower refractive index) and the lighter area is the higher refractive index: (a) honeycomb PBG fiber; (b) air-guiding PBG fiber [2]

Two important PBG fiber structures are displayed in Fig. 1.15. The honeycomb fiber design shown in Fig. 1.15(a) was the first PBG fiber. A triangular array of air holes of sufficient size as displayed in Fig. 1.15(b). In this case a large hollow core has been defined by removing the silica around seven air holes in the center of the structure [9].

1.5. Study of Previous References

In the recent time PCF has drawn attention of many researchers for research purpose. For the advantage of flexibility in design PCF has become popular in optical fiber communication system.

The paper [4], by Abraham et.al an overview of PON (passive optical network) standards is provided, along with a discussion of video delivery over a PON network.

In the journal [5], Gambling mainly focused on the evolution of optical fiber. It gives us the idea how during the second half of the 20th Century there were several technological revolutions.

In paper [6], an all-silica optical fiber was made by embedding a central core in a two-dimensional photonic crystal with a micrometer-spaced hexagonal array of air holes. In this paper by Birks et.al an effective-index model confirmed that such a fiber can be single mode for any wavelength.

In paper [7], Richard Ramsay explained different characteristics PCF and benefits of them. Advantages in efficiency, beam quality, scalability were also explained in the article.

In journal [8], R. Buczynski discussed about the artificial crystal-like microstructure results in a number of unusual properties. In this, different properties possible to obtain in photonic crystal fibers are reviewed. Fabrication and modeling methods are also discussed.

The proposed fiber compensates from E to L band (1.31-1.64 μm) and around this wavelength bands dispersion coefficient have been achieved at range of -150.9 to - 2043.4 ps/(nm.km) with nonlinear coefficient of 89.76 to 52.99 W- 1km-1 by Siddika et.al. At the wavelength of 1.55 μm, negative dispersion, nonlinear coefficient and Confinement loss are investigated as -1016.6 ps/(nm.km), 65.14 $W^{-1}km^{-1}$ and 0.2352 dB/m respectively.[9]

According to simulation, a five-ring dispersion compensating hybrid cladding photonic crystal fiber (DC-HyPCF) is designed that simultaneously offers birefringence of order 3.79×10^{-2}, nonlinear coefficient of 40.1 W^{-1} km^{-1} at 1550 nm wavelength by hasan et al. [10].

Sajjad et.al proposed PCF that shows promising dispersion characteristics (0.0001787 ps/km-nm) with very low effective area (3.03μm^2) and high non-linear parameter (67.23

W^{-1}km^{-1}) at 1.55μm, making it suitable candidate for chromatic dispersion controller and nonlinear optical application. [11]

It is shown from the paper's [12] numerical results by Saitoh et.al that it is possible to design a four ring PCF with flattened dispersion of 0 ± 0.5 ps/(km·nm) from a wavelength of 1.19 μm to 1.69 μm and a five-ring PCF with flattened dispersion of 0 ± 0.4 ps/(km·nm) from a wavelength 1.23 μm to 1.72 μm.

In [13] by Samiul et.al the designed fiber's average dispersion of about -138 ps/(nm-km) with an absolute dispersion variation of 12 ps/(nm. km). Moreover, to check the dispersion accuracy, sensitivity of the fiber dispersion properties to a ± 1–5% variation in the optimum parameters is studied for practical conditions.

In paper [14] by Sumaiya et.al according to simulation results, a five-ringed modified hexagonal photonic crystal fiber (MH-PCF) having germanium (Ge) doped silica core can be designed with a low confinement loss at 1550 nm of the order 1.026×10^{-14} dB/km with simultaneously nearly zero ultra-flattened chromatic dispersion of 0 ± 0.35 ps/nm/km in a wavelength range of 1.30 to 1.65 μm as well as large effective area in a wide range of wavelengths.

The proposed design is suitable for the application of polarization maintaining residual dispersion compensation (RDC) as it offers high negative flattened average dispersion of $-(478\pm8)$ ps.nm^{-1}.km^{-1} within the wavelength of 1.4 to 1.7 μm (300 nm band) by Russel et.al in [15].

The proposed (dd-SPCF) defected core spiral photonic crystal fiber by Mondal et.al in [16] shows promising dispersion characteristics (-0.000169 ps/km-nm) with very low effective area (2.65162 μm^2) and high nonlinear 76.44 W^{-1}km^{-1} parameter at operating wavelength 1.55 μm, making it a suitable candidate for chromatic dispersion controller and nonlinear optical applications.

In [17] by Asiful et.al results show that the fiber exhibits an average dispersion of -227 ps/nm-km with a flattened dispersion profile. It is also demonstrated that the fiber shows a high birefringence of 0.0221 at the wavelength 1550 nm. In the paper an elliptical air hole

is introduced as a defect in the core region and this gives an additional flexibility to tailor the dispersion property.

In paper [18] by Samiul et.al the designed fiber exhibits flattened negative dispersion over the S + C + L + U wavelength bands and an average dispersion of −465.5 ps⁄(nm.km) in the wavelength range 1460-1675 nm with an absolute dispersion variation of 10.5 ps⁄(nm.km). In addition, the proposed PCF shows a high birefringence of 2.68×10^{-2} at the operating wavelength 1550 nm. Moreover, the variation of two air holes in the first ring up to 5% ensures an average dispersion of −491.5 ps⁄(nm.km) with a dispersion variation of 13 ps⁄(nm.km), and birefringence reaches up to 3×10^{-2}.

The proposed structure is obtained by Silva et.al in [19] by introducing a small Ge-doped core at the center of a conventional photonic crystal fiber. Numerical results show that the designed photonic crystal fiber exhibits flattened negative dispersion over *E+S+C+L+U* wavelength bands with an average dispersion of -212 ps.km $^{-1}$nm $^{-1}$.

In [20] by Bakar et.al the proposed design is numerically investigated for residual dispersion compensation in optical transmission link. The optimized structure shows a flattened and high average dispersion of -457.4 ps/(nm.km) in the wavelength range of 1360 nm to 1690 nm. The sensitivity of the fiber dispersion properties to a ±2% variation in the optimum parameters is studied for practical conditions.

In the paper [21] Wang et.al proposed the flat normal dispersion in the wavelength range of 1540–2600 nm, where the values of the dispersion slope are between 0.0058 and 0.03 ps/(nm.km). Furthermore, the numerical results show that the flat-top supercontinuum spectrum ranging from 1000 to 2600 nm can be generated by launching pump pulses at the wavelength of 1550 nm in the heavily Ge doped fiber with a four-layer refractive index profile.

In [22] the presented result by Lucki et.al comprises a numerical model of a photonic crystal fiber in a submicron lattice, specific for its negative dispersion coefficient achieved for broad spectrum of telecommunication wavelengths, i.e. 1300 − 1700 nm. The air holes doped with fluoride materials enhance negative dispersion coefficient to - 438 ps.nm^{-1}. km^{-1}.

Saeed et.al proposed a design in [23] that has relatively low dispersion with negligible variation has become feasible in the wavelength range of 1.1 to 1.8 μm. According to the new structure of PCF presented in this study, the dispersion slope is 6.8×10^{-4} ps/(km.nm) and the confinement loss reaches below 10^{-6} dB/km in this range, while at the same time an effective area of more than 50 μm^2 has been attained.

1.6 Objectives of The Thesis

The objectives of the thesis are set as under:

(1) To study structural properties of PCF to analyze and propose a suitable model.

(2) To compensate the dispersion by varying doping parameters of the core.

(3) To study other characteristics of the designed H-PCF over a broadband range.

1.7 Organization of The Thesis

Chapter 1 deals with the introduction of the thesis. This chapter generalizes optical fiber communication system, history, benefits and types of PCF etc.

Chapter 2 deals with the losses in PCF and light guiding mechanism through PCF.

Chapter 3 describes the designed PCF model by using doping parameters and analysis of the H-PCF.

Chapter 4 covers the description of the plots found from the results of the thesis work and describes the detail analysis of the results/plots. It also gives a summary of comparison of results.

Chapter 5 includes comparison with some previous works, gives some idea of the future works and conclusion of the thesis.

CHAPTER 2

CHARACTERISTICS OF PHOTONIC CRYSTAL FIBER

2.1   Introduction

PCFs have been under intensive study due to their unique and useful optical properties. PCFs are also referred as microstructure optical fibers. PCFs fall into two basic categories. The first one, an index guiding PCF is usually formed by a central solid defect region surrounded by multiple air holes in a regular triangular lattice and confines light by total internal reflection like standard fibers. In this case the average refractive index of the cladding is reduced because of the air holes (low refractive index). The second one uses a perfect periodic structure exhibiting a photonic band-gap (PBG) effect at the operating wavelength to guide light in a low index core region which is also called PBG fiber (PBGF). A comprehensive review of guidance mechanism, optical properties and the factors which affect the performance of optical fibers are also presented in this chapter.

2.2   Loss Properties of PCF

Optical fibers are used to transfer light over distances ranging from meters to thousands of kilometers. Over such spaces, even small imperfections can lead to substantial effects. Conventional silica fibers have attained such an amazing degree of perfection that their losses are about 0.2dB/km at 1.55 μm wavelength are limited by a mixture of intrinsic material absorption and scattering from microscopic density fluctuations. On the other hand, at longer wavelengths such as the 10.6 μm large-power LASERS used for various industrial and medical applications, silica and other common fiber materials are not transparent at all. Interestingly, not all losses are bad. As they have seen, most of the proposed hollow-fiber designs have been multi-mode. They support multiple guided modes that propagate at different speeds. Unchecked this results in modal dispersion. Since it is impossible to avoid exciting multiple modes, the differing velocities cause pulses to spread and information transmission to be scrambled. However, this problem is reduced in a hollow core fiber by differential attenuation. Some modes have much lower losses than others and thus transmission in everything but the lowest-loss mode will be filtered out after propagation over a long distance.

2.2.1 Attenuation

The attenuation A(λ) at wavelength λ of a fiber between two cross-sections separated by distance L is defined, as:

$$A(\lambda) = 10\log\frac{P_1(\lambda)}{P_2(\lambda)} \text{ (dB)} \qquad (2.1)$$

Where,

$P_1(\lambda)$: optical power traversing the cross-section 1, and

$P_2(\lambda)$: optical power traversing the cross-section 2 at the wavelength λ.
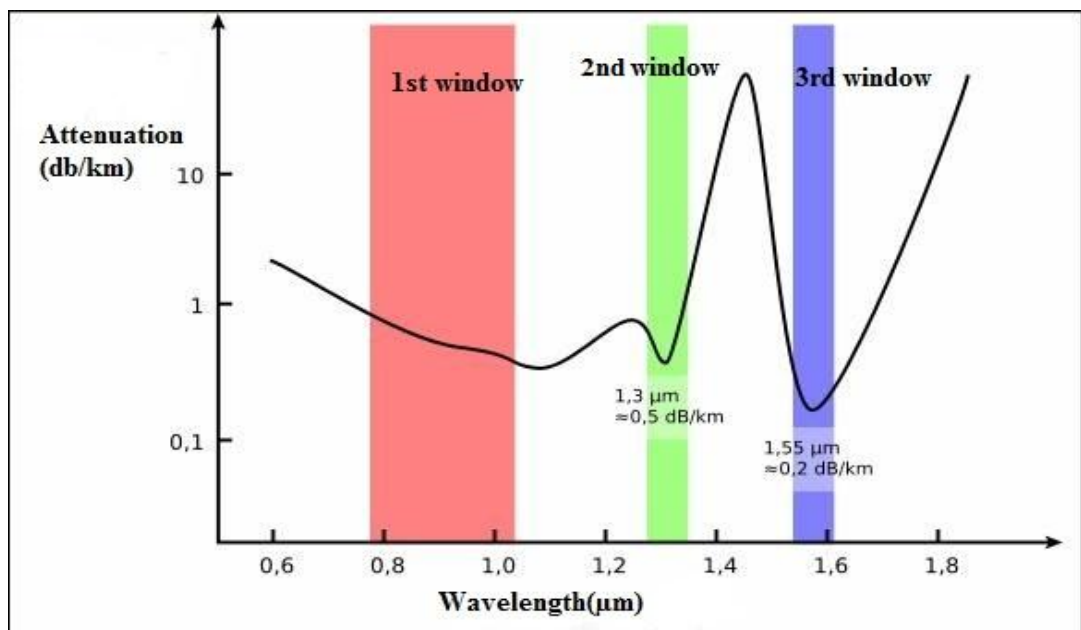
Fig. 2.1: Effect of attenuation in transmission window [3]

For a uniform fiber, it is possible to define attenuation per unit length or an attenuation coefficient which is independent of the length of the fiber:

$$\alpha_{dB} = \frac{A(\lambda)}{L} \text{ dB/km} \qquad (2.2)$$

2.2.2 Confinement Loss

The losses in PCFs occur for a number of reasons, such as intrinsic material absorption loss, structural imperfection loss, Rayleigh scattering loss, confinement loss, and so on. Fabrication related losses can be reduced by carefully optimizing the fabrication process. Confinement loss is an additional form of loss that occurs in single-material fibers. PCFs

23

are usually made from pure silica and so the guided modes are inherently leaky because the core index is the same as the index of the outer cladding without air holes. This confinement loss can be reduced exponentially by increasing the number of rings of air holes that surround the solid core, and is determined by the geometry of the structure.

It is important to know how many numbers of rings of air holes are required to reduce the confinement loss under the Rayleigh scattering limit for practical fabrication process. The confinement loss of the fundamental mode has been computed from the imaginary part of the complex effective index, n_{eff} using [10],

$$L_C = 8.686 k_o I_m [n_{eff}] \qquad (2.3)$$

2.2.3 Birefringence

Optical property depends on polarization and propagation direction of light. Optically anisotropic, where anisotropic is the definite direction that passes definite light, materials are said to be birefringent. Birefringence is a responsible of phenomenon of double reflection whereby a ray of light when incident upon a birefringent material is split by polarization into two rays taking slightly different paths. High birefringence is used in fiber optic sensors. For high birefringence, design core should be asymmetrical and cladding can be elliptical instead of circular.

The difference in refractive indexes along the x-axis and the y-axis, η_x and η_y respectively is called birefringence, B.

This formula implies that $\eta_x > \eta_y$; in other word, y is the fast axis, x the slow axis. Here "x" and "y" for these two axes have been chosen quite arbitrarily. Usually the terms fast and slow are used to denote the appropriate axis.

In conventional single mode fibers without birefringence design, B is small and changes randomly along the fiber because of variations in the core shape and the anisotropic stress acting on the core [10].

$$B = | Re(\eta_{xeff}) - Re(\eta_{yeff}) | \qquad (2.4)$$

2.2.4 Dispersion

Dispersion is the broadening or spreading of optical signal while it propagates inside the fiber. The phenomenon of spreading of optical pulse as it travels along the fiber and limits the information capacity of the fiber is known as dispersion. Dispersion of the transmitted optical signal causes distortion for both digital and analog transmission along optical fibers.
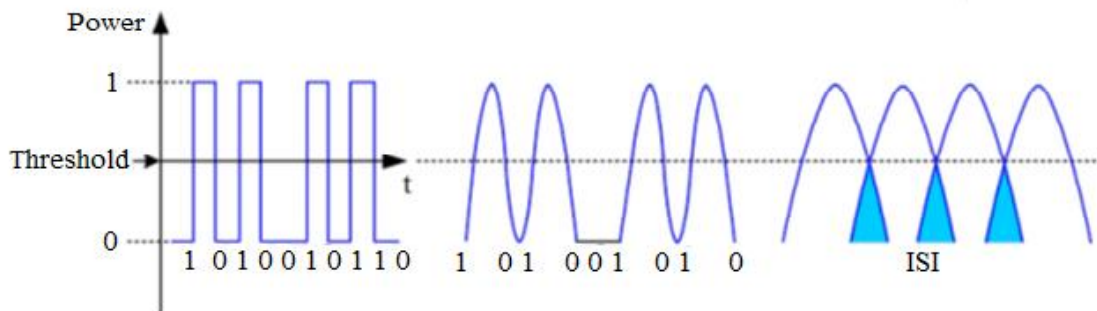
Fig. 2.2: Effect of dispersion in optical pulses [2]

There are mainly two types of dispersion in optical fiber. These types are:
  i) Chromatic dispersion
  ii) Intermodal dispersion

2.2.4.1 Chromatic Dispersion:

Chromatic dispersion is caused by delay differences among the group velocities of the different wavelengths composing the source spectrum. The consequence of the chromatic dispersion is a broadening of the transmitted impulses.
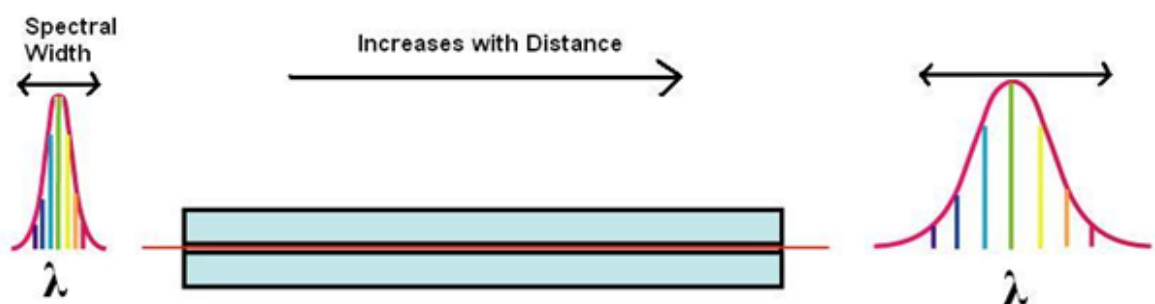
Fig. 2.3: Effect of chromatic dispersion on spectral width [2]

The chromatic dispersion is essentially due to two contributions: material dispersion and waveguide dispersion. The material dispersion occurs because the refractive index of silica (and hence the group velocities) changes with the optical frequency (wavelength) [12].

$$D_{mat}(\lambda) = -\frac{\lambda}{c} \left| \frac{dn_{eff}^2}{d\lambda^2} \right| \qquad (2.5)$$

The waveguide depends on the dispersive properties of the waveguide itself (e.g. the core radius and the index difference). In a single mode fiber, chromatic dispersion is sum of the material and waveguide dispersion.

$$D(\lambda) = D_{mat}(\lambda) + D_{wg}(\lambda) \qquad (2.6)$$

An example of the interplay between these two contributions in the total dispersion is given in Fig. 2.4.
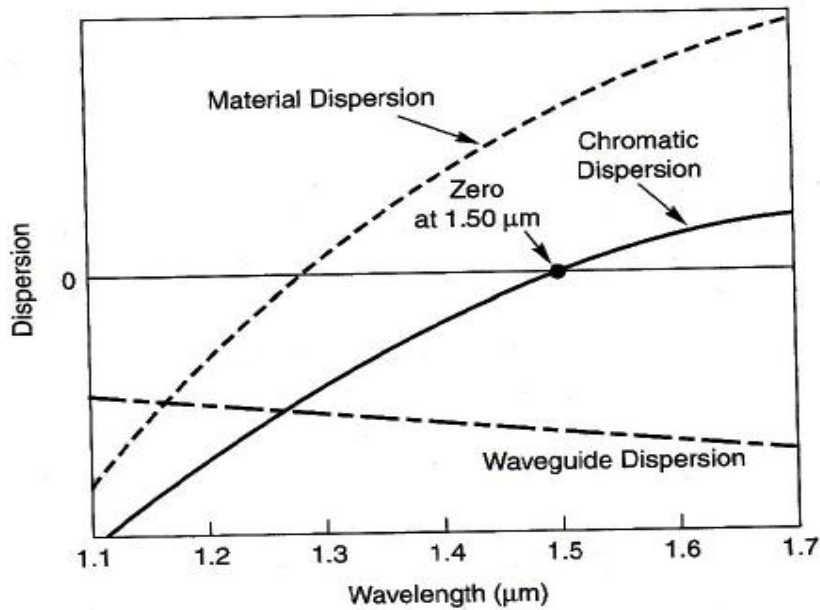
Fig. 2.4: Effect of material and waveguide dispersion on total chromatic dispersion [3]

2.2.4.2   Intermodal Dispersion

Intermodal dispersion results from different propagation characteristic of higher order transverse modes in waveguides, such as multimode fibers. This effect can severely limit the possible data rate of a system for optical fiber communication based on multimode fibers. But single mode fiber does not show intermodal dispersion.

$$\sigma_{inter} = (Ln_1^2\Delta)/(2\sqrt{3}\,cn_2) \tag{2.7}$$

Here, L = Fiber length

n_1 = Core refractive index.

n_2 = Cladding refractive index.

c = Light velocity.

2.2.5 Nonlinear Effects

Usually light waves or photons transmitted through a fiber have little interaction with each other, and are not changed by their passage through the fiber (except for absorption and scattering).

There are exceptions, however, arising from the interactions between light waves and the material transmitting them, which can affect optical signals. These processes are normally referred to as nonlinear effects or phenomena because their strength typically depends on the square (or some higher power) of the optical intensity.

$$\gamma = \frac{2\pi n_2}{\lambda A_{eff}} \tag{2.8}$$

where,

γ = Nonlinear parameter

n_2 = Nonlinear refractive index

λ = Wavelength

A_{eff} = Effective area.

Here, nonlinear refractive index is calculated from, $n_2 = 2.507 + 0.505\Delta$ $\qquad$ (2.9)

and $\Delta = (n_1{}^2 - n_2{}^2)/(2n_1{}^2)$. Where Δ is the relative refractive index difference, n_2 is the refractive index of pure silica n_1 is the value after doping GeO_2 with SiO_2.

Hence nonlinear effects are weak at low powers but they can become much stronger at high optical intensities. This situation can result either when the power is increased or when it is concentrated in a small area such as the core of a single-mode optical fiber.

There are two broad categories of nonlinear effects that can be separated based on their characteristics: namely, scattering and Kerr effects.

Kerr effects

Self-phase modulation	Cross-phase modulation	Four-wave mixing

Scattering effects

Stimulated Raman Scattering	Stimulated Brillouin Scattering
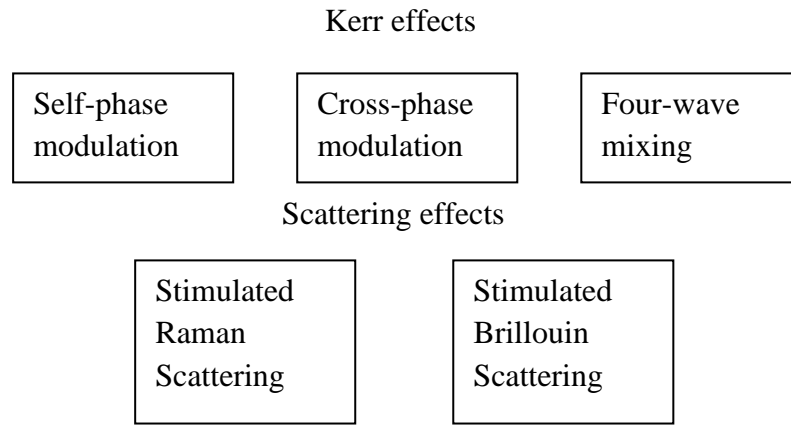
Fig. 2.5: Block schematic showing the fiber nonlinear effects [2]

2.3   Electromagnetic Wave Guiding Mechanism

Since a PCF is a structure that usually is formed by a center core surrounding by a periodic structure (cladding), basically we can think in two possible guiding mechanism: index-guiding or bandgap-guiding.

In index-guiding PCFs, similar to conventional fibers, light is guided in a higher index core by modified total internal reflection from a low effective index cladding. In bandgap PCFs, light is confined in a low-index core by reflection from a photonic crystal cladding. Because of their novel guiding mechanism and variety in design, PCFs have a number of novel properties and significant applications. For index-guiding PCFs, the properties include endlessly single mode, large mode area, high numerical aperture, high birefringence, high nonlinear coefficient and dispersion management. Various bandgap PCFs and many significant applications for them have been achieved, such as low-loss air-core bandgap PCFs, all-solid bandgap PCFs, a variety of PCF devices and Bragg PCFs for CO_2 laser transmission. Most PCFs guide light by only one of the two different guiding mechanisms, although hybrid-guiding (combination of index-guiding and bandgap-guiding) has been utilized in photonic crystal slabs for many years.

Recently a hybrid PCF has been discovered which guides light by both index-guiding and bandgap-guiding simultaneously. This hybrid PCF was composed of air holes and Ge-doped silica rods disposed around an undoped silica core; the air holes were arranged in a hexagonal pattern as in an index-guiding PCF, while the high index rods replaced a single row of air holes along one of the PCF axes. However, the hybrid PCF is a quite new issue; a kind of hybrid PCF and some basic analysis has been proposed. And to be precise, it was

not a systematic investigation that offers insight into the nature of the hybrid PCF and many significant properties of hybrid PCFs have not been investigated yet.

2.3.1 Normalized Frequency of PCF

The V parameter (normalized frequency) is frequently used in the design of conventional SIFs and is given by

$$V = \frac{2\pi a}{\lambda}\sqrt{n_{co}^2 - n_{cl}^2} \tag{2.10}$$

that must be less than 2.405 for the fiber to be single mode, where λ is the operating wavelength, a is the core radius, n_{co} is the core index, and n_{cl} is the cladding index. Recently, it has been reported that the fundamental properties of index-guiding PCFs such as cutoff wavelength, mode field diameter (MFD), splice loss, and so on, can be easily estimated without the need for heavy numerical computations by appropriately defining the V parameter. By analogy with step index fibers, the effective V parameter V_{eff} for PCFs can be defined as,

$$V_{eff} = \frac{2\pi}{\lambda} A_{eff}\sqrt{n_{co}^2 - n_{FSM}^2} \tag{2.11}$$

Where, A_{eff} is the effective mode area.

2.3.2 Effective Mode Area

The effective mode area A_{eff}, is related to the effective area of the fiber core area which is computed using transverse electric or magnetic field vector of the whole cross-sectional area of the fiber. The effective area of the of the fiber core A_{eff} is defined as

$$A_{eff} = \frac{\left(\iint |E_t|^2 \, dx\, dy\right)^2}{\iint |E_t|^4 \, dx\, dy} \tag{2.12}$$

Or,

$$A_{eff} = \frac{\left(\iint |H_t|^2 \, dx\, dy\right)^2}{\iint |H_t|^4 \, dx\, dy} \tag{2.13}$$

Where, E_t and H_t is the transverse electric field vector and magnetic field vector respectively and the integration is done through the whole cross-sectional area of the fiber.

2.3.3 Effective Refractive Index

In homogenous transparent media, the refractive index n can be used to quantify the increase in the wave number (phase change per unit length) caused by the medium: the wave number is n times higher than it would be in vacuum. The effective refractive index n_{eff} has the analogous meaning for light propagation in a waveguide.

$$\beta = n_{eff} \frac{2\pi}{\lambda}$$

(2.14)

The effective refractive index depends not only on the wavelength but also (for multimode waveguide) on the mode in which the light propagates. For this reason, it is also called effective mode index.

Again, effective refractive index is a number that quantify the phase delay per unit length in a waveguide, relative to the phase delay in vacuum. The rate of change in the fundamental LP_{01} mode propagating along a straight fiber is determined by the phase propagation constant β.

It is directly related to the wavelength of LP_{01} mode λ_{01} by the factor of 2π. Hence:

$$\beta \lambda_{01} = 2\pi$$

(2.15)

An effective refractive index for single mode fiber sometimes referred to as a phase index or normalized phase change coefficient, n_{eff}. It is defined by the ration of the propagation constant of the fundamental mode to that of the vacuum wave number, k.

$$n_{eff} = \frac{\beta}{k}$$

(2.16)

Hence the wavelength of the fundamental mode λ_{01} is smaller than the vacuum wavelength λ by the factor $1/n_{eff}$.

$$\lambda_{01} = \frac{\lambda}{n_{eff}}$$

(2.17)

2.4 Theory of Electromagnetic (EM) Light Propagation Through PCF

The basic starting point in understanding the optical properties of photonic crystals is that Maxwell's equations. An electromagnetic wave can be expressed in terms of an electric field vector $\vec{E}$ and a magnetic field vector $\vec{B}$. When incident on a material the terms $\vec{H}$, the

magnetic flux density, $\overrightarrow{D}$ the electric displacement vector, $\vec{J}$ the current density and ρ the charge density are also defined. The Maxwell's equations in the differential form may be expressed in the international system units as:

$$\nabla * \overrightarrow{E}(\vec{r},t) = -\frac{\delta}{\delta t}\overrightarrow{B}(\vec{r},t) \tag{2.18a}$$

$$\nabla * \overrightarrow{H}(\vec{r},t) = \frac{\delta}{\delta t}\overrightarrow{D}(\vec{r},t) + J \overrightarrow{_{free}} \tag{2.18b}$$

$$\nabla * \overrightarrow{B}(\vec{r},t) = 0 \tag{2.18c}$$

$$\nabla * \overrightarrow{D}(\vec{r},t) = \rho_{free} \tag{2.18d}$$

Considering a number of assumptions valid for our particular case the previous equations can be simplified. First, for a medium that is free of free charges and free currents, ρ_{free} and J_{free} are set to zero. Next, if the field strengths are assumed to be small enough, the relations $\overrightarrow{D}$ to $\overrightarrow{E}$ and $\overrightarrow{B}$ to $\overrightarrow{H}$ can be considered as linear. Finally, for isotropic loss-less materials the dielectric permittivity, $\varepsilon(\vec{r},\omega)$ is scalar and real where $\vec{r}$ is the spatial vector and ω is the angular frequency of light. Then, the constitutive equations of the material are given by:

$$\overrightarrow{D}(\vec{r},t) = \varepsilon(\vec{r})\overrightarrow{E}(\vec{r},t) \tag{2.19a}$$

$$\overrightarrow{B}(\vec{r},t) = \mu_0\overrightarrow{H}(\vec{r},t) \tag{2.19b}$$

Where μ_0 is the magnetic permeability of vacuum. If harmonic time dependence of the electromagnetic fields is assumed, the fields can be written as:

$$\overrightarrow{E}(\vec{r},t) = \overrightarrow{E}(\vec{r})e^{i\omega t} \tag{2.20a}$$

$$\overrightarrow{H}(\vec{r},t) = \overrightarrow{H}(\vec{r})e^{i\omega t} \tag{2.20b}$$

By the substitution of equations (2.17) into equations (2.18) the following system is obtained:

$$\nabla * \overrightarrow{E}(\vec{r}) = -i\,\omega\varepsilon\mu_0\overrightarrow{H}(\vec{r}) \tag{2.21a}$$

$$\nabla * \overrightarrow{H}(\vec{r}) = i\omega\varepsilon\,\vec{r}\,\overrightarrow{E}(\vec{r}) \tag{2.21b}$$

$$\nabla . \overrightarrow{H}(\vec{r}) = 0 \tag{2.21c}$$

$$\nabla . (\varepsilon(\vec{r}) \, \vec{E}(\vec{r}) = 0 \tag{2.21d}$$

Equation (2.19a) and equation (2.19b) can be rearranged into a single vectoral expression satisfied by the magnetic field $\vec{H}(\vec{r})$

$$\nabla * 1/\varepsilon(\vec{r}) \, (\nabla * \vec{H}(\vec{r})) = \omega^2 \mu_0 \, \vec{H}(\vec{r}) \tag{2.22}$$

This general expression represents an eigen value problem that together with the divergence equation given the response of an optical field in a dielectric medium whose dielectric constant distribution is given by $\varepsilon(\vec{r})$. If the spatial dependence of the dielectric constant of any medium is known, the solution to equation (2.22) will provide the solutions to the optical modes. However, the complex geometry of photonic crystals makes the solution of this equation non-trivial and outside of the simplest cases, requires a fair amount of computational work to provide answers. The left side of the equation (2.19) can be formulated as an operator (Θ) acting on $\vec{H}(\vec{r})$ So that it takes explicitly the form of an eigenvalue problem

$$\Theta\vec{H}(\vec{r}) = \omega^2 \mu_0 \, \vec{H}(\vec{r}) \tag{2.22a}$$

$$\Theta \equiv \nabla * \left(\frac{1}{\varepsilon(\vec{r})} \nabla * \right) \tag{2.22b}$$

Similarly, from equation (2.21), a master equation for $\vec{E}$ could also be formulated. However, it is more convenient to express the problem in terms of $\vec{H}(\vec{r})$. This is because the operator Θ is Hermitian which simplifies the computational problem. After obtaining the modes $\vec{H}(\vec{r})$ for a given frequency, the following relation can be used to obtain the electric field distribution,

$$\vec{E}(\vec{r}) = (-i/ \, \omega\varepsilon(\vec{r}) \,) \nabla * \vec{H}(\vec{r}) \tag{2.23}$$

In optical fibers, the translational invariance of the refractive index profile along the z-directional leads to the following form of solutions for equation (2.20)

$$\vec{H}(x, y, z) = \vec{H}(x, y)e^{-i\beta z} \tag{2.23}$$

Where β is the propagation constant along z (the fiber axis). The harmonic mode $\vec{H}$ (x,y) is the eigen vector associated to the eigen value β .In the case of a wave propagation in a homogeneous medium ($\varepsilon(\vec{r}) = \varepsilon$) equation (2.20) reduces to the Helmholtz equation,

which can be solved in a closed form. In the same manner, if the geometry of the system is simple enough to apply analytical boundary conditions at the interfaces, the electromagnetic problem can also have an analytical solution. This is the case of conventional step-index fibers. However, in the case of photonic crystal fibers the eigen value problem is more complicated due to the fiber's complex geometry and analytical solutions are impossible to obtain. Powerful numerical methods are used to obtain the eigenvectors and Eigen values of the electromagnetic problem. Nevertheless, when analyzing infinite structures, the periodic nature of a photonic crystal allows the simplification of the electromagnetic problem to a small region of the photonic crystal. Photonic crystals can be described in terms of a periodic array of points in space called a lattice and a unit cell which is represented identically at every point of the lattice. The unit cell is defined as the smallest area, which by mere translation can fully represent the structure. Every point of the lattice can be defined in terms of the lattice vectors $(\overrightarrow{\mu_1}\overrightarrow{\mu_2}\overrightarrow{\mu_3})$, which are the smallest vectors that can connect one lattice point with another. All crystals have an associated lattice in Fourier space called reciprocal lattice which consists of the set of all the allowed terms in the Fourier expansion of the periodic structure. The lattice is defined in terms of the primitive reciprocal lattice vectors $(\overrightarrow{g_1}\overrightarrow{g_2}\overrightarrow{g_3})$.

To examine the way a photonic crystal affects the propagation of light passing through it, the dielectric constant of the structure must be expressed in terms of the lattice vector $\vec{R}$. The periodic dielectric function of a photonic crystal satisfies

$$\varepsilon(\vec{r}) = \varepsilon(\vec{r} + \vec{R}) \tag{2.24}$$

According to Bloch's theorem the solution of the magnetic field can be expressed as Bloch's states consisting of a plane wave modulated by a periodic function with the same periodicity a photonic crystal.

$$\overrightarrow{H_k}(r) = \overrightarrow{U_k}(r)e^{-i\vec{k}\vec{r}} \tag{2.25}$$

Where $\vec{k}$ is the wave vector, $\vec{r}$ denotes the position vector and $\overrightarrow{U_k}(\vec{r})$ has the same periodicity as the lattice, i.e. $\overrightarrow{U_k}(\vec{r}) = \overrightarrow{U_k}(\vec{r} + \vec{R})$. Therefore, knowing the values of the magnetic field $\overrightarrow{H_k}$ in a unit cell, the magnetic field in all the structure can be inferred from equation (2.22). In other words, the electromagnetic problem in an infinite photonic crystal is reduced to finding the values of the magnetic field in a small area. In the same way, in the reciprocal lattice, a Blotch state for a wave vector $\vec{k}$ is equal to the Bloch state $\vec{k} + \vec{G}$

where $\vec{G}$ is any vector of the reciprocal lattice. This gives rise to a periodicity of the dispersion curve in the reciprocal space (or $\vec{k}$ space), expressed as $\omega(\vec{k}) = \omega(\vec{k} + \vec{G})$. Consequently, the dispersion information of the modes is contained in a region of the reciprocal space called the Brillouin zone and only wave vectors $\vec{k}$ lying inside the Brillouin zone identify an independent mode. Therefore, the dispersion curves of photonic crystals are normally presented as plots of frequency versus wave vectors in the Brillouin zone.

2.5   Conclusion

In this chapter the loss properties of PCF are described in details. The light guiding mechanism is explained with appropriate equations. Mostly the Maxwell's equations help to understand light pulse behavior inside the fiber core.

CHAPTER 3

ANALYSIS OF THE PCF SYSTEM MODEL

3.1   Introduction

In recent days many research works have been done over PCF. By optimizing various parameters such as pitch (Λ), air holes diameter (d), varying core and cladding materials, varying structure (hexagonal, decagonal etc.) many PCF's model have been proposed. Those models show flattened, zero or negative dispersion, large or small effective area, low confinement loss, high or low nonlinearity contributing in various fields. The proposed hexagonal model is designed using COMSOL Multiphysics 4.3. Optimized model has been found by varying air holes diameter of the core and cladding. The model has been finalized based on the electric field distribution which exactly passes through the core. PML (Perfectly Matched Layer) has been added to bind the electric field in the region. In model wizard, Radio Frequency (RF) has been chosen. The proposed two-dimensional model has been studied in Electromagnetic Wave (EMW) frequency domain physics interface. This field is found in Radio Frequency. For analyzing the mode field of the proposed model Mode Analysis has been added as the study type. The mode field of the model has been taken in various wavelengths which is used in studying various parameters such as effective mode index, dispersion, chromatic dispersion, effective area, nonlinearity parameter etc. These parameters have been investigated and discussed thoroughly.

3.2   System Model
3.2.1   System Diagram

Silicon dioxide (SiO$_2$) outer cladding
Silicon dioxide (SiO$_2$) inner cladding
Pitch(Λ=1.55 μm)
Air holes
Elliptical silica core(a=2*r1,b=r1)
1st layer radius,r1=(d1/2)=(0.5*Λ)/2
2nd layer radius,r2=(d1/2)=(0.5*Λ)/2
3rd layer radius,r3=(d2/2)=(1.0*Λ)/2
4th layer radius,r4=(d2/2)=(1.0*Λ)/2
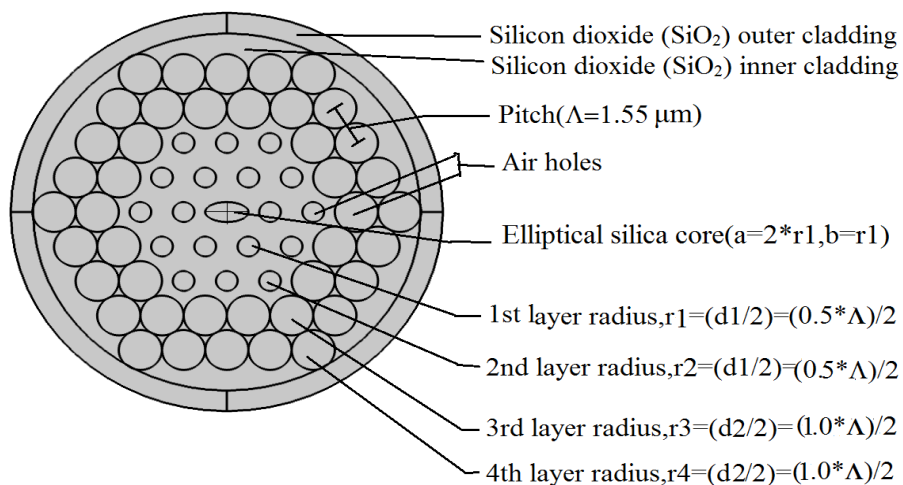
Fig. 3.1: System model of the proposed Hexagonal shaped PCF.
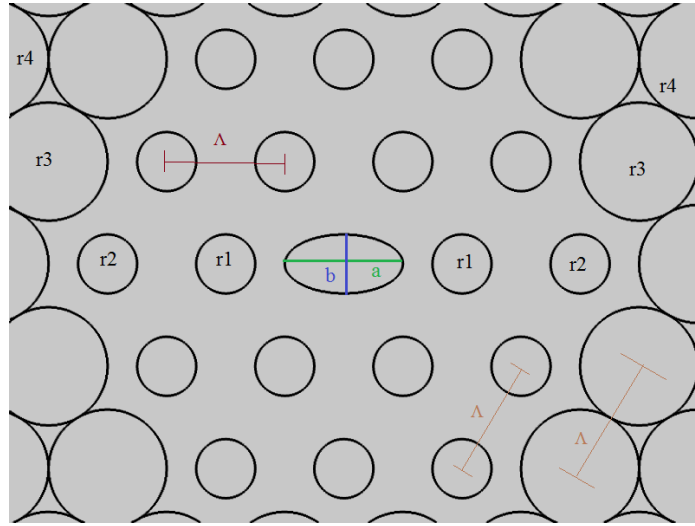
Fig. 3.2: Enlarged view of H-PCF with optimized structural parameters

3.2.2 Description of The System Model

The proposed Hexagonal PCF (H-PCF) has four rings and two types of air holes. The diameters for 1st and 2nd air holes rings (near the core) are same. The first and second layer rings diameter is denoted as d1 and respectively radius is denoted as r1 and r2. The diameters for 3rd and 4th air holes rings are same. d2 is the diameter of the 3rd and 4th layer air holes. Again, the radius for the 3rd and 4th layer air holes respectively denoted as r3 and r4. An elliptical shape air hole is considered as the core of the proposed model. Elliptical core has semi major axis, semi minor axis which is respectively shown as a and b. The air holes are arranged in regular hexagonal shape.

Distance between adjacent air holes on an axis is called pitch and is assigned as Λ. Pitch is adjusted so that light pass through the core properly and the design shows low chromatic dispersion. Λ=1.55 μm is the pitch of our design which is found after adjusting all the diameters of the air holes of core and cladding. Considering Λ, the diameter for the 1st and 2nd layer air holes is d1=0.5×Λ, and the radius is r=0.3875 μm, where r1=r2=r. Again, the diameter for the 3rd and 4th layer air holes is d2=1×Λ and the radius is r3=r4=0.5×Λ. In Design, different shape air hole is experimented as the core. As the elliptical shape core gives better result it is finalized. The Elliptical core's semi major axis and semi minor axis are respectively a=2×r, b=r where r=0.3875 μm, is the radius of the 1st and 2nd layer air holes of the model.

Silicon di-oxide or Silica (SiO_2) is the material chosen for the cladding of the H-PCF. The air holes which are arranged in hexagonal shape are made of air. A circular shaped PML is

added at the outer region of the region which confines the electromagnetic wave in the desired region so that no light can escape from the fiber. PML material is same as the cladding material which is SiO_2. PML layer is varied and finally adjusted so that light is confined within the core.

SiO_2 is used as the core material when it is not doped. The Elliptical core is doped with two types of material. In the first approach the core is doped with Germanium Oxide (GeO_2) and its different parameters is observed to obtain low dispersion, a better effective area. Secondly the H-PCF's elliptical core is doped with Barium Fluoride (BaF_2). The obtained results of the two approaches are compared and the best one is suggested.

The model is modified and designed in COMSOL using the previously discussed parameters. The parameter r, r1, r2, r3 is used as the global parameter in COMSOL. Varying wavelength in a wide range, the stability of the light confinement of the model is studied. For the proposed design the wavelength is varied from 1.41 μm to 1.61 μm.

The refractive index for the core and cladding material is calculated using Sellmeier equation and Sellmeier constant. Sellmeier constant $Bs1$, $Bs2$, $Bs3$, $Cs1$, $Cs2$, $Cs3$ are used to calculate the refractive index of SiO_2 which is the cladding material and core material when the core is undoped. The refractive index of GeO_2 is calculated using $Bg1$, $Bg2$, $Bg3$, $Cg1$, $Cg2$, $Cg3$. Sellmeier constants $Ba1$, $Ba2$, $Ba3$, $Ca1$, $Ca2$, $Ca3$ are used for the calculation of refractive index of BaF_2. The modified refractive index of GeO_2 doped SiO_2 core is calculated using Sellmeier equation. Also, Sellmeier equation is used to have the modified refractive index of BaF_2 doped SiO_2 core.

Different parameters which are used to design the proposed H-PCF model are shown below in tabular from:

Name	Description	Expression	Unit	Value
L	Wavelength	1.51	μm	1.5100E-6 m
F	Frequency	c_const/l	Hz	1.9986E14 Hz
P	Pitch	1.55	μm	1.5500E-6 m
r1	Radius of 1st cell	(0.5*Λ)/2	μm	3.8750E-7 m
r2	Radius of 2nd cell	(0.5*Λ)/2	μm	3.8750E-7 m
r3	Radius of 3rd cell	(1*Λ)/2	μm	7.7500E-7 m
r4	Radius of 4th cell	(1*Λ)/2	μm	7.7500E-7 m

X	Doping percentage	0.00		0.0000
Bs1	Sellmeier constant for SiO_2	0.69616630		0.69617
Bs2	Sellmeier constant for SiO_2	0.40794260		0.40794
Bs3	Sellmeier constant for SiO_2	0.89747940		0.89748
Cs1	Sellmeier constant for SiO_2	0.06840430	μm	6.8404E-8m
Cs2	Sellmeier constant for SiO_2	0.11624140	μm	1.1624E-7m
Cs3	Sellmeier constant for SiO_2	9.896161	μm	9.8961E-6m
Bg1	Sellmeier constant for GeO_2	0.80686642		0.80687
Bg2	Sellmeier constant for GeO_2	0.71815848		0.71816
Bg3	Sellmeier constant for GeO_2	0.85416831		0.85417
Cg1	Sellmeier constant for GeO_2	0.068972606	μm	6.8973E-8m
Cg2	Sellmeier constant for GeO_2	0.15396605	μm	1.5397E-7m
Cg3	Sellmeier constant for GeO_2	11.841931	μm	11.842E-6m
Ba1	Sellmeier constant for BaF_2	0.64335620		0.64336
Ba2	Sellmeier constant for BaF_2	0.5067620		0.50676
Ba3	Sellmeier constant for BaF_2	3.82610		3.8261
Ca1	Sellmeier constant for BaF_2	0.0577890		5.7789E-8m
Ca2	Sellmeier constant for BaF_2	0.109680		1.0968E-7m
Ca3	Sellmeier constant for BaF_2	46.3864		4.6386E-5m

Table 3.1: Various parameters of the system model.

3.2.3   Electric Field Distribution Without Doping

Electric field distribution is calculated using derived Eigen value problem found from Maxwell's Equation. Electric field distribution of PCF changes with the variation of core and cladding, air hole diameters, doping and other related parameters. Different structure of PCF shows different Electric mode field distribution. Depending on the core shape and structure (e.g. Hexagonal, decagonal, octagonal etc.) various types of mode field are found which are proposed in many research papers.

COMSOL Multiphysics gives a numerical technique to analyze the electric filed distribution of PCF which is almost similar to practical situation. It applies Finite Element Method (FEM) to analyze and simulate PCF's model to get electric field distribution. FEM represents any geometry through small elements. COMSOL provides responsive

meshing environment. It separates whole PCF model into numerous small elements to analyze the model precisely. Various size, type and shape meshing element are used. Also, user defined meshing can be used to simulate the designed model. COMSOL also provides different types of solver. In our model Eigen value solver 1 is used.

We know that PCF has highest magnetic field density so that light exactly passes through core region. The proposed model is designed and the parameters are varied in such a way that varying wavelength in a broadened range, we get desired electric mode field in all wavelengths.

For undoped H-PCF model electric field is noted from 1.41 to 1.61 μm wavelength. Several observations are taken keeping the designed parameters constant. Data for pitch, Λ=1.55 μm, radius for 1st and 2nd layer air holes is r1=r2=0.3875 μm and diameter d1=0.5×Λ, radius for 3rd and 4th layer air holes r3=r4=0.5×Λ and diameter d2=1×Λ, Elliptical core's semi major axis and semi minor axis are respectively a=2×r, b=r is taken. Best possible result of electric mode field is noted for given wavelengths when it is not doped. The following picture shows 2-dimensional and 3-dimensional view of electric mode field of undoped (0% doping) H-PCF model at 1.42 μm wavelength.
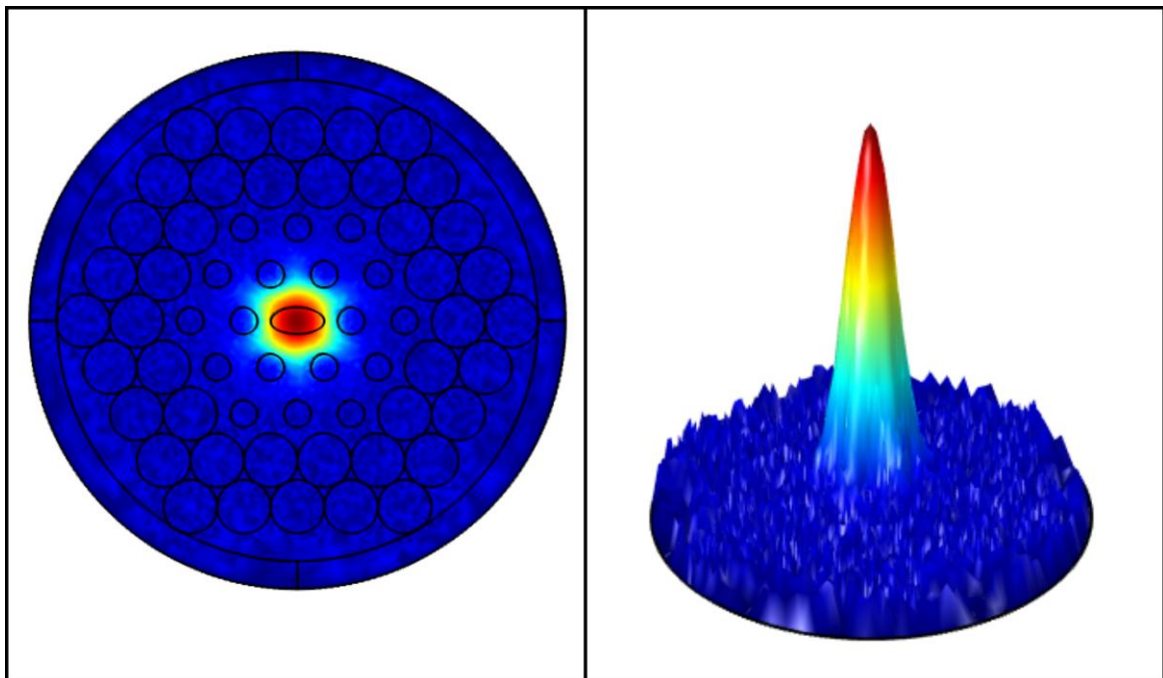
Fig. 3.3: (a) Electric field distribution without doping (b) 3D Electric field distribution without doping for pitch, Λ = 1.55μm.

3.2.4   Electric Field Distribution with Doping

3.2.4.1   Electric Field Distribution of GeO_2 Doped SiO_2

The proposed H-PCF model's elliptical core is doped with GeO_2. The observations for various doping concentrations are considered from wavelength 1.41 μm to 1.61 μm. Varying the doping concentrations electric mode field is observed and the desired mode is studied. The proposed design is simulated with 10%, 30%, 40%, 50%, 60% doping concentrations. Their effect on the propagation of light through H-PCF is studied to minimize the losses. Sellmeier equation and coefficient is also used to calculate the modified refractive index.

All the designed parameter such as pitch, diameter of air holes of 1st, 2nd, 3rd, 4th are kept unchanged. Only doping concentration of the core is varied.

Data for X=10% doping concentration, pitch Λ=1.55 μm, radius for 1st and 2nd layer air holes are r1=r2=0.3875 μm and diameter is d1=0.5×Λ, radius for 3rd and 4th layer air holes are r3=r4=0.5×Λ and diameter d2=1×Λ, Elliptical core's semi major axis and semi minor axis are respectively a=2×r, b=r parameters are same as before doping. For 10% doping concentration at 1.55 μm wavelength 2-Dimensional and 3-Dimension electric mode field is given below.

Fig. 3.4: (a) Electric field distribution of GeO_2 doped SiO_2 (b) 3D Electric field distribution of GeO_2 doped SiO_2 for pitch, Λ = 1.55 μm at 10% doping concentration.

Fig. 3.5: (a) Electric field distribution of GeO_2 doped SiO_2 (b) 3D Electric field distribution of GeO_2 doped SiO_2 for pitch, Λ =1.55µm at 30% doping concentration.

Again, data for X=30% doping concentration, pitch Λ=1.55 µm, radius for 1st and 2nd layer air holes are r1=r2=0.3875 µm and diameter d1=0.5×Λ, radius for 3rd and 4th layer air holes r3=r4=0.5×Λ and diameter d2=1×Λ, Elliptical core's semi major axis and semi minor axis are respectively a=2×r, b=r parameters are same as before doping. For 30% doping concentration at 1.55 µm wavelength 2-Dimensional and 3-Dimension electric mode field is shown below.
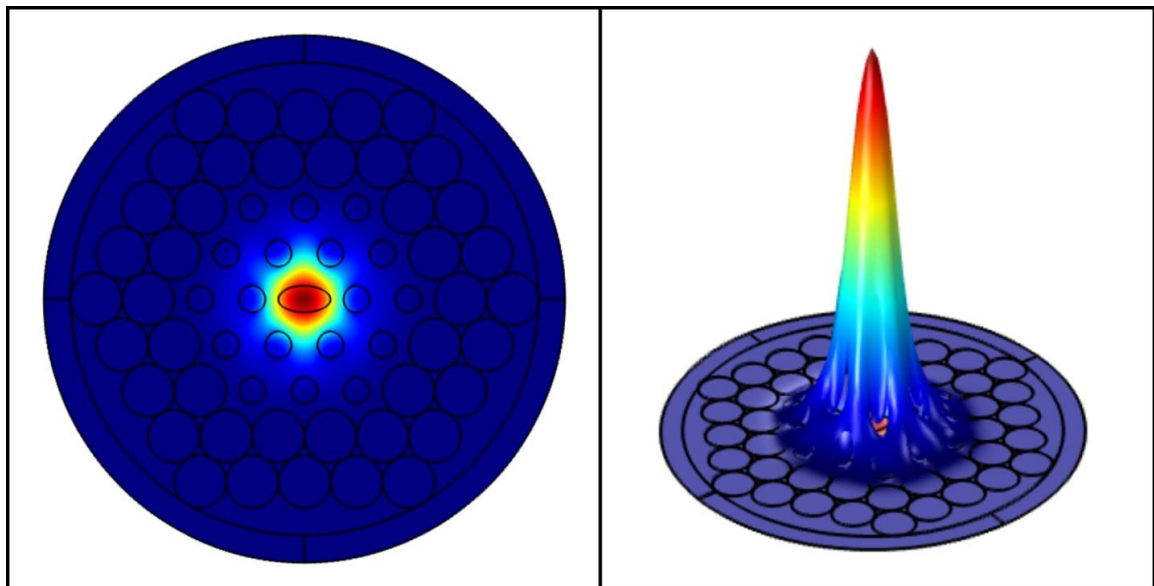

Fig. 3.6: (a) Electric field distribution of GeO_2 doped SiO_2 (b) 3D Electric field distribution of GeO_2 doped SiO_2 for pitch, Λ =1.55 µm at 40% doping concentration.

41

Similarly, data for X=40% doping concentration, pitch Λ=1.55 µm, radius for 1st and 2nd layer air holes are r1=r2=0.3875 µm and diameter d1=0.5×Λ, radius for 3rd and 4th layer air holes r3=r4=0.5×Λ and diameter d2=1×Λ, Elliptical core's semi major axis and semi minor axis are respectively a=2×r, b=r parameters are same as before doping. For 40% doping concentration at 1.55 µm wavelength the proposed model is simulated.

Fig. 3.7: (a) Electric field distribution of GeO_2 doped SiO_2 (b) 3D Electric field distribution of GeO_2 doped SiO_2 for pitch, Λ =1.55 µm at 50% doping concentration.

Furthermore, data for X=50% doping concentration, pitch Λ=1.55 µm, radius for 1st and 2nd layer air holes are r1=r2=0.3875 µm and diameter d1=0.5×Λ, radius for 3rd and 4th layer air holes r3=r4=0.5×Λ and diameter d2=1×Λ, Elliptical core's semi major axis and semi minor axis are respectively a=2×r, b=r parameters are same as before doping. For 50% doping concentration at 1.55 µm wavelength the proposed model is simulated. The observed 2-Dimensional and 3-Dimension electric mode field is presented below.

Also, data for X=60% doping concentration, pitch Λ=1.55 µm, radius for 1st and 2nd layer air holes are r1=r2=0.3875 µm and diameter d1=0.5×Λ, radius for 3rd and 4th layer air holes r3=r4=0.5×Λ and diameter d2=1×Λ, Elliptical core's semi major axis and semi minor axis are respectively a=2×r, b=r parameters are same as before doping. For 60% doping concentration at 1.55 µm wavelength the proposed model is simulated. The observed 2-Dimensional and 3-Dimension electric mode field is given below.
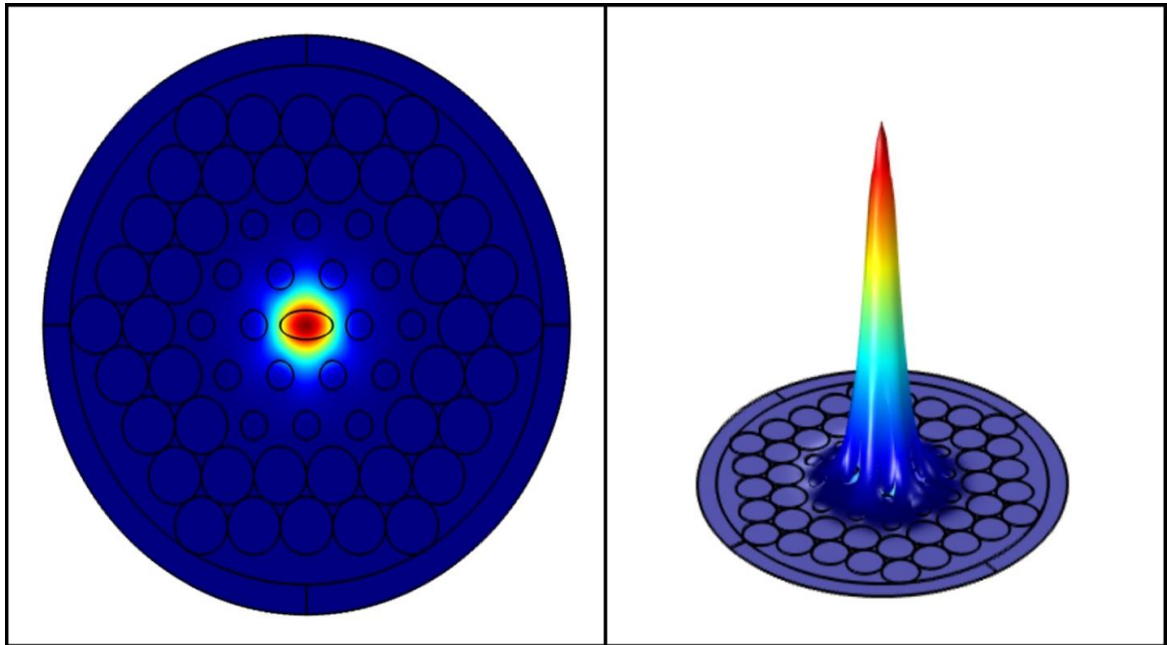
Fig. 3.8: (a) Electric field distribution of GeO_2 doped SiO_2 (b) 3D Electric field distribution of GeO_2 doped SiO_2 for pitch, Λ =1.55µm at 60% doping concentration.
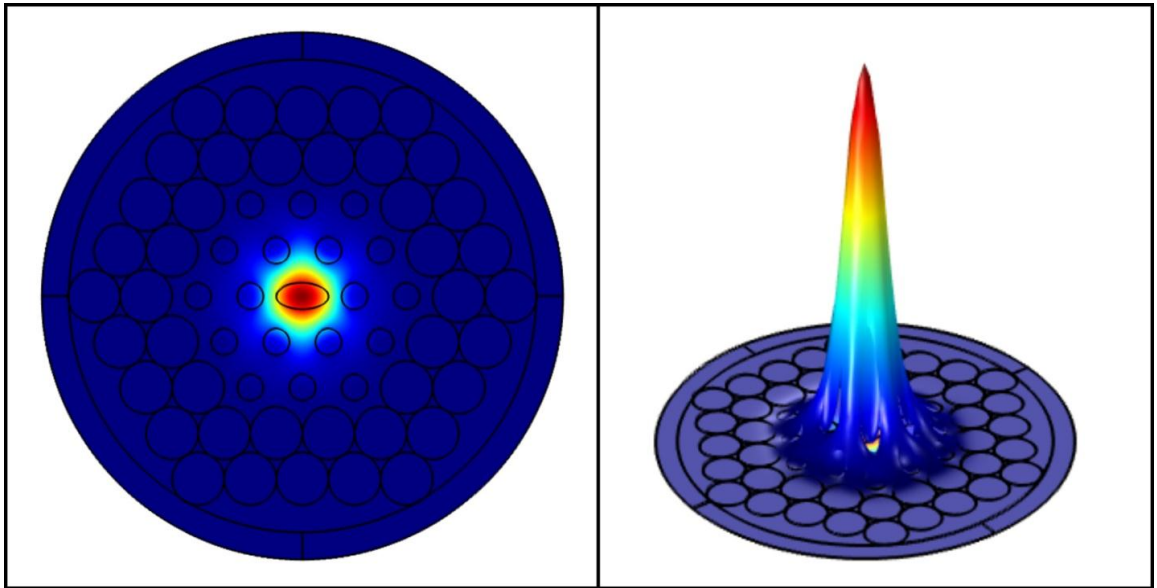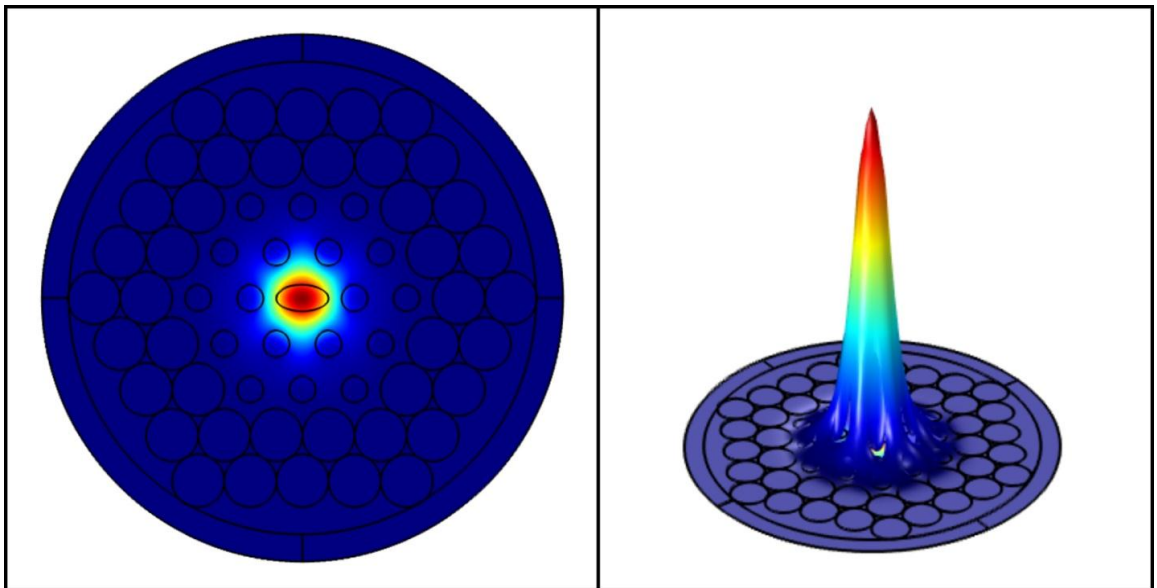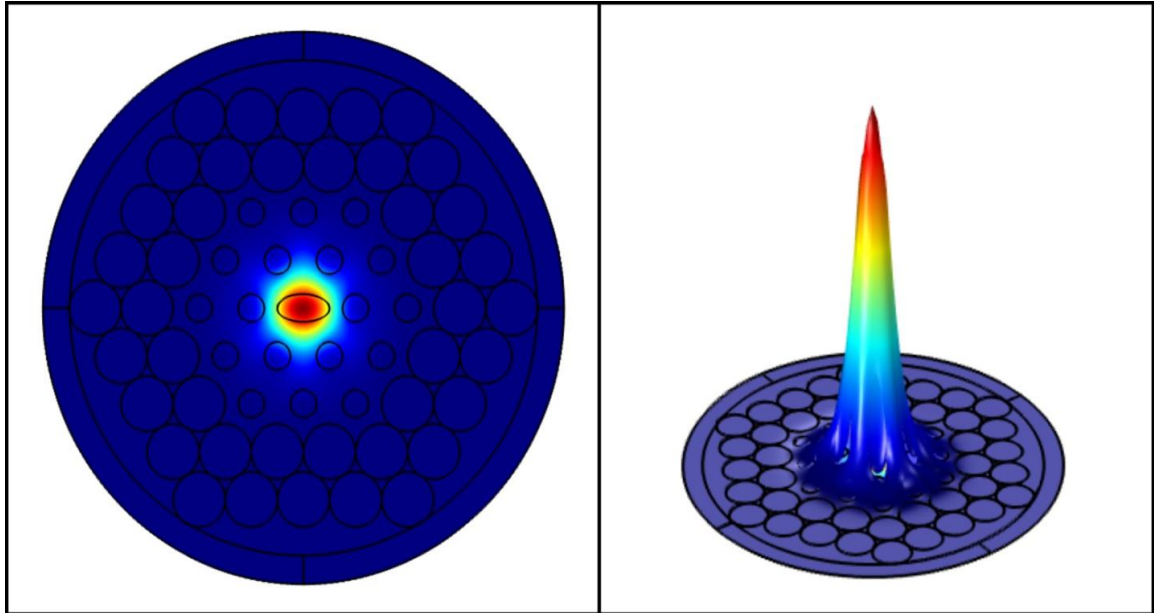
3.2.4.2   Electric Field Distribution of BaF_2 Doped SiO_2

Again, for further investigation propose H-PCF is doped with BaF_2 (Barium fluoride). Doping concentration of core is varied respectively to 10%, 30%, 40%, 50%, 60%. Obtained result of BaF_2-SiO_2 is examined thoroughly to notice the effect of BaF_2 doping on HPCF's core. The cladding material is same as before doping which is SiO_2.

The modified refractive index again is found using Sellmeier equation. The result of doping of GeO_2-SiO_2 is compared with doping of BaF_2 -SiO_2. The electric field distribution for different doping concentration is noticed and compared for analysis.

Data for X=10% doping concentration, pitch Λ=1.55 µm, radius for 1st and 2nd layer air holes are r1=r2=0.3875 µm and diameter d1=0.5×Λ, radius for 3rd and 4th layer air holes r3=r4=0.5×Λ and diameter d2=1×Λ, Elliptical core's semi major axis and semi minor axis are respectively a=2×r, b=r parameters are same as before doping. For 10% doping concentration at 1.55 µm wavelength the proposed model is simulated. The observed two dimensional and three dimension electric mode field is shown below.

Fig. 3.9: (a) Electric field distribution of BaF$_2$ doped SiO$_2$ (b) 3D Electric field distribution of BaF$_2$ doped SiO$_2$ for pitch, Λ =1.55μm at 10% doping concentration.

In addition, data for X=30% doping concentration, pitch Λ=1.55 μm, radius for 1st and 2nd layer air holes are r1=r2=0.3875 μm and diameter d1=0.5×Λ, radius for 3rd and 4th layer air holes r3=r4=0.5×Λ and diameter d2=1×Λ, Elliptical core's semi major axis and semi minor axis are respectively a=2×r, b=r parameters are same as before doping. For 30% doping concentration at 1.55 μm wavelength 2-Dimensional and 3-Dimension electric mode field is presented below.

Fig. 3.10: (a) Electric field distribution of BaF$_2$ doped SiO$_2$ (b) 3D Electric field distribution of BaF$_2$ doped SiO$_2$ for pitch, Λ =1.55μm at 30% doping concentration.

Also, data for X=40% doping concentration, pitch Λ=1.55 µm, radius for 1st and 2nd layer air holes are r1=r2=0.3875 µm and diameter d1=0.5×Λ, radius for 3rd and 4th layer air holes r3=r4=0.5×Λ and diameter d2=1×Λ, Elliptical core's semi major axis and semi minor axis are respectively a=2×r, b=r parameters are same as before doping.

For 40% doping concentration at 1.55 µm wavelength 2-Dimensional and 3-Dimension electric mode field is presented below.

Fig. 3.11: (a) Electric field distribution of BaF_2 doped SiO_2 (b) 3D Electric field distribution of BaF_2 doped SiO_2 for pitch, Λ =1.55µm at 40% doping concentration.

Additionally, data for X=50% doping concentration, pitch Λ=1.55 µm, radius for 1st and 2nd layer air holes are r1=r2=0.3875 µm and diameter d1=0.5×Λ, radius for 3rd and 4th layer air holes r3=r4=0.5×Λ and diameter d2=1×Λ, Elliptical core's semi major axis and semi minor axis are respectively a=2×r, b=r parameters are same as before doping.

For 50% doping concentration at 1.55 µm wavelength 2-Dimensional and 3-Dimension electric mode field is as following.
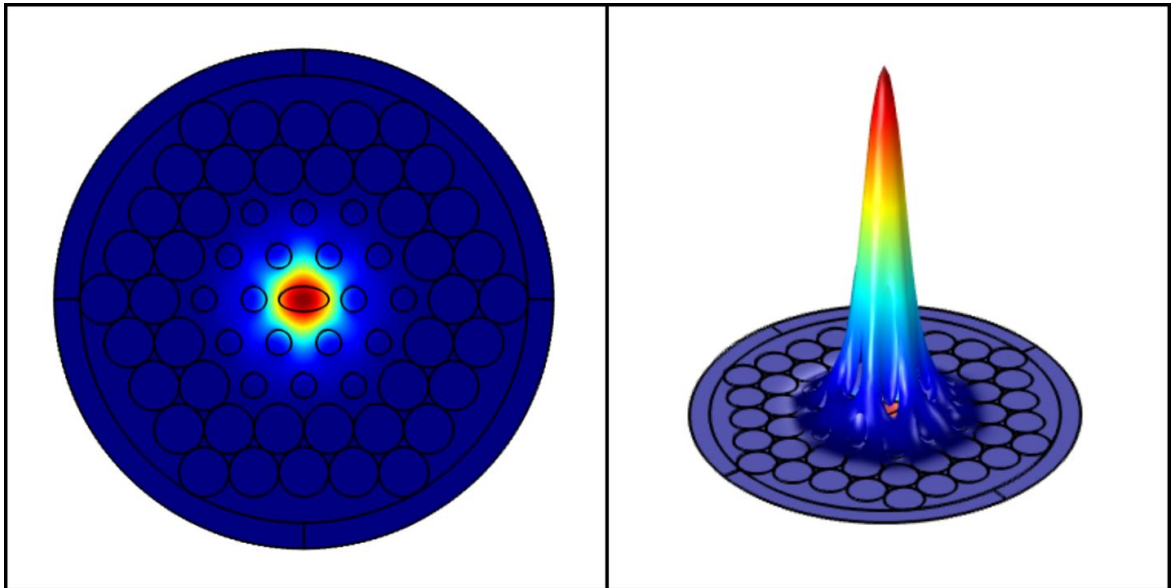
Fig. 3.12: (a) Electric field distribution of BaF$_2$ doped SiO$_2$ (b) 3D Electric field distribution of BaF$_2$ doped SiO$_2$ for pitch, Λ =1.55µm at 50% doping concentration.

Including data for X=60% doping concentration, pitch Λ=1.55 µm, radius for 1st and 2nd layer air holes are r1=r2=0.3875 µm and diameter d1=0.5×Λ, radius for 3rd and 4th layer air holes r3=r4=0.5×Λ and diameter d2=1×Λ, Elliptical core's semi major axis and semi minor axis are respectively a=2×r, b=r parameters are same as before doping. For 60% doping concentration at 1.55 µm wavelength 2-Dimensional and 3-Dimension electric mode field is given below.
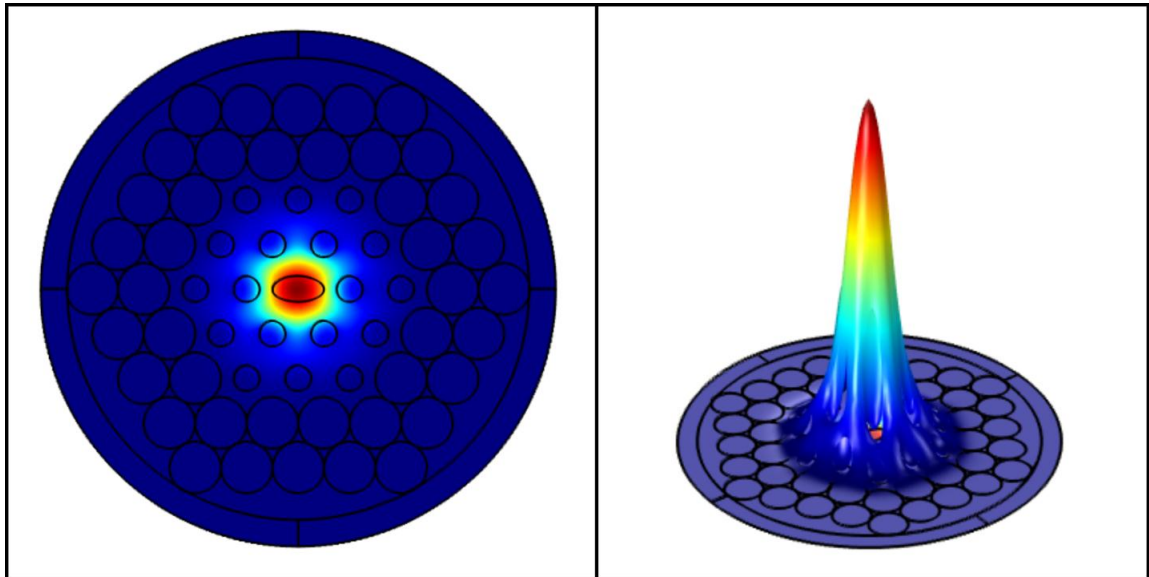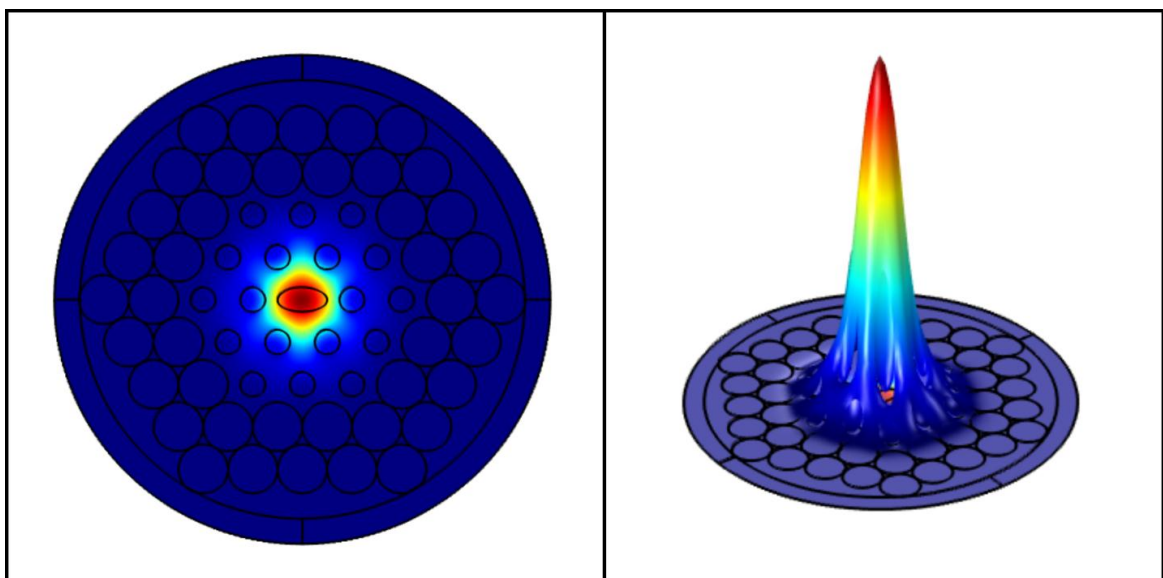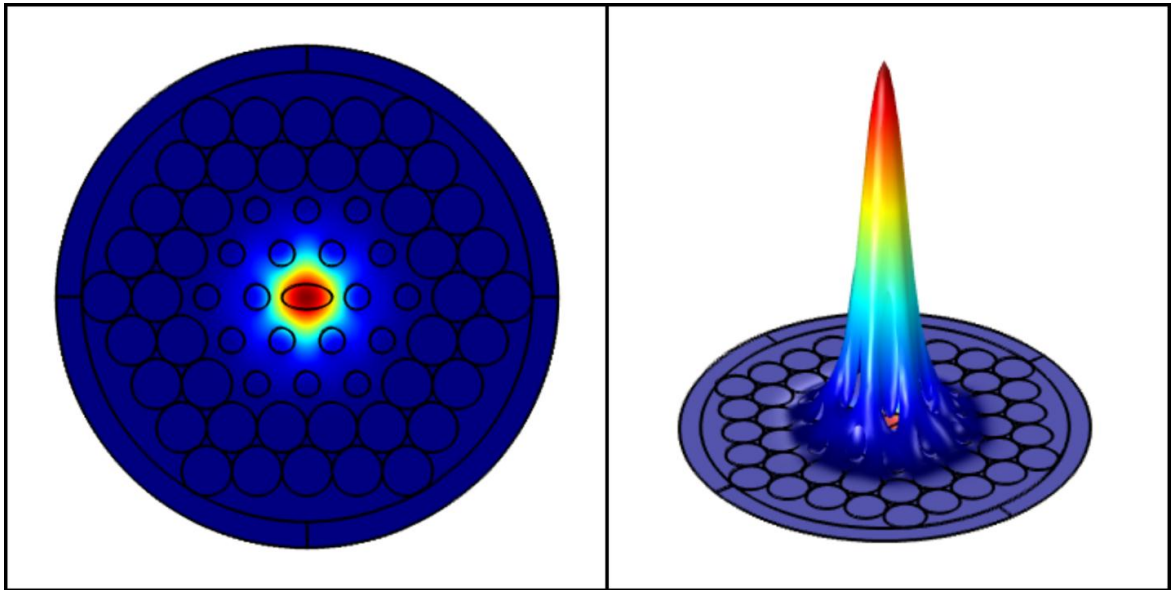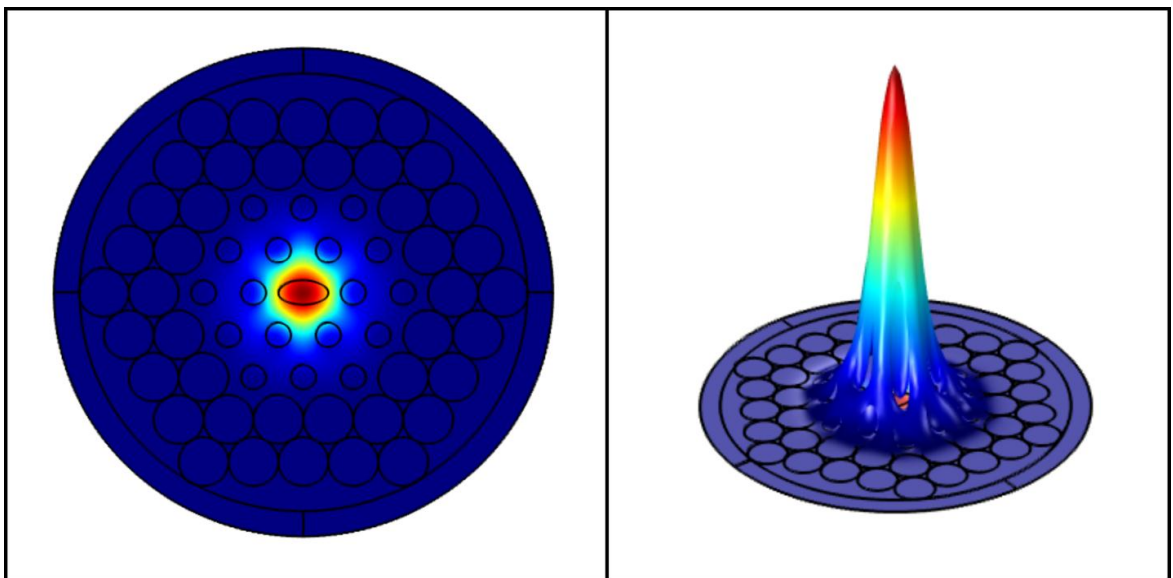

Fig. 3.13: (a) Electric field distribution of BaF$_2$ doped SiO$_2$ (b) 3D Electric field distribution of BaF$_2$ doped SiO$_2$ for pitch, Λ =1.55µm at 60% doping concentration.

3.2.5 Analysis or Effect of Changing Doping Concentrations

It is known that, in the best ray passing model, the light is strongly confined in the central core region, i.e. the central core region has the highest magnetic field density for a specific model. In order to find the best possible outcome, the resultant effective mode index and doping concentration have changed for various times and find which has most of the light passing through the central region and thus find the desired value of effective mode index for any wavelength. Doping material and concentration have also effect on electric field distribution. As the doping increases the light gets stronger in the central region.
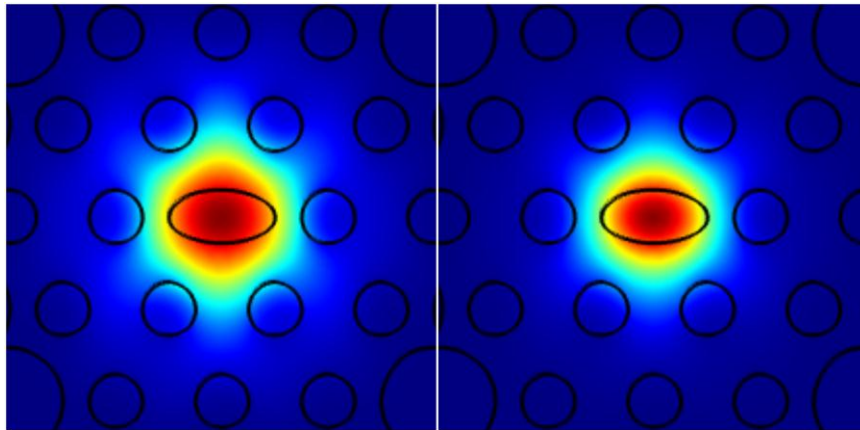
Fig. 3.14: Surface electric field distribution at a wavelength 1.55 μm (a) for 10% doping concentration (b) for 60% GeO_2 doping concentration.

Comparative figures of the proposed design of GeO_2 doped SiO_2 for pitch, Λ =1.55 μm at 1.55 μm wavelength are shown in above Fig. 3.14. From 60% doping to 10% doping the ray get closer to the core region. It varies with the doping concentration.
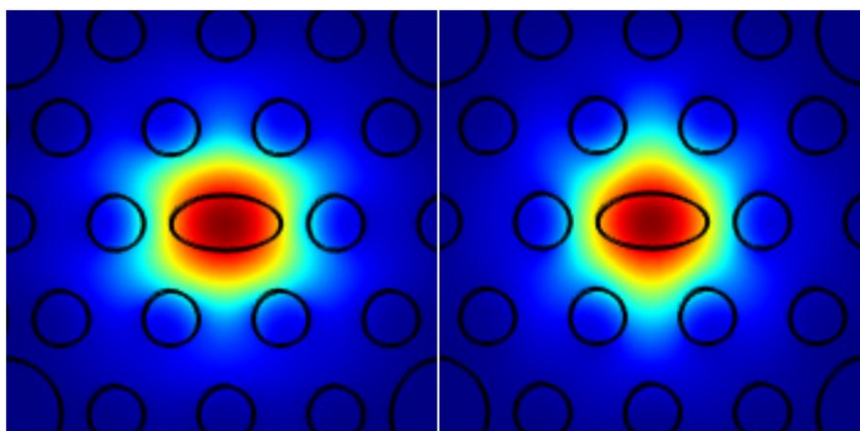
Fig. 3.15: Surface electric field distribution at a wavelength 1.55 μm (a) for 10% doping concentration (b) for 60% BaF_2 doping concentration.

The electric field distribution doesn't remain same for the variation of doping elements. The variation for BaF_2 is much more negligible then GeO_2. But still it can be seen in the comparative figure of BaF_2 doped SiO_2 for pitch, $\Lambda = 1.55$ μm at 1.55 μm which is shown Fig. 3.15.

3.2.5 Conclusion

Pure Silica core makes the wave propagation characteristics fixed, for a particular set of parameters, whereas the design can modify the electric field and hence the optical wave propagation characteristics by changing the doping concentration and material. Among the variants studied, the main focus was to achieve a range of flattened dispersion and modified non-linearity which elaborately discussed in the next chapter.

CHAPTER 4
RESULT AND ANALYSIS

4.1   Introduction

The proposed H-PCF is simulated in COMSOL Multiphysics 4.3 by varying different parameters of the fiber. The single core hexagonal fiber's core is doped with two different materials (GeO_2 and BaF_2). Results of different parameters are noted in a broad range of wavelength by varying doping percentage. All other design parameters (air hole diameters, pitch etc.) are kept constant. The simulated results are plotted using MATLAB 7.6. Important MATLAB codes are attached in Appendix 1. The necessary data tables of different parameters, relevant plots and their analysis are described in this chapter.

4.2   Analysis of H-PCF Model Without Doping

4.2.1   Analysis of Effective Mode Index Without Doping

Simulating the H-PCF model, the effective mode index (η_{eff}) of H-PCF is found. When fiber core is not doped, the core and cladding material is SiO_2. The real part of effective mode index (η_{eff}) is taken into account. Equation (2.16) is applied for calculating the effective mode index of H-PCF. For without doping at pitch, $\Lambda=1.55$ µm required data sets are received for respective wavelength to formulate the plots.
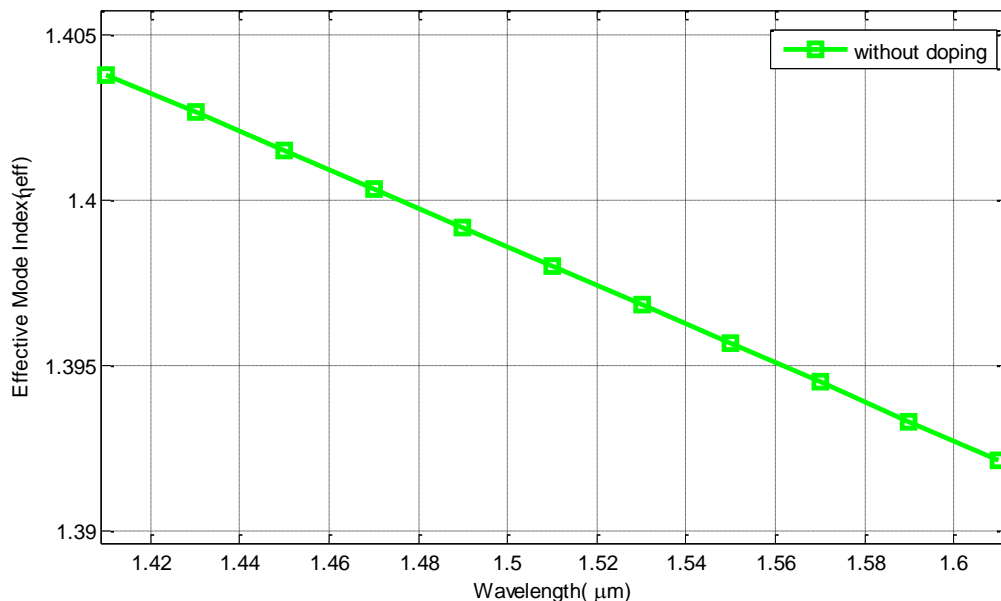
Fig. 4.1: Plot of Effective mode index as a function of wavelength for without doping at pitch, Λ =1.55 µm.

Effective mode index and respective wavelength is plotted in Fig. 4.1. From Fig. 4.1 it is seen that, effective mode index decreases as wavelength increases. At 1.55 µm wavelength effective mode index is 1.395679.

4.2.2 Analysis of Effective Mode Area Without Doping

Effective mode area of the designed PCF model is calculated using equation (2.12). Values which are taken from COMSOL simulation, is used to plot the mode area against wavelength.

Fig. 4.2 shows effective mode area (A_{eff}) against wavelength at pitch, Λ = 1.55 µm for without doping or 0% doping. From the Fig. 4.2 it is observed that effective area increases linearly with increase in wavelength. Simulation data of (emw.normE)^2 and(emw.normE)^4 are taken from COMSOL. From plot it is also noticed that the proposed model has an effective area of 5.0717 μm^2 for without doping at 1.55 µm wavelength.
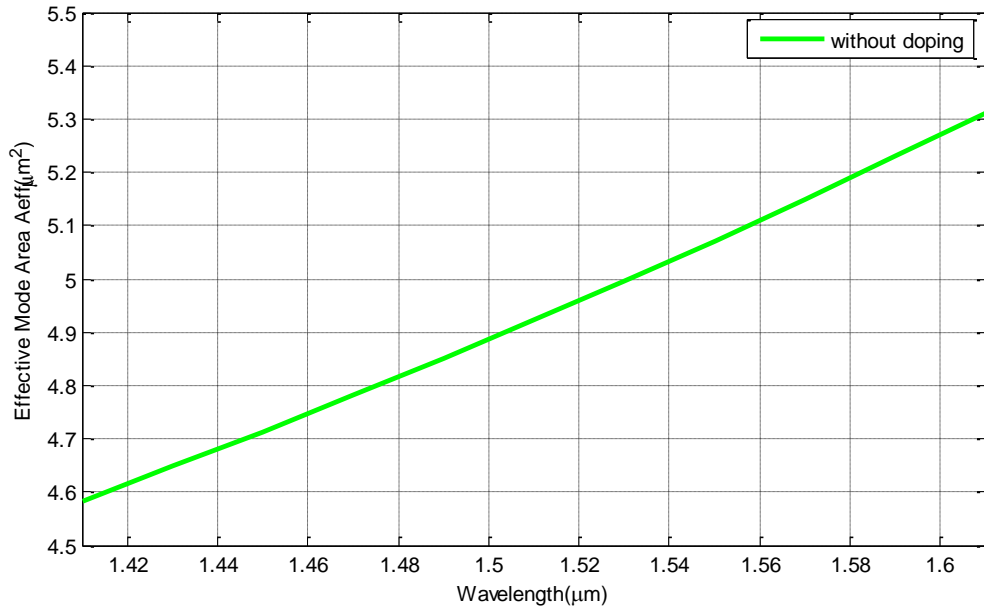
Fig. 4.2: Plot of Effective mode area as a function of wavelength for without doping at pitch, Λ = 1.55 µm.

4.2.3 Analysis of Dispersion Without Doping

Chromatic Dispersion of the proposed H-PCF is calculated from equation (2.5). For without doping, obtained results for dispersion parameter is plotted against wavelength. At

1.371 μm wavelength, dispersion is 0.1449 ps/(nm.km). Then dispersion stars rising. From 1.426 μm to 1.449 μm, dispersion is almost flattened. Fluctuation is seen at several wavelengths from 1.45 μm to 1.59 μm. Then dispersion becomes negative. At 1.426 μm, 1.449 μm and 1.591 μm wavelengths dispersion are respectively 0.9436 ps/(nm.km), 0.9667 ps/(nm.km) and -0.05364 ps/(nm.km). Furthermore, at 1.61 μm dispersion is -1.57 ps/(nm.km).
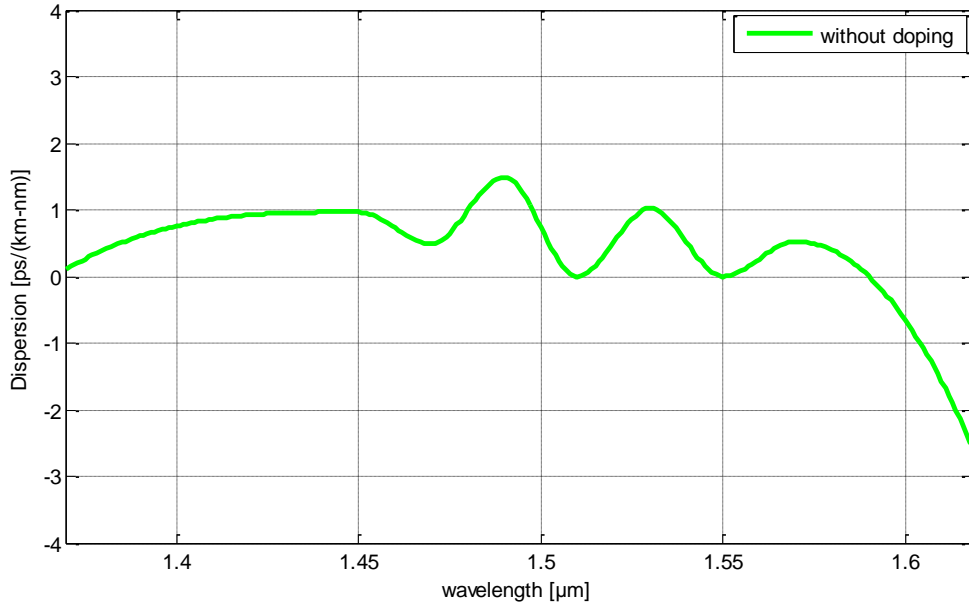
Fig. 4.3: Plot of Dispersion as a function of wavelength for without doping at pitch, $\Lambda =$ 1.55 μm.

4.3   Analysis of H-PCF Model with Doping

4.3.1   Analysis of Effective Mode Index with GeO_2 Doping

The effective mode index of GeO_2-SiO_2 of H-PCF is found similarly simulating the proposed model in COMSOL. Equation (2.16) is used for the calculation of mode index. Different doping concentrations of GeO_2-SiO_2 of the model are taken into consideration. 10%, 30%, 40%, 50% and 60% doping concentrations are used to analyze the behavior of the model. From COMSOL the results of effective mode index at 10% doping concentration of GeO_2-SiO_2 is noted.

In Fig. 4.4 the effective mode index (η_{eff}) is plotted as a function of wavelength at pitch, $\Lambda = 1.55$ μm using 10% doping concentration of GeO_2-SiO_2. Simulation data from COMSOL is used to plot the Fig. 4.4. At 1.55 μm effective mode index is 1.40057 for

51

10% doping. Effective mode index at 1.55 µm wavelength is 1.395679 for 0% doping. So, it is noticed that effective mode index increases after GeO₂ doping.

Doping concentration of GeO₂-SiO₂ is gradually increased to study the effect of doping on the proposed H-PCF structure. 30%, 40%, 50% and 60% doping concentrations of GeO₂-SiO₂ are also taken into consideration.
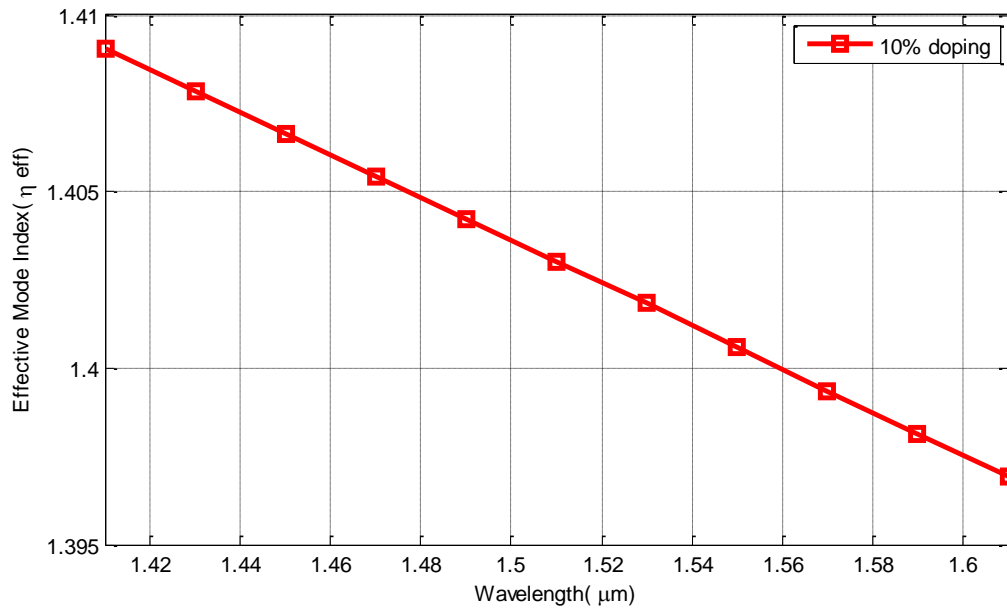
Fig. 4.4: Plot of Effective mode index as a function of wavelength for 10% doping of GeO₂-SiO₂ at pitch, Λ = 1.55 µm
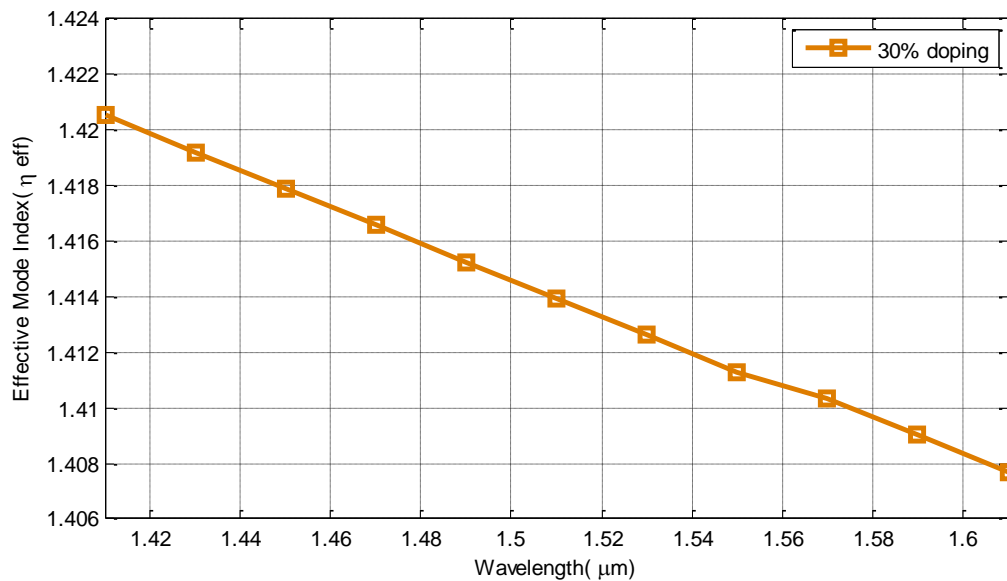
Fig. 4.5: Plot of Effective mode index as a function of wavelength for 30% doping of GeO₂-SiO₂ at pitch, Λ = 1.55 µm

In Fig. 4.5 effective mode index is plotted as function of wavelength at 30% doping concentration using data from COMSOL for pitch, $\Lambda = 1.55$ μm. At 1.55 μm wavelength effective mode index is 1.411287 for 30% doping. For 10% doping effective mode index is 1.40057. So, effective mode index increases with increasing of doping percentage.
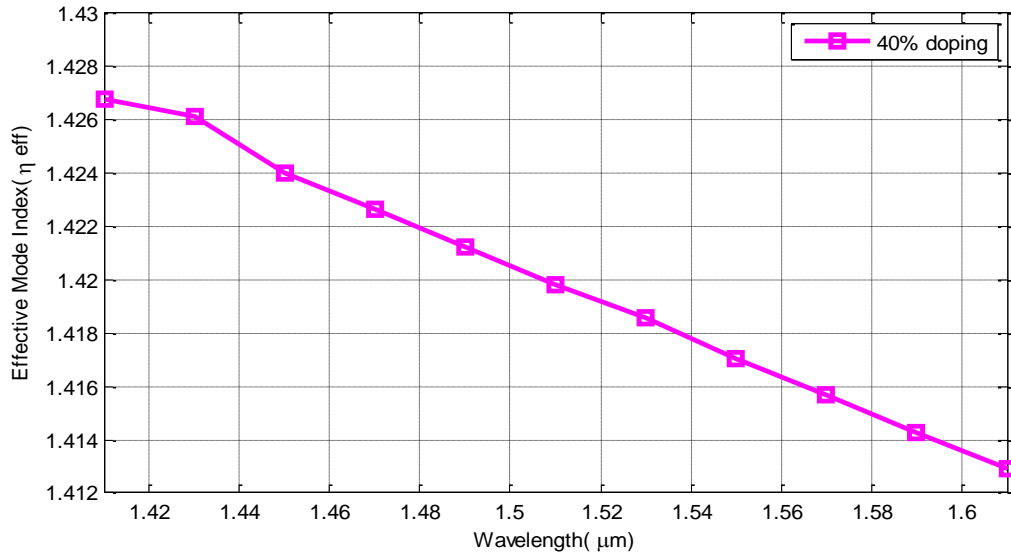
Fig. 4.6: Plot of Effective mode index as a function of wavelength for pitch, $\Lambda =1.55$ μm at 40% doping concentration of GeO_2-SiO_2
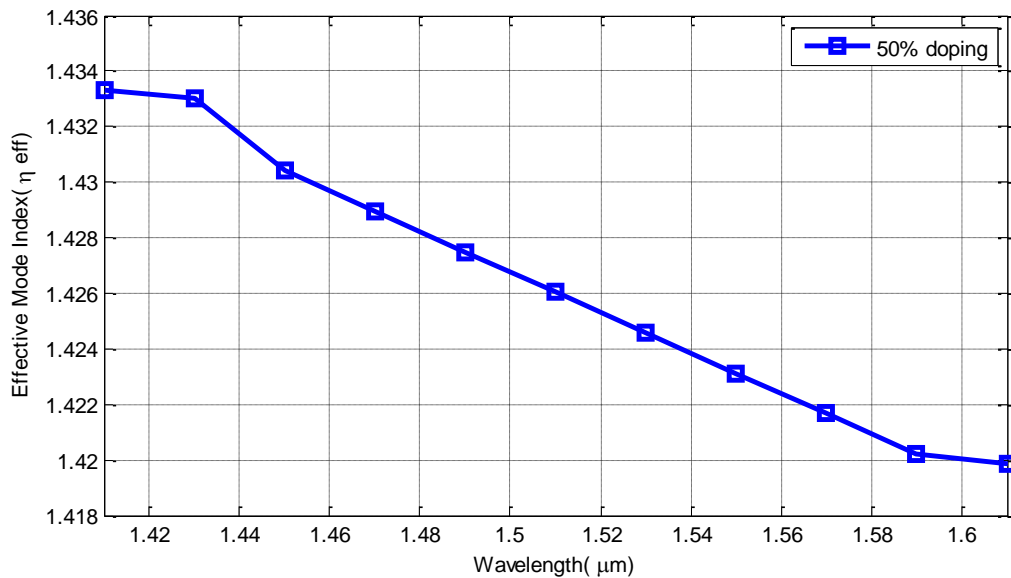
Fig. 4.7: Plot of Effective mode index as a function of wavelength for pitch, $\Lambda =1.55$ μm at 50% doping concentration of GeO_2-SiO_2

In Fig. 4.6 effective mode index for 40% doping concentration of GeO_2-SiO_2 is plotted. It is seen that effective mode index values are more than the previous two doping (10%,

30%) concentrations. The effective mode index's curve shows almost linear pattern and increases with decreasing of wavelengths. At 1.55 μm effective mode index is 1.417073 for 40% doping.

The Fig. 4.7 shows effective mode index for pitch, Λ = 1.55 μm at 50% doping concentration of GeO_2 doped silica. Effective mode index is maximum at 1.41 μm wavelength. Then it starts decreasing. At 1.55 μm wavelength effective mode index is 1.423125 for 50% doping. Fluctuation is seen at 1.43 μm and 1.59 μm wavelengths.

In Fig. 4.8 effective mode index for 60% doing of GeO_2-SiO_2 at pitch Λ = 1.55 μm is shown. It shows same behavior which is mode index decreases with increasing of wavelength as it is for 10%, 30%, 40% and 50% doping concentrations.
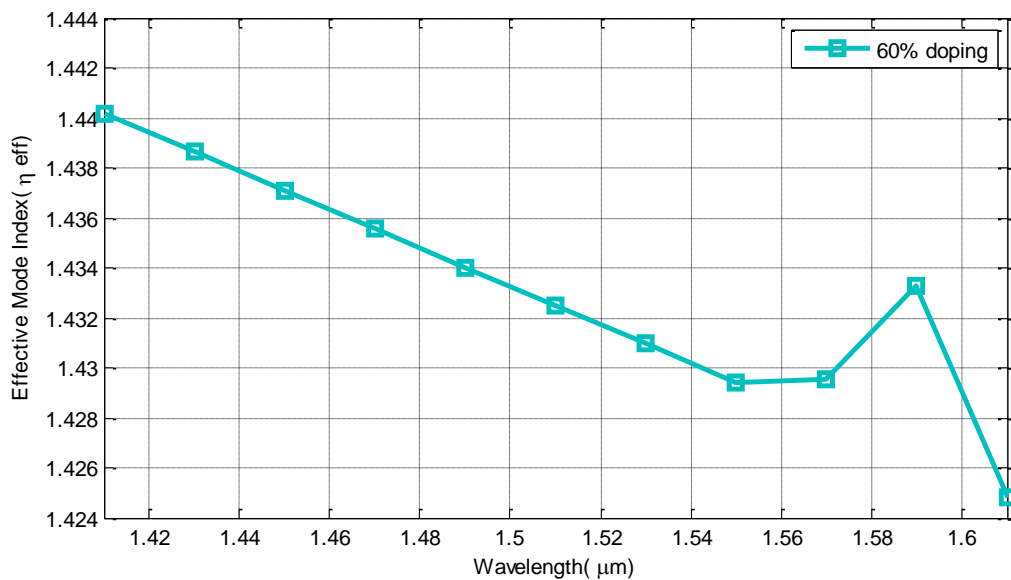
Fig. 4.8: Plot of Effective mode index as a function of wavelength for pitch, Λ =1.55 μm at 60% doping concentration of GeO_2-SiO_2.

Fig. 4.9 shows combine plot of effective mode index for 10%, 30%, 40%, 50% and 60% doping concentrations of GeO_2 doped silica. Minimum value of effective index is found for 10% doping concentration. Then, with increasing doping effective mode index increases and maximum value of effective mode index is found for 60% doping. At 1.55 μm effective mode index are 1.400574, 1.411287, 1.417073, 1.423125, 1.429428 for respectively 10%, 30%, 40%, 50% and 60% doping concentrations. Little fluctuation is seen for 60% doping from 1.57 μm to 1.61 μm. At 1.55 μm wavelength effective mode index is 1.395679 for 0% doping. Comparing the results, it can be said that after doping with GeO_2 effective mode index increases. Again, at 1.47 μm wavelength effective mode

index are 1.400346, 1.404212, 1.416577, 1.422623, 1.428959, 1.435568 respectively for 0%, 10%, 30%, 40%, 50% and 60% doping concentrations of GeO_2-SiO_2.

Fig. 4.9: Plot of Effective mode index as a function of wavelength for pitch, Λ =1.55 μm at 10%, 30%, 40%, 50% and 60% doping concentrations of GeO_2-SiO_2.

4.3.2   Analysis of Effective Mode Area with GeO$_2$-SiO$_2$ Doping

Effective mode area for GeO_2-SiO_2 is calculated using equation (2.12). Effective mode area for 10%, 30%, 40%, 50% and 60% doping are calculated and the result is compared with each other to analyze the effect of doping on mode area of our proposed H-PCF model. The effective mode area is plotted against wavelength using the simulation data from COMSOL and MATLAB code attached in Appendix 1.

Fig. 4.10 shows that effective mode area increases with increasing of wavelength at 10% doping concentration. At 1.55 μm effective mode area is 5.0717 μm^2 and 4.6292 μm^2 for respectively 0% and 10% doping concentration of GeO_2. So, effective mode area decreases with increasing doping concentration of GeO_2.

Fig. 4.11 shows that effective mode area for 30% doping concentration of GeO_2 doped Silica. At 1.55 μm wavelength effective mode area is 4.6292 μm^2 and 3.9357 μm^2 for respectively 10% and 30% doping of GeO_2. Again, effective mode area decreases with increasing of doping concentration. Effective mode area increases with increasing

wavelength but after 1.55 μm wavelength effective mode area suddenly starts decreasing. After 1.57 μm wavelength it starts increasing.
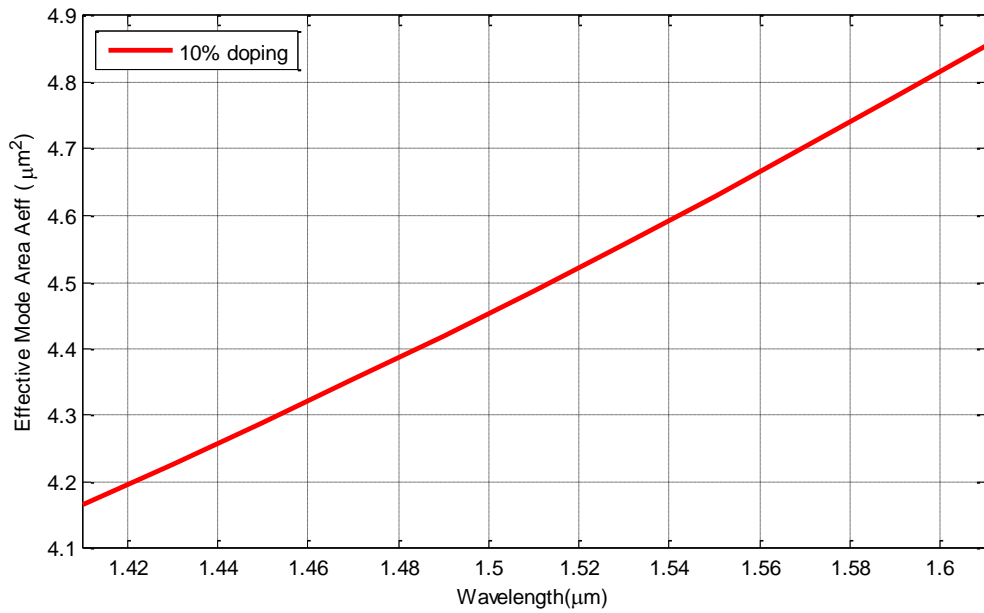
Fig. 4.10: Plot of Effective mode area as a function of wavelength for pitch, Λ =1.55 μm, at 10% doping concentration of GeO_2-SiO_2.
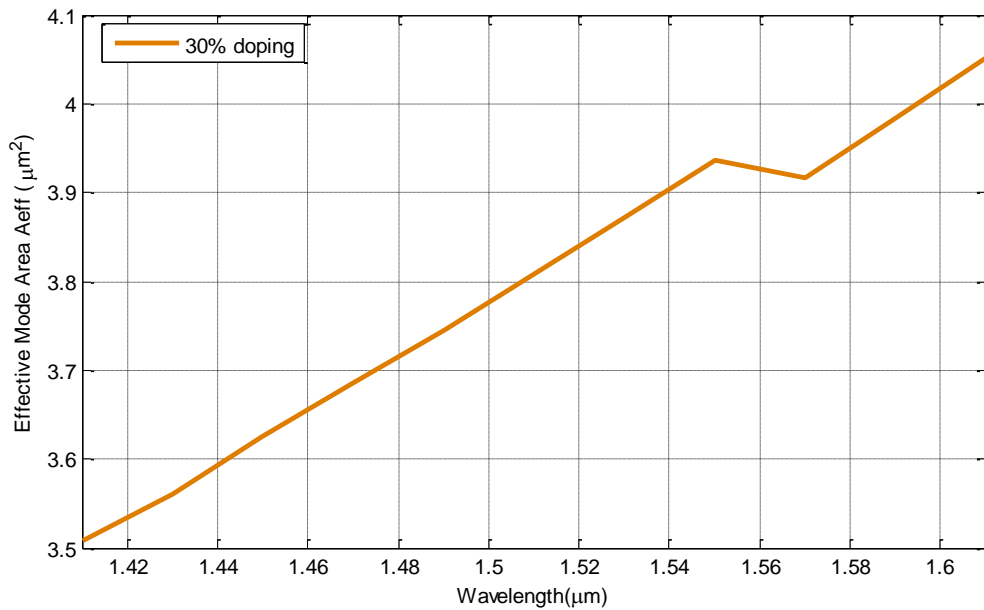
Fig. 4.11: Plot of Effective mode area as a function of wavelength for 30% doping concentration of GeO_2-SiO_2 at pitch, Λ =1.55 μm.

Fig. 4.12 shows that effective mode area at 40% doping concentration of GeO_2 doped Silica. From 1.41 μm to 1.43 μm effective mode area decreases. After 1.43 μm effective mode area starts increasing. There is little fluctuation at 1.45 μm wavelength.

Also, in Fig. 4.12 at 1.55 μm wavelength effective mode area for 40% doping concentration is 3.6598 μm^2.
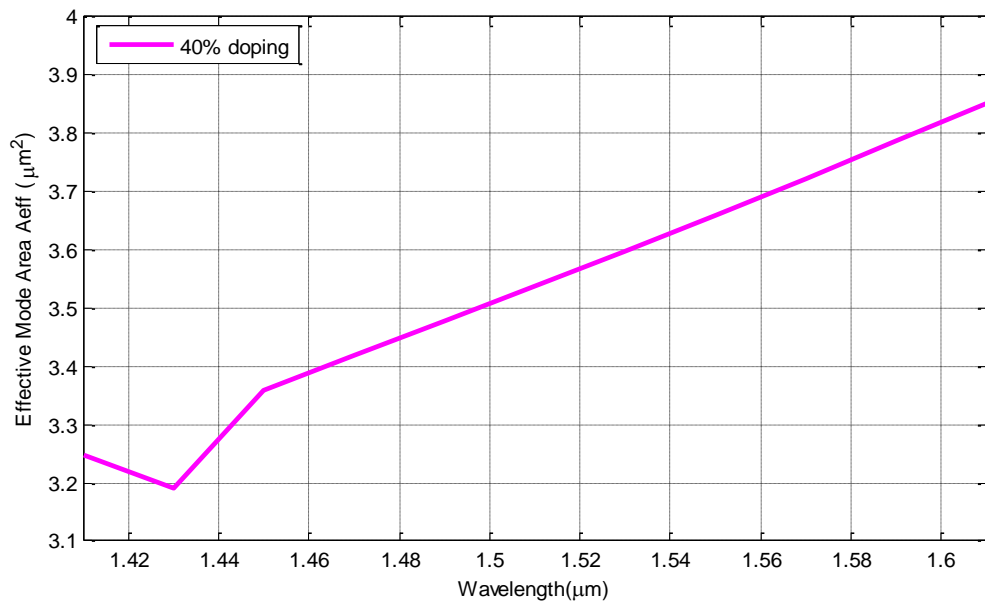
Fig. 4.12: Plot of Effective mode area as a function of wavelength for 40% doping concentration of GeO$_2$ doped SiO$_2$ at pitch, Λ =1.55 μm.

In Fig. 4.13 effective mode area is plotted against wavelength for 50% doping concentration of GeO$_2$ doped SiO$_2$. Effective area increases with wavelength but after 1.59 μm wavelength, effective area starts decreasing. The change is not much significant.
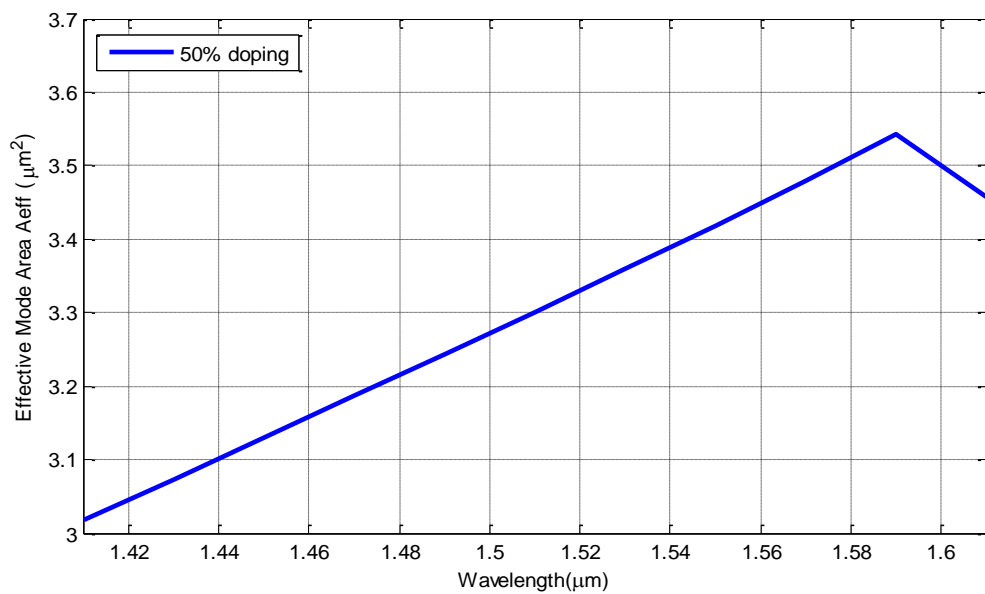
Fig. 4.13: Plot of Effective mode area as a function of wavelength for pitch, Λ =1.55 μm, at 50% doping concentration of GeO$_2$ doped SiO$_2$.

Again, in Fig. 4.13 at 1.55 μm wavelength effective mode area is 3.4193 μm^2 for 50% doping.

In Fig. 4.14 effective area is plotted against wavelength for 60% doping concentration of GeO$_2$ doped SiO$_2$ for pitch 1.55 μm. The curve plotted in MATLAB using simulation data from COMSOL.

At 1.55 μm wavelength effective mode area is 3.20813 μm^2. The plot is almost linear.
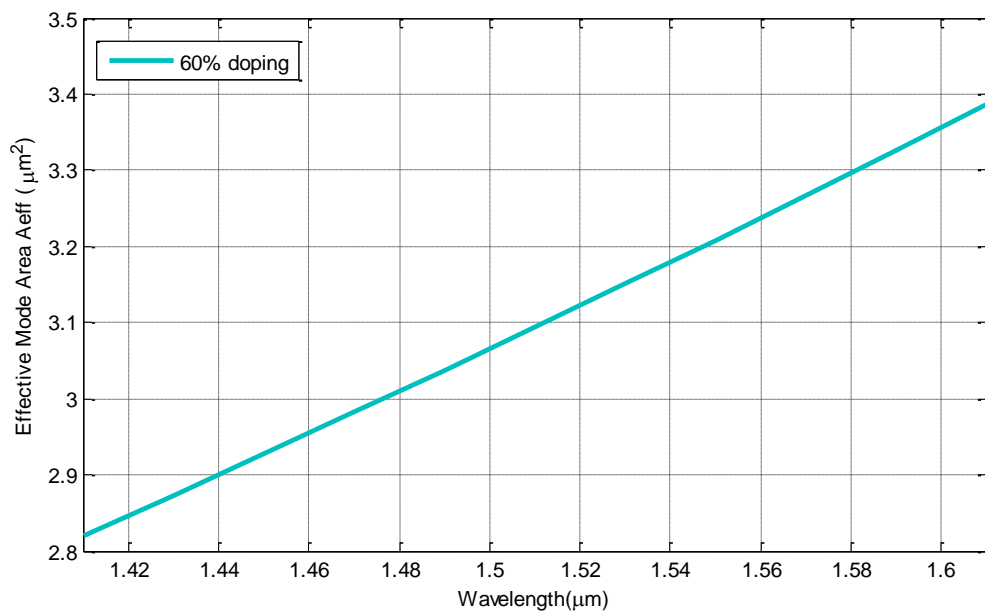
Fig. 4.14: Plot of Effective mode area as a function of wavelength for pitch, Λ =1.55 μm, at 60% doping concentration of GeO$_2$ doped SiO$_2$.

The Fig. 4.15 shows effective mode area against wavelength for all doping concentrations such as 10%, 30%, 40%, 50% and 60%. From the plot it is seen that with increasing wavelength effective mode area increases but with increasing of doping it decreases.

Maximum value of effective area is found for 10% doping concentration. Minimum value of effective area is for 60% doping concentration.

Again, at 1.55 μm wavelength effective area are respectively 4.6292 μm^2, 3.9357 μm^2, 3.6598 μm^2, 3.4193 μm^2, 3.2081 μm^2 for 10%, 30%, 40%, 50% and 60% doping concentrations. At 1.57 μm wavelength effective mode area is 4.7027 μm^2, 3.9161 μm^2, 3.7231 μm^2, 3.4801 μm^2, 3.2667 μm^2 for respectively 10% ,30%, 40%, 50% and 60% doping concentrations.

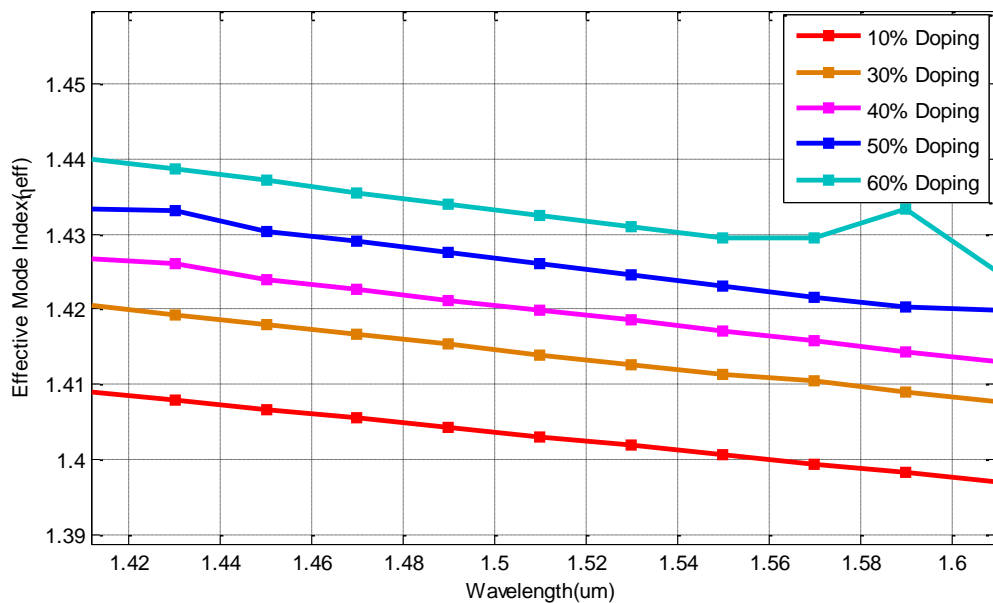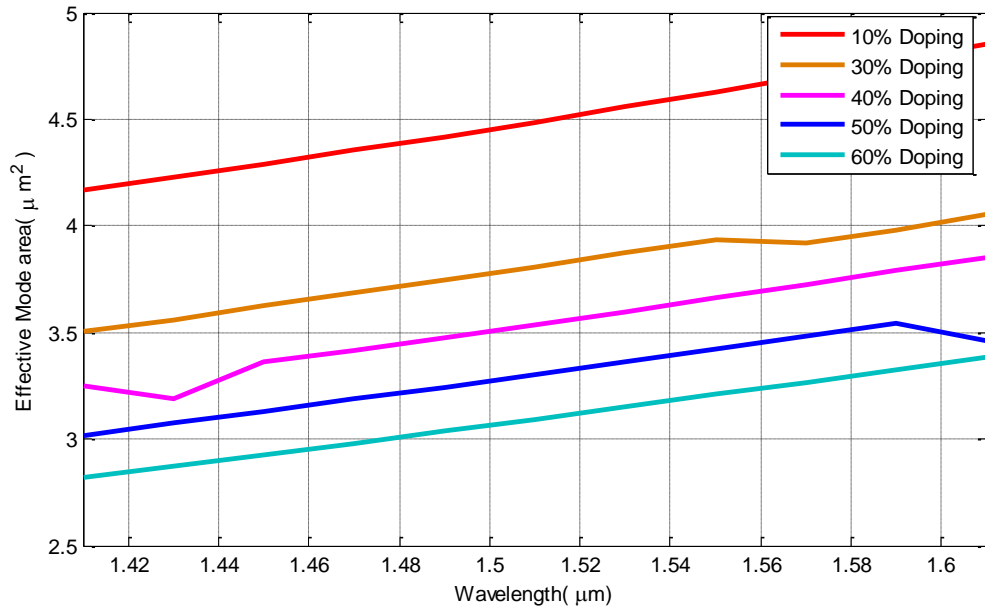**Fig. 4.15**: Plot of Effective mode area as a function of wavelength for pitch, Λ =1.55 μm, at 10%, 30%, 40%, 50% and 60% doping concentrations of GeO_2 doped SiO_2

4.3.3 Analysis of Dispersion with GeO_2 Doped Silica Doping

Dispersion of proposed GeO_2 doped silica hexagonal single core fiber is calculated. Again 10%, 30%, 40%, 50% and 60% doping concentrations of GeO_2 are considered. From COMSOL real value of effective mode index is noted by simulating the model for various concentrations. Using these real values of effective mode index in MATLAB, dispersion is calculated. Finite element method is used in calculating dispersion.

In Fig. 4.16 dispersion for 10% doping concentration of GeO_2 doped silica is shown. Dispersion is calculated using equation (2.5). For 10% doping from the plot it is noticed that there is a flattened range from 1.401 μm to 1.452 μm. In this range dispersion varies from 1.156 ps/(nm.km) to 1.396 ps/(nm.km). Small variation of dispersion is seen from 1.452 to 1.49 μm wavelength. Then there is a sharp fall and the dispersion falls up to -20.17 ps/(nm.km) which is at 1.511 μm wavelength. After 1.511 μm wavelength there is sharp rise up to 44.37 ps/(nm.km) for 1.53 μm wavelength. Then dispersion curve starts falling and falls up to -21.7 ps/(nm.km). -21.7 ps/(nm.km) dispersion is noted at 1.55 μm wavelength. After -21.7 ps/(nm.km) dispersion curve starts rising. Again, a flattened range is seen from 1.57 μm to 1.61μm wavelength and in this range dispersion varies from -3.553 $\times10^{-15}$ to -0.1755 ps/(nm.km). The Proposed H-PCF has dispersion of 0.05659

ps/(nm.km) at 1.463 µm wavelength for 10% doping concentration, which is nearly zero. At 1.500 µm, it shows dispersion of -9.573 ps/(nm.km) which is negative dispersion.
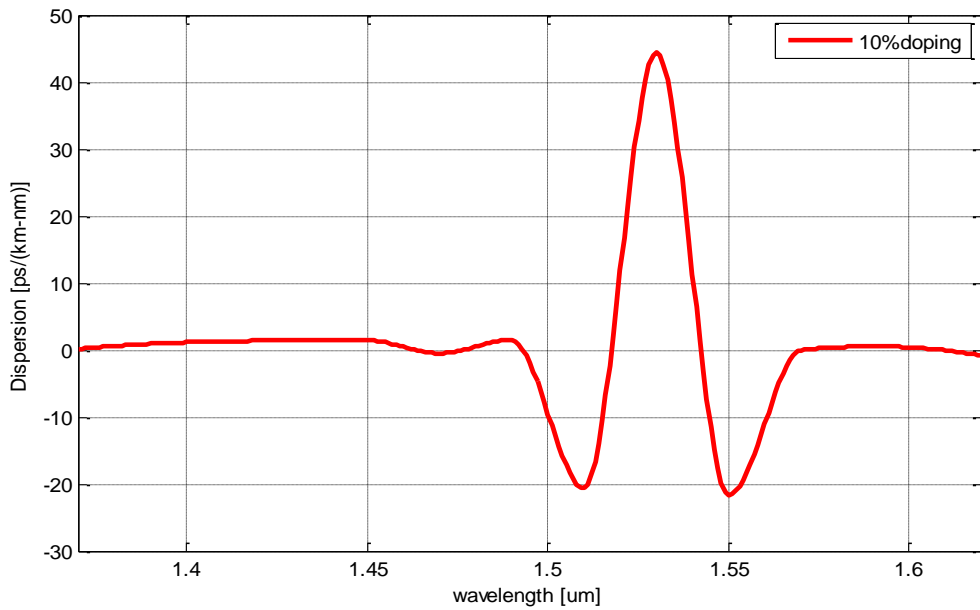
Fig. 4.16: Plot of Dispersion as a function of wavelength for 10% doping concentration of GeO$_2$-SiO$_2$ at pitch, Λ = 1.55 µm.
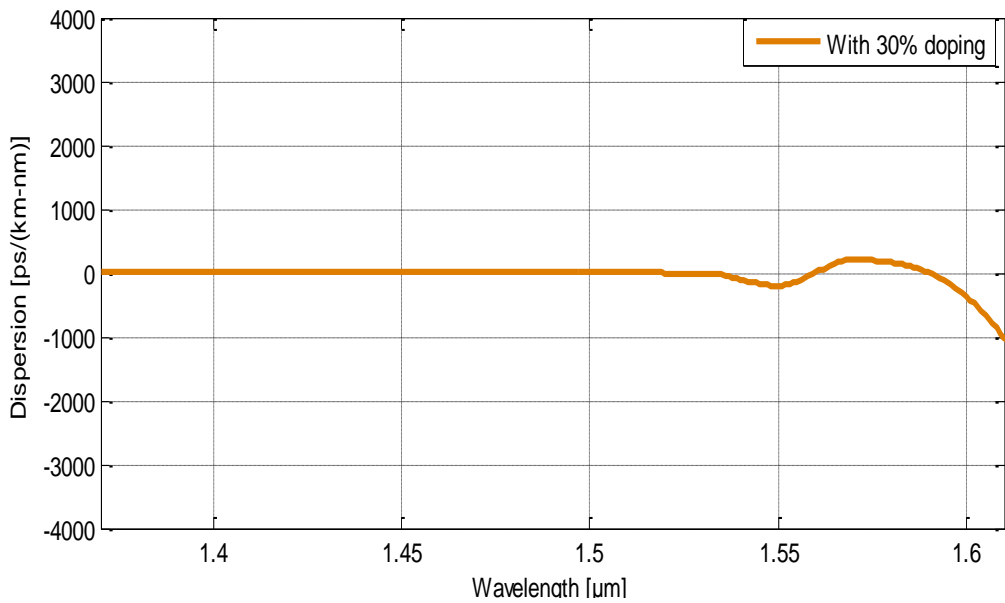
Fig. 4.17: Plot of Dispersion as a function of wavelength for 30% doping concentration of GeO$_2$-SiO$_2$ at pitch, Λ = 1.55 µm

Fig. 4.17 shows dispersion for 30% doping concentration of GeO$_2$ doped silica. From the plot it is seen that from 1.371 µm to 1.533 µm wavelength dispersion curve is almost flattened. In this range dispersion varies from 0.457 ps/(nm.km) to -12.21 ps/(nm.km).

Then small variation is seen and dispersion curve becomes negative. After -201 ps/(nm.km) at 1.55 µm wavelength the dispersion curve starts rising and rises up to 200.2 ps/(nm.km). After that it starts falling and falls up to -1017 ps/(nm.km) at 1.61 µm wavelength.
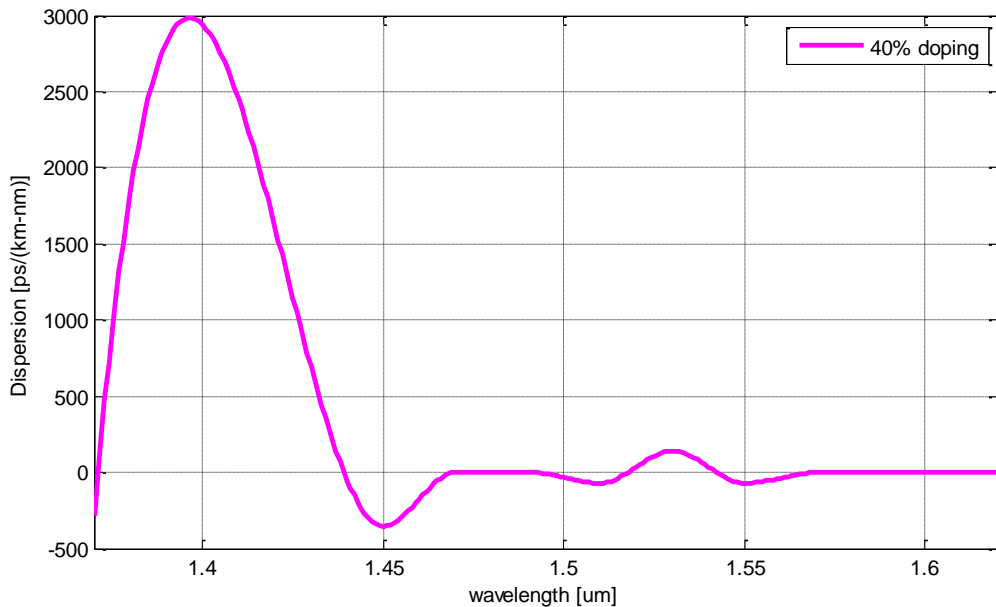
Fig. 4.18: Plot of Dispersion as a function of wavelength for 40% doping concentration of GeO$_2$-SiO$_2$ at pitch, $\Lambda = 1.55$ µm

Fig. 4.18 shows dispersion for 40% doping concentration of GeO$_2$ doped silica. Dispersion curve starts at 1.37 µm wavelength. In this wavelength dispersion is -278.8 ps/(nm.km). After this wavelength dispersion curve rises up to 2981 ps/(nm.km) which is at 1.397 µm wavelength. After 2981 ps/(nm.km) it starts falling and falls up to -352.8 ps/(nm.km) at 1.45 µm wavelength. Again, the curve starts rising and goes towards zero dispersion. There is small flattened range starting from 1.469 µm to 1.494 µm wavelength and in this range dispersion varies from -2.603 to -6.884 ps/(nm.km). Fluctuation of dispersion can be found from 1.494 µm to 1.566 µm wavelength. Again, from 1.566 µm to 1.61 µm dispersion curve is almost flattened and dispersion varies from -7.938 ps/(nm.km) to -0.5767 ps/(nm.km).

Fig. 4.19 shows dispersion curve for 50% doping of GeO$_2$. From plot it is found that dispersion curve starts at 1.37 µm wavelength having dispersion of -420.2 ps/(nm.km). Then it rises up to dispersion of 4717 ps/(nm.km) at 1.396 µm wavelength. After 4717 ps/(nm.km) the curve falls up to -554.7 ps/(nm.km) which is at 1.451 µm wavelength. A flattened range can be seen from 1.469 µm to 1.572 µm wavelength and in this range the dispersion varies from -4.051 ps/(nm.km) to -10. 31 ps/(nm.km). Then the curve starts

61

falling and falls up to value of -1172 ps/(nm.km) at 1.61 µm wavelength. After -1172 ps/(nm.km) it again starts rising. At 1.549 µm wavelength almost zero dispersion is found which is -0.003697 ps/(nm.km).
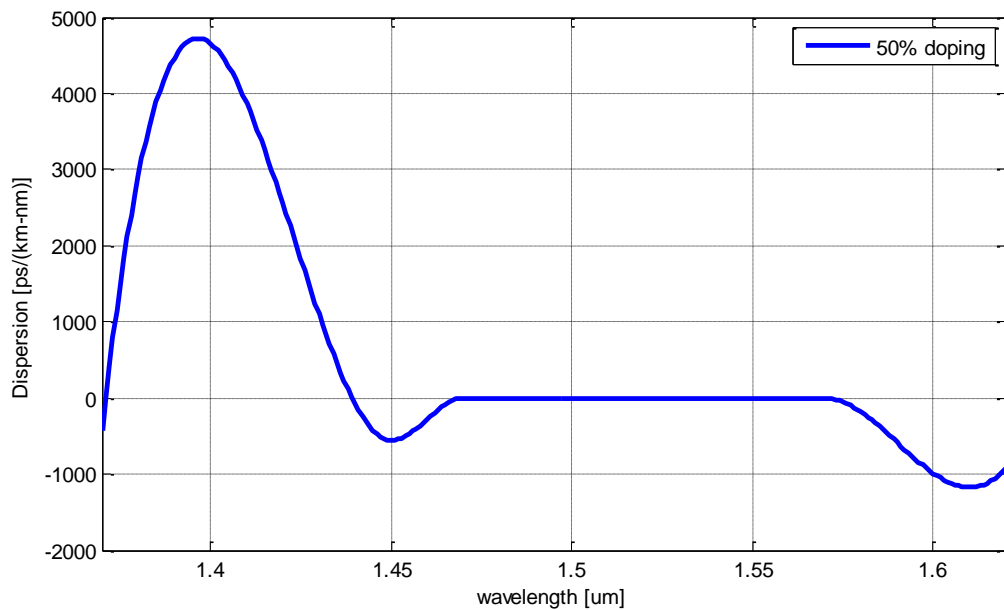
Fig. 4.19: Plot of Dispersion as a function of wavelength for 50% doping concentration of GeO$_2$-SiO$_2$ at pitch, Λ = 1.55 µm
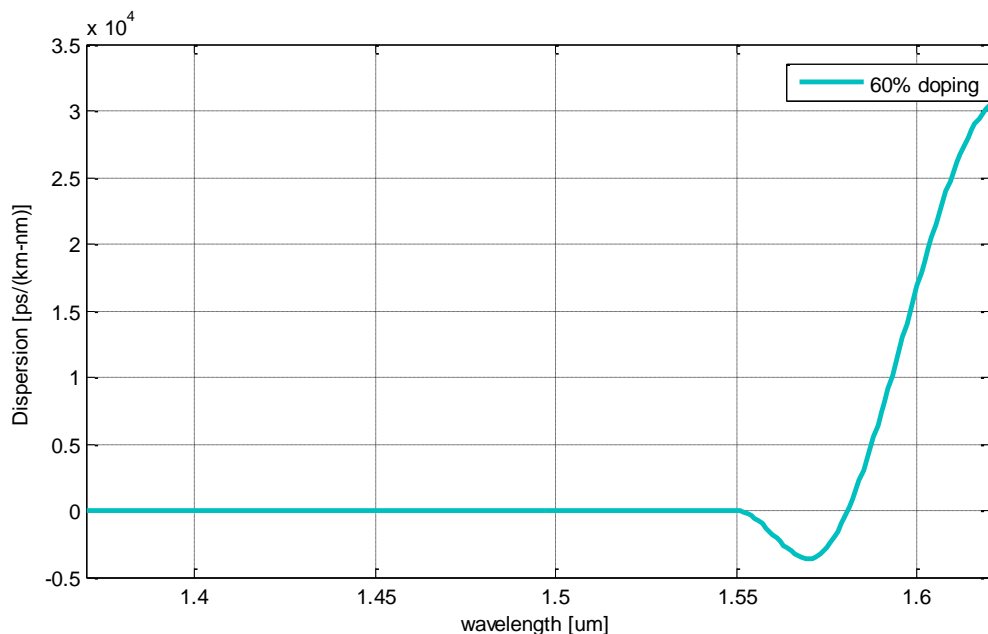
Fig. 4.20: Plot of Dispersion against wavelength for GeO$_2$-SiO$_2$ 60% doping concentration at pitch, Λ = 1.55 µm

In Fig. 4.20 dispersion versus wavelength curve is shown for 60% doping concentration of GeO$_2$ doped Silica H-PCF. From curve it is seen that the proposed GeO$_2$ doped Silica H-PCF has flattened range from 1.37 µm to 1.551 µm wavelength. In this range dispersion

varies from 5.857 ps/(nm.km) to -27.80 ps/(nm.km). The curve falls up to -3608 ps/(nm.km) which is at 1.57 µm wavelength. Then it stats rising and rises up to value of 2.543×10^4 ps/(nm.km) for 1.61 µm wavelength.

Fig. 4.21 shows combine dispersion against wavelength curve for 10%, 30%, 40%, 50% and 60% doping concentrations of GeO_2 doped silica. From plot it is seen that for 40% and 50% doping there is variation of dispersion from 1.371 to 1.467 µm wavelength. From 1.467 to 1.533 µm dispersion remains near zero and flattened for all doping concentration. In this range dispersion varies from -0.3721 ps/(nm.km) to 40.36 ps/(nm.km). After 1.533 µm wavelength dispersion becomes negative for 60% doping. Again, for 60% doping there is sharp rise up to 1.732×10^4 ps/(nm.km) which is at 1.613 µm wavelength. 10% dispersion curve is continuously flattened. For 10% and 30% doping dispersion, curve is almost flattened and remains near zero for total wavelength. After 1.61µm dispersion curve for 30% doping becomes negative. At 1.55 µm wavelength dispersion is -21.7ps/(nm.km), -201 ps/(nm.km), -71.82 ps/(nm.km), -1.11×10^{-16} ps/(nm.km) and -1.033 ps/(nm.km) respectively for 10%, 30%, 40%, 50% and 60% doping concentrations.
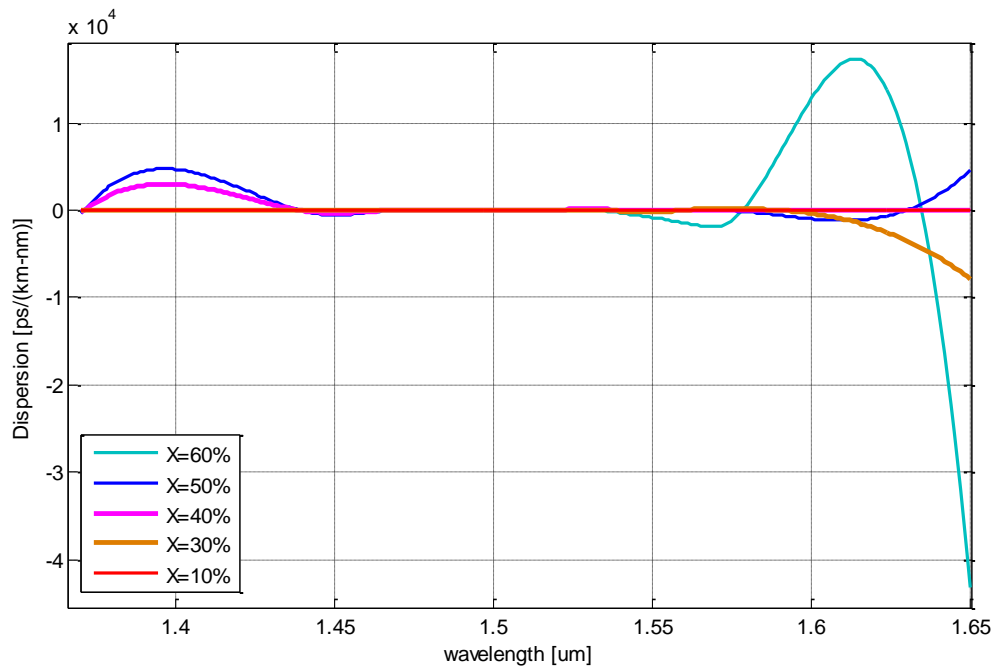
Fig. 4.21: Plot of Dispersion against wavelength for GeO_2-SiO_2 10%, 30%, 40%, 50% and 60% doping concentrations at pitch, $\Lambda = 1.55$ µm

4.3.4   Analysis of Nonlinearity Parameter with GeO₂ Doped Silica Doping

Nonlinearity parameter is also studied for Our Proposed H-PCF for all doping concentrations 10%, 30%, 40%, 50% and 60%. Nonlinearity parameter is calculated using

effective mode area. All data for effective area calculation is taken from COMSOL. Nonlinearity parameter is calculated using equation (2.80).

Fig. 4.22: Plot of Nonlinearity parameter against wavelength for GeO_2-SiO_2 10% doping concentration at pitch, Λ = 1.55 µm

In Fig. 4.22 nonlinearity parameter for 10% doping concentration of GeO_2 doped silica is shown. At 1.47 µm, 1.51 µm, 1.53 µm wavelength nonlinearity parameter are respectively 17.4748 $W^{-1}Km^{-1}$, 16.5038 $W^{-1}Km^{-1}$, 16.0378 $W^{-1}Km^{-1}$. So, nonlinearity parameter decreases with increasing wavelength. At 1.55 µm wavelength nonlinearity parameter is 15.5869 $W^{-1}Km^{-1}$.

In Fig. 4.23 nonlinearity parameter against wavelength is presented for 30% doping concentration of GeO_2 doped silica. For 1.47 µm, 1.51 µm, 1.53 µm wavelength nonlinearity parameter are respectively 20.6492 $W^{-1}Km^{-1}$, 19.4526 $W^{-1}Km^{-1}$, 18.8838 $W^{-1}Km^{-1}$.

Again from Fig. 4.23 at 1.47 µm wavelength nonlinearity parameter for 10% and 30% doping are respectively 17.4748 $W^{-1}Km^{-1}$ and 20.6492 $W^{-1}Km^{-1}$. Comparing the results of 10% and 30% doping it can be said that with increasing doping percentage nonlinearity parameter increases. At 1.55 µm wavelength nonlinearity parameter is 18.3334 $W^{-1}Km^{-1}$.
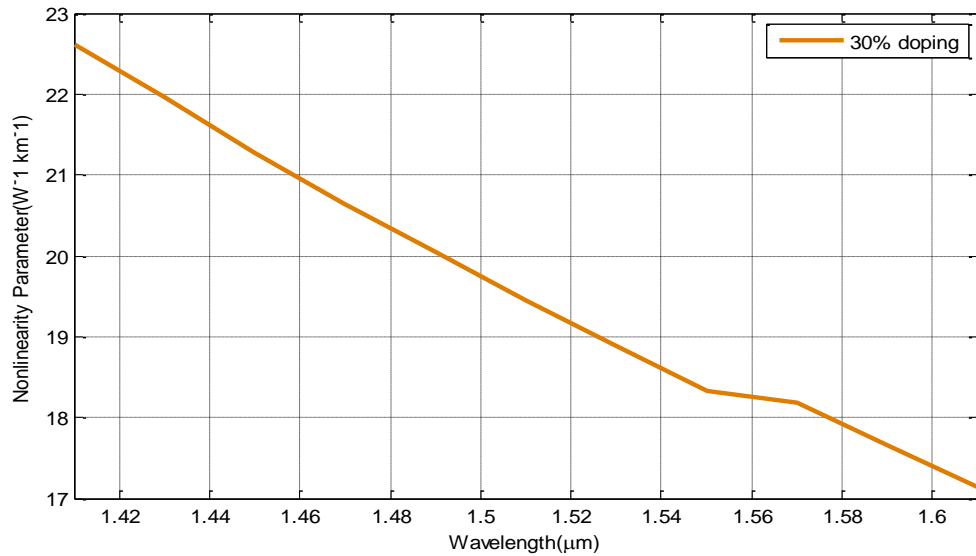
Fig. 4.23: Plot of Nonlinearity parameter against wavelength for GeO_2-SiO_2 30% doping concentration at pitch, $\Lambda = 1.55$ μm

In Fig. 4.24 nonlinearity parameter against wavelength is presented for 40% doping concentration. From curve it is seen that nonlinearity parameter is almost constant from 1.41 to 1.43 μm wavelength. Then the curve starts falling and falls up to 1.61 μm. At 1.47 μm, 1.49 μm, 1.51 μm, 1.53 μm wavelength nonlinearity parameter are respectively 22.1344 $W^{-1}Km^{-1}$, 21.4674 $W^{-1}Km^{-1}$, 20.8243 $W^{-1}Km^{-1}$, and 20.2038 W-1 Km-1. For 10%, 30%, 40% doping nonlinearity parameter are respectively 15.5869 $W^{-1}Km^{-1}$, 18.3334 $W^{-1}Km^{-1}$ and 19.6048 $W^{-1}Km^{-1}$ at 1.55 μm. Again, comparing the results it can be said that with increasing wavelength nonlinearity parameter decreases but with increasing doping it increases.
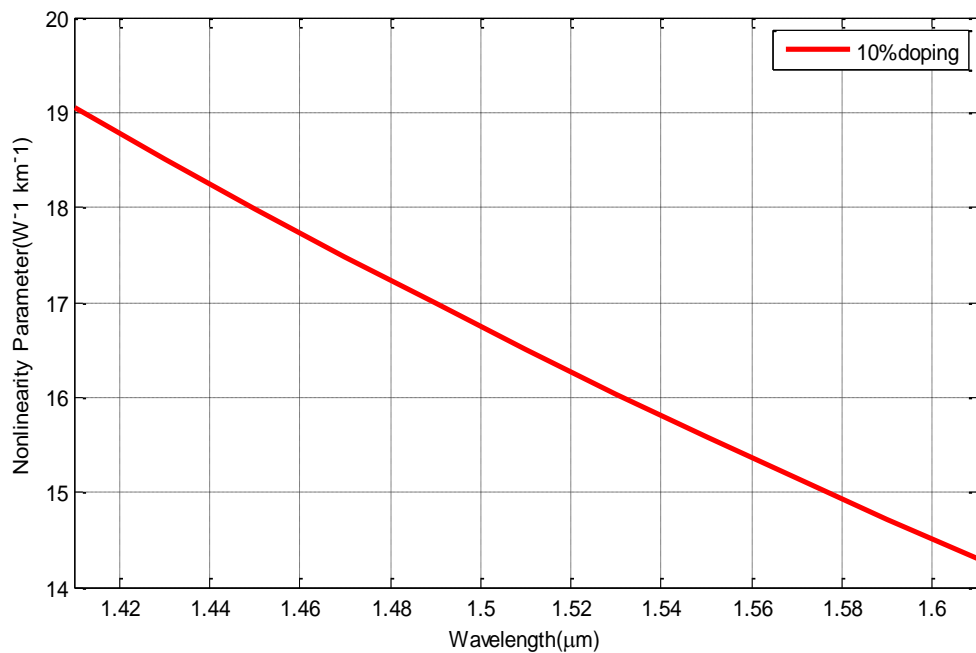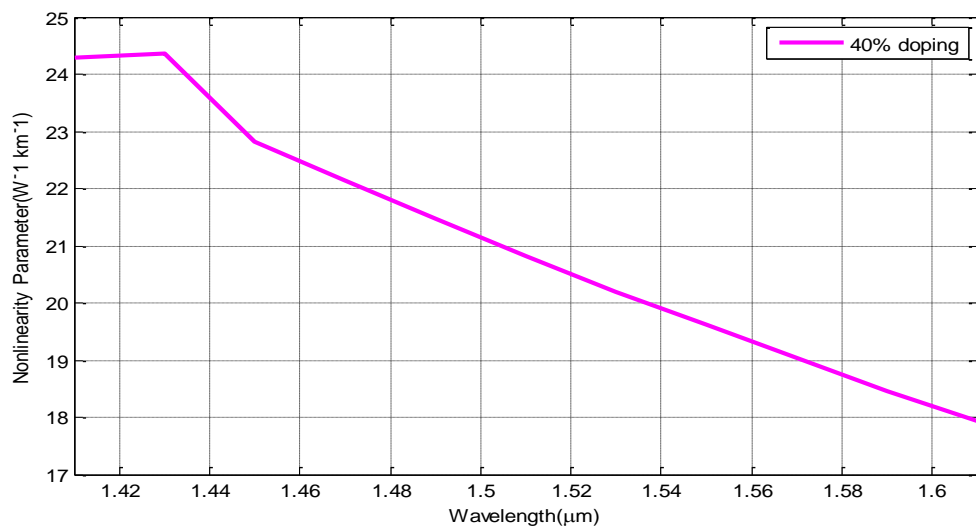

Fig. 4.24: Plot of Nonlinearity parameter against wavelength for GeO_2-SiO_2 40% doping concentration at pitch, $\Lambda = 1.55$ μm
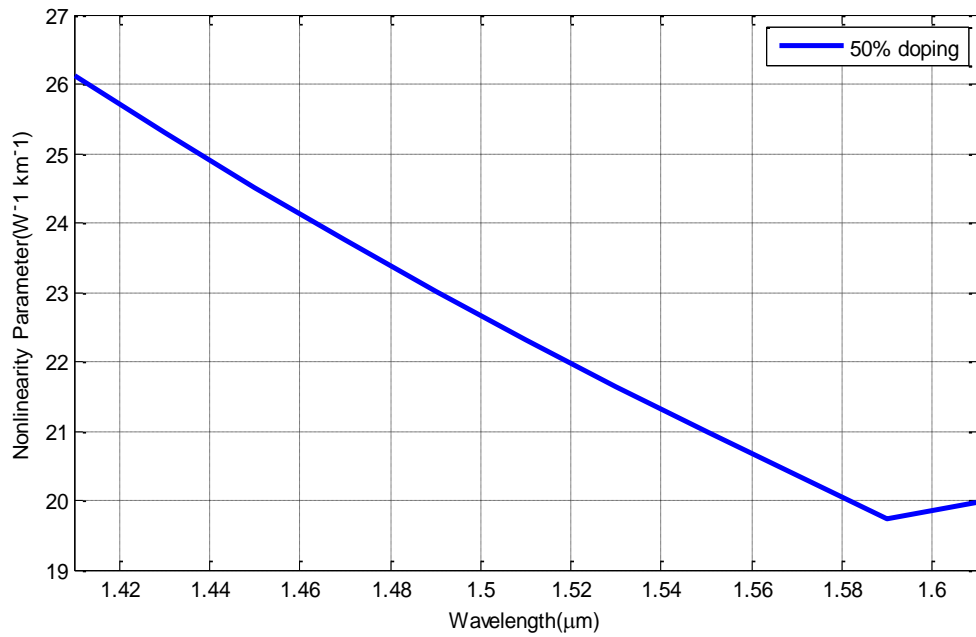
Fig. 4.25: Plot of Nonlinearity parameter against wavelength for 50% doping concentration of GeO_2-SiO_2 at pitch, Λ = 1.55 µm

In Fig. 4.25 nonlinearity parameter against wavelength for 50% doping concentration of GeO_2-SiO_2 doping is presented. From plot it is noticed that the curve is almost linear from 1.41 µm to 1.59 µm wavelength. After 1.59 µm wavelength suddenly the nonlinearity curve starts rising.

At 1.47 µm, 1.49 µm, 1.51 µm, 1.53 µm wavelength nonlinearity parameters are respectively 23.7484 $W^{-1}Km^{-1}$, 23.0170 $W^{-1}Km^{-1}$, 22.3134 $W^{-1}Km^{-1}$ and 21.6360 $W^{-1}Km^{-1}$. At 1.55 µm wavelength nonlinearity parameter for 40% and 50% doping are respectively 19.6048 $W^{-1}Km^{-1}$ and 20.9833 $W^{-1}Km^{-1}$. So, 50% doping shows more nonlinearity than 40% doping.

The Fig. 4.26 shows nonlinearity against wavelength for 60% doping concentration. From figure it is seen that for 60% doping concentration nonlinearity curve is linear. At 1.55 µm wavelength nonlinearity parameter is 22.3650 $W^{-1}Km^{-1}$.

Again, 25.3719 $W^{-1}Km^{-1}$, 24.5745 $W^{-1}Km^{-1}$, 23.8087 $W^{-1}Km^{-1}$, 23.0727 $W^{-1}Km^{-1}$ nonlinearity parameters are found respectively for 1.47 µm, 1.49 µm, 1.51 µm, 1.53 µm wavelength.
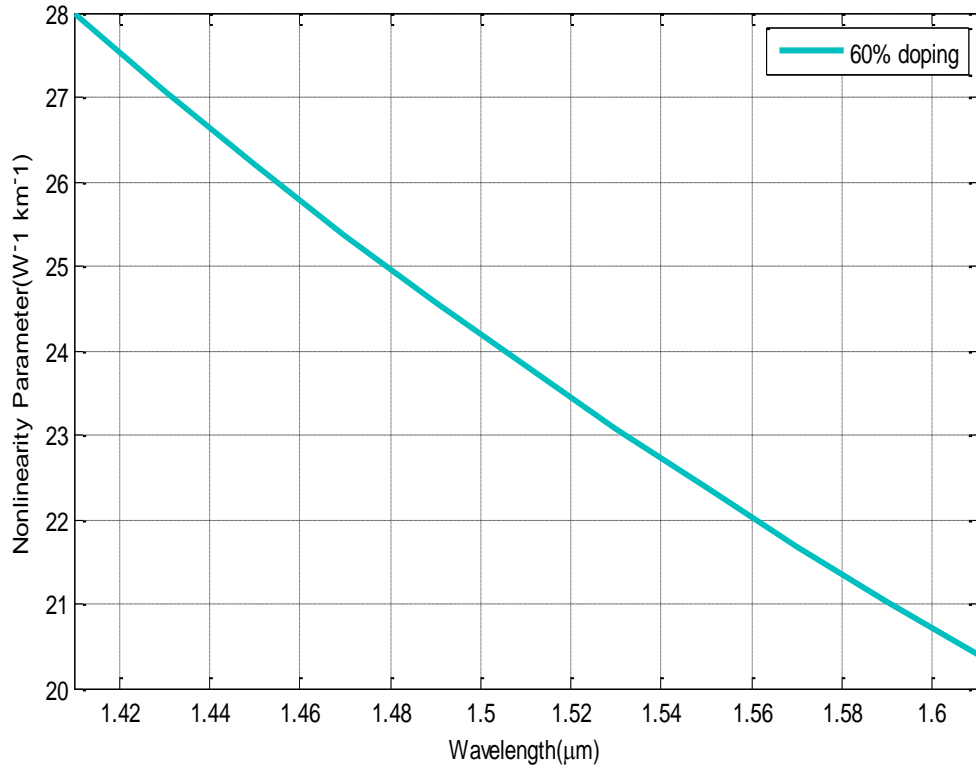
Fig. 4.26: Plot of Nonlinearity parameter against wavelength for 60% doping concentration of GeO_2-SiO_2 doping at pitch, $\Lambda = 1.55$ μm

In Fig. 4.27 nonlinearty parameter against wavelength is presented for all doping concentrations such as 10%, 30%, 40%, 50% and 60% of GeO_2-SiO_2 H-PCF. From Fig. it is noticed that with inceasing wavelength nonlinearity parameter decreases. Minimum value for nonlinearity parameter is found for 10% doping concentration. Maximum value is seen at 60% doping.

Again, in Fig. 4.27 At 1.55 μm wavelength for 10%, 30%, 40%, 50% and 60% doping concentrations, nonlinearity parameter values are respectively 15.5869 $W^{-1}Km^{-1}$, 18.3334 $W^{-1}Km^{-1}$, 19.6048 $W^{-1}Km^{-1}$, 20.9833 $W^{-1}Km^{-1}$, 22.3650 $W^{-1}Km^{-1}$.

Comparing the results, it is found that with increasing doping nonlinearity parameter increases. 10% and 60% curve are totally linear but 30%, 40%, 50% curve is not fully linear. It shows fluctuation in one or two wavelengths.
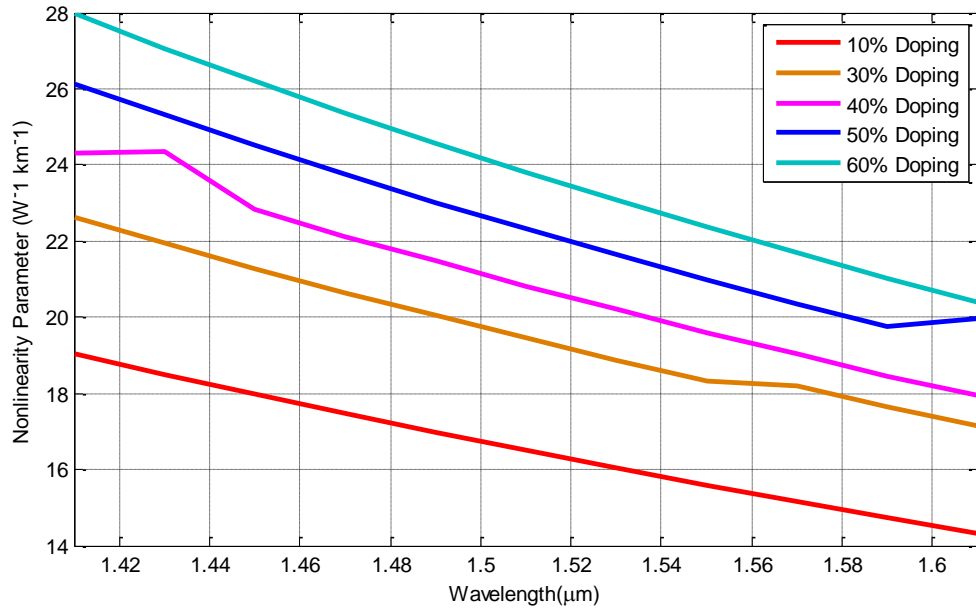
Fig. 4.27: Plot of Nonlinearity parameter against wavelength for GeO_2-SiO_2 10%, 30%, 40%, 50% and 60% doping concentration at pitch, $\Lambda = 1.55$ μm

4.4 Analysis of H-PCF Model with Doping for BaF_2

4.4.1 Analysis of Effective Mode Index for BaF_2-SiO_2 Doping

The effective mode index of BaF_2-doped SiO_2 (BaF_2-SiO_2) is similarly found simulating the proposed model with COMSOL4.3. Equation (2.16) can be efficiently used for the calculation of mode index. Different doping concentrations for BaF_2-SiO_2 model are taken into consideration. In this case 10%, 30%, 40%, 50% and 60% doping concentrations are used to analyze the behavior of the model.

In Fig.4.28 effective mode index(η_{eff}) is plotted as a function of wavelength at pitch, $\Lambda = 1.55$ μm for 10% doping concentration BaF_2-SiO_2. At 1.47 μm, 1.51 μm effective mode index are respectively 1.4015 and 1.3992. The plot is linear and with increasing wavelength effective mode index decreases. At 1.55 μm wavelength effective mode index is 1.396931 for 10% doping concentration of BaF_2-SiO_2. For 0% doping concentration effective mode index is 1.395679. So, effective mode index increases in very small amount after doping with BaF_2. For GeO_2 10% doping effective mode index is 1.400574 at 1.55 μm wavelength. Comparing the results, it can be said that after doping with GeO_2 increase of effective mode index is more than BaF_2 doping.
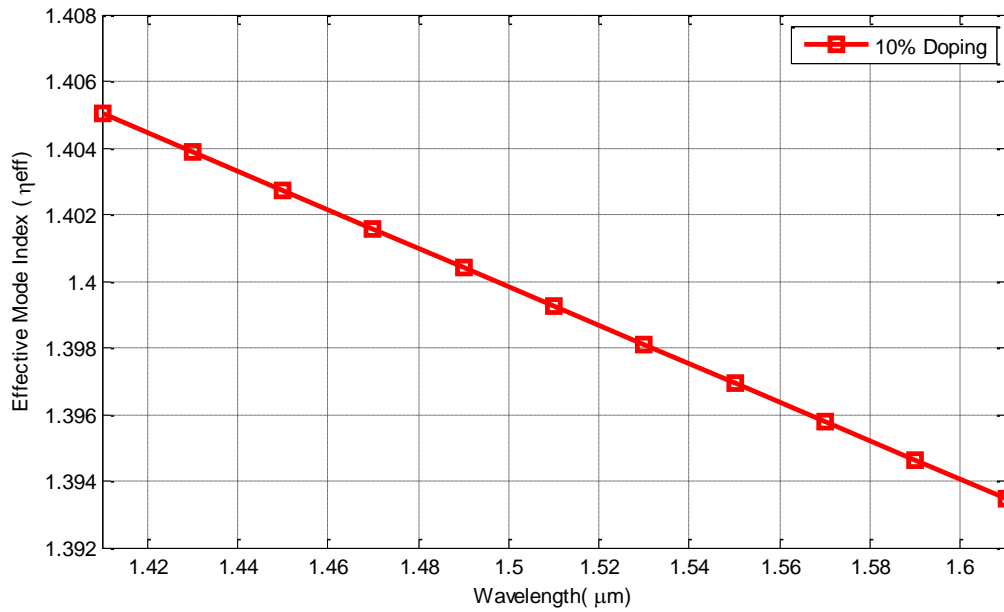
Fig. 4.28: Plot of Effective mode index as a function of wavelength for pitch, $\Lambda = 1.55$ μm, with 10% doping of BaF_2-SiO_2

Fig. 4.29 shows effective mode index against wavelength for 30% doping concentration of BaF_2 doped silica. At 1.47 μm and 1.51 μm wavelength effective mode index are respectively 1.403255 and 1.400948.

Fig. 4.29: Plot of Effective mode index as a function of wavelength for pitch, $\Lambda = 1.55$ μm with 30% doping concentration of BaF_2-SiO_2

At 1.55 μm wavelength effective mode index are 1.395679, 1.398635 and 1.411287 which are respectively for 0% doping, 30% doping of BaF_2 and 30% doping of GeO_2. After doping with BaF_2 effective mode index increases but the increase is not significant as it is for GeO_2 doping.

Again at 1.55 μm wavelength effective mode index is 1.396931 and 1.398635 for respectively 10% and 30% doping of BaF_2. So, with increasing doping of BaF_2 effective mode index decreases.

Fig. 4.30: Plot of Effective mode index as a function of wavelength for pitch, Λ =1.55 μm at 40% doping concentration of BaF_2-SiO_2.

Fig. 4.30 shows effective mode index against wavelength for 40% doping concentration of BaF_2-SiO_2. At 1.55 μm wavelength effective mode index is 1.399318 for 40% doping of BaF_2.

For GeO_2 effective mode index is 1.417073 at 1.55 μm wavelength for 40% doping. Effective mode index for GeO_2 40% doping is greater than BaF_2 40% doping.

Fig 4.31 shows effective mode index against wavelength for 50% doping concentration of BaF_2-SiO_2. Value of effective mode index is 1.399975 at 1.55 μm wavelength. For 50% doping of GeO_2 effective mode index is 1.423125 at 1.55 μm wavelength.
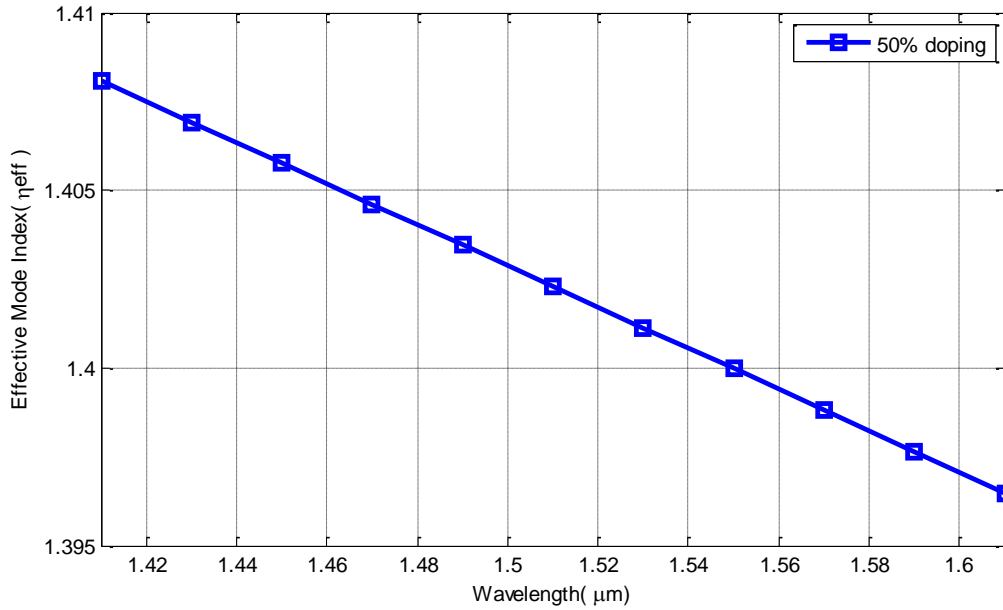
Fig. 4.31: Plot of Effective mode index as a function of wavelength for pitch, Λ =1.55 μm at 50% doping concentration of BaF_2-SiO_2

In Fig. 4.32 effective mode index for 60% doing of BaF_2-SiO_2 at pitch Λ = 1.55 μm is shown. The following Fig. shows the same behavior which is decreasing mode index with increasing of wavelength as it is for 10%, 30%, 40%, 50% doping concentrations. At wavelength 1.55 μm value of effective mode index is 1.429428 and 1.400606 respectively for 60% doping concentration of GeO_2 and BaF_2.

Fig. 4.32: Plot of Effective mode index as a function of wavelength for pitch, Λ =1.55 μm at 60% doping concentration of BaF_2-SiO_2

Fig. 4.33 shows combine plot of effective mode index for all doping percentage of BaF_2 which are taken to considerations. Maximum value of effective mode index is found for 60% doping. Minimum value is found at 10% doping. At 1.55 μm wavelength effective mode index is 1.396931, 1.398635, 1.399318, 1.399975, 1.400606 respectively for 10%, 30%, 40%, 50% and 60% doping of BaF_2. Again, at 1.55 μm wavelength effective mode index is 1.400574, 1.411287, 1.417073, 1.423125, 1.429428 respectively for 10%, 30%, 40%, 50% and 60% doping of GeO_2. So, effective mode index increases with increasing doping concentration. Also, it can be noticed that effective mode index for GeO_2 doping is greater than BaF_2 in all doping concentrations. Values of effective mode index are 1.395679, 1.400606, 1.429428 respectively for 0% doping, 60% doping of BaF_2 and 60% doping of GeO_2. After doping with BaF_2 and GeO_2 the value of effective mode index definitely increases which can be easily realized comparing the results.

Fig. 4.33: Plot of Effective mode index as a function of wavelength for pitch, Λ =1.55 μm at 10%, 30%, 40%, 50% and 60% doping concentrations of BaF_2-SiO_2

4.4.2   Analysis of Effective Mode Area for BaF_2-SiO_2 Doping

Effective mode area for doping percentage 10% 30% 40% 50% and 60% are taken into consideration for BaF_2-SiO_2.
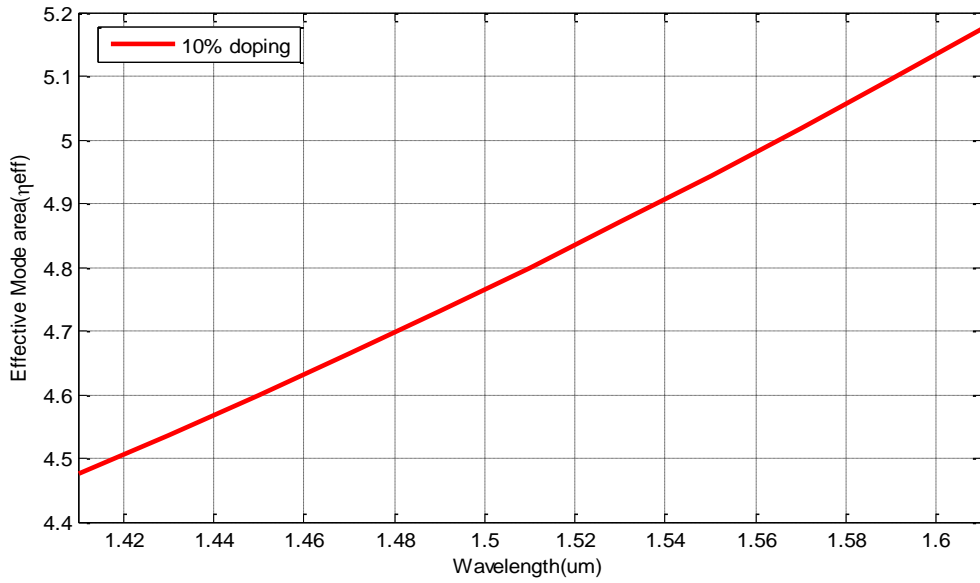
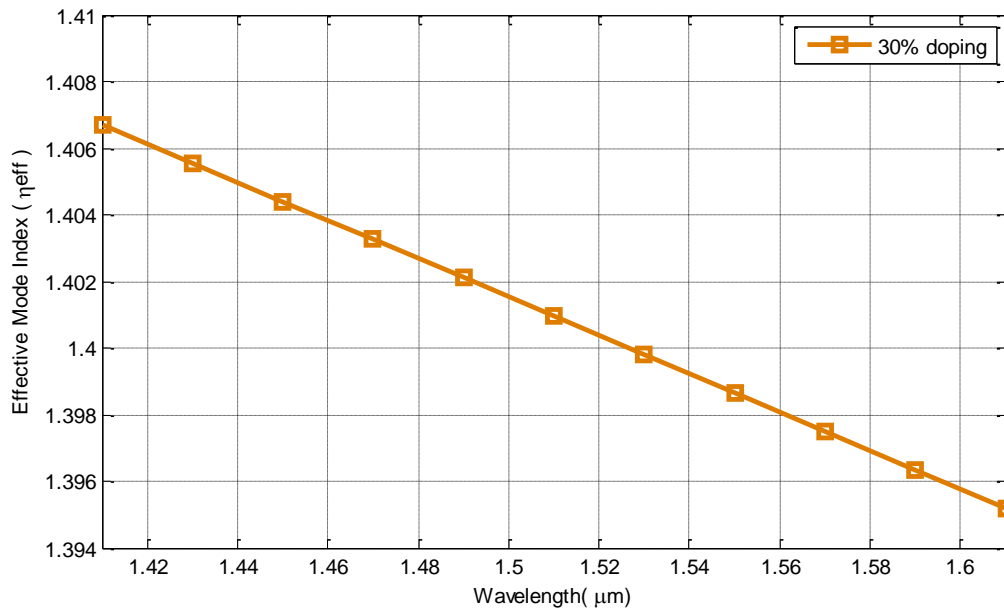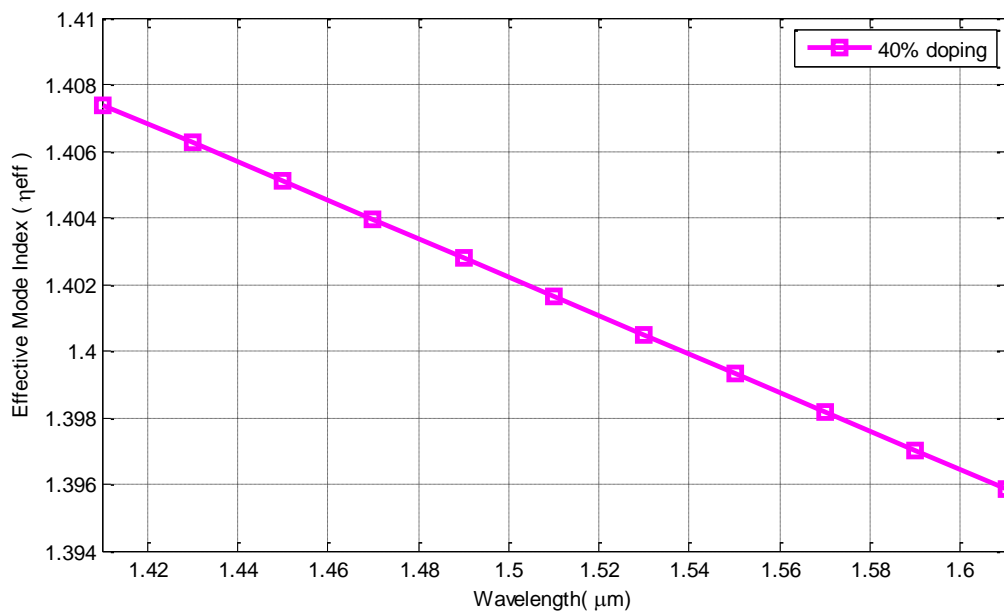**Fig. 4.34:** Plot of Effective mode area as a function of wavelength for pitch, $\Lambda =1.55$ μm at 10% doping concentration of BaF_2-SiO_2.

Fig. 4.34 shows effective mode area against wavelength for 10% doping concentration of BaF_2-SiO_2. Effective mode area is 4.6640 μm^2, 4.7307 μm^2 and 4.7994 μm^2 respectively at 1.47 μm, 1.49 μm and 1.51 μm wavelength for 10% BaF_2 doping. So, with increasing wavelength effective mode area increases. At 1.55 μm wavelength effective mode area is 5.0717μm^2, 4.9429μm^2 respectively for 0% doping and 10% doping of BaF_2. After doping effective mode area decreases. At 1.55 μm wavelength effective mode area is 4.6292 μm^2 for 10% doping of GeO_2. Effective mode area for GeO_2 doping is less than BaF_2 doping.
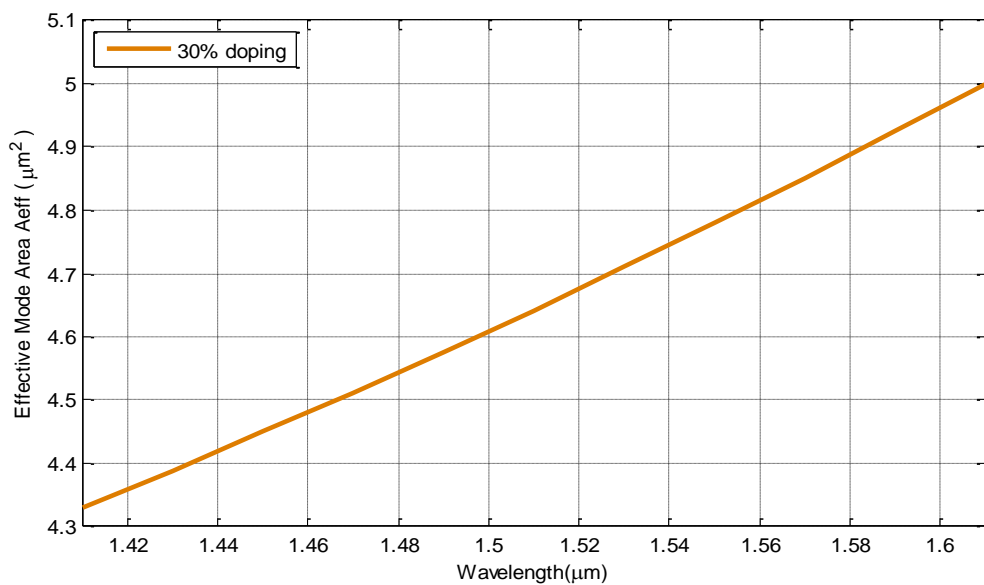
Fig. 4.35: Plot of Effective mode area as a function of wavelength for pitch, $\Lambda =1.55$ μm at 30% doping concentration of BaF_2-SiO_2

Fig. 4.35 shows effective mode area against wavelength for 30% doping concentration of BaF$_2$-SiO$_2$. The plot is almost linear.

Again, from Fig 4.35 it is seen that at 1.55 µm wavelength effective mode area is 4.7795 µm^2 for 30% doping of BaF$_2$. Again for 30% GeO$_2$ doping effective mode area is 3.9357 µm^2. For same doping percentage BaF$_2$ doping has more effective area than GeO$_2$.
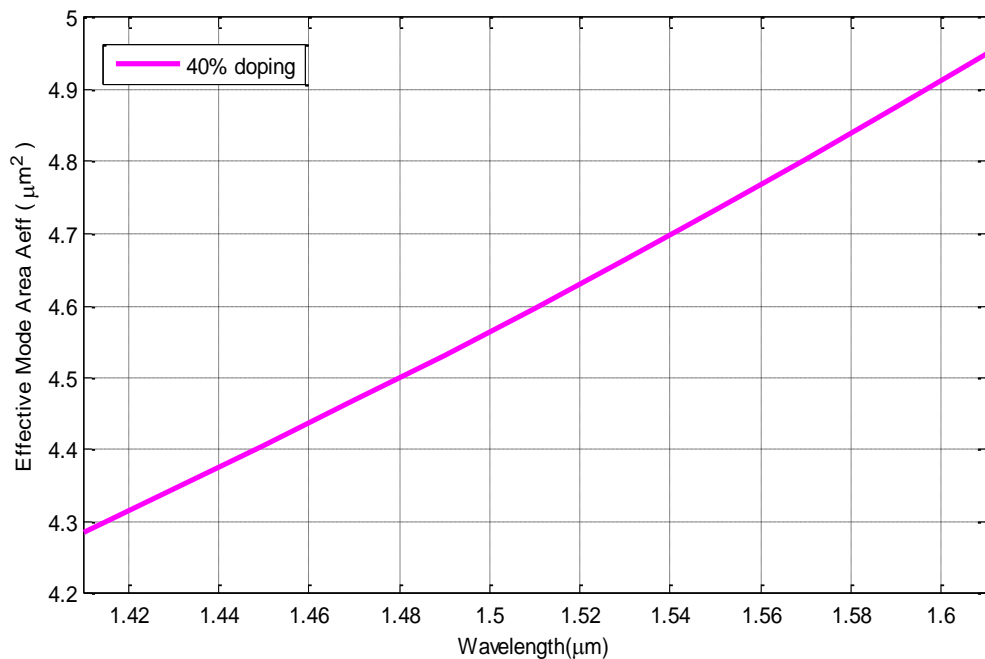
Fig. 4.36: Plot of Effective mode area as a function of wavelength for pitch, Λ =1.55 µm at 40% doping concentration of BaF$_2$-SiO$_2$

In Fig. 4.36 effective mode area for 40% doping concentration of BaF$_2$ is shown. At 1.47 µm, 1.51 µm, 1.53 µm effective mode area are respectively 4.4675 µm^2, 4.5312 µm^2 and 4.5966 µm^2.

Again, from Fig. 4.36 it is seen that at 1.55 µm wavelength effective area is 4.7329 µm^2. For GeO$_2$ 40% doping effective mode area is 3.6598 µm^2 at 1.55 µm wavelength.

Fig. 4.37 shows effective mode area against wavelength for 50% doping concentration of BaF$_2$-SiO$_2$. At 1.55 µm wavelength effective mode area is 4.6779 µm^2 for 50% BaF$_2$ doping. For GeO$_2$ at the same wavelength and same doping percentage effective mode area is 3.4193 µm^2.
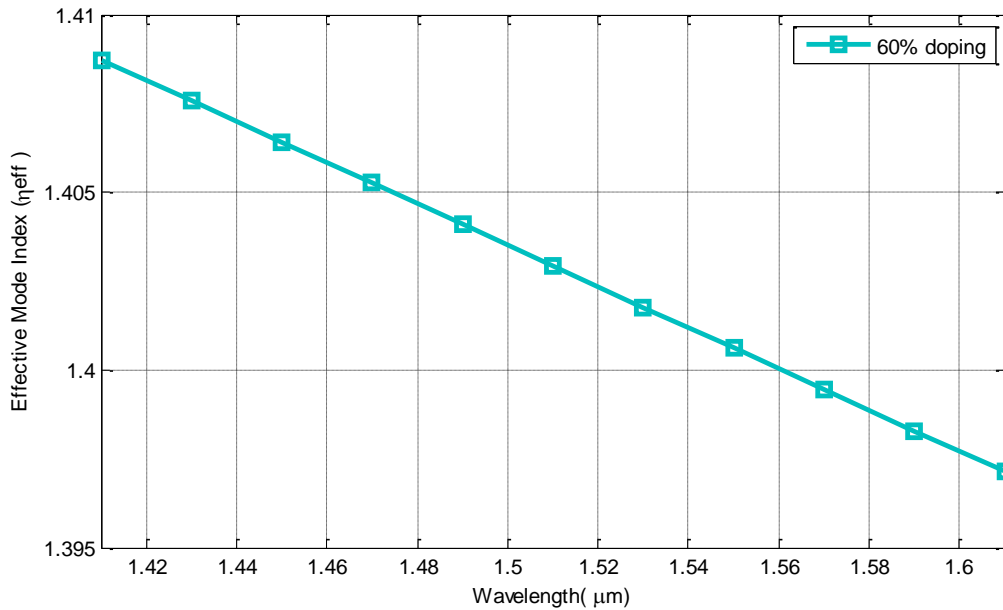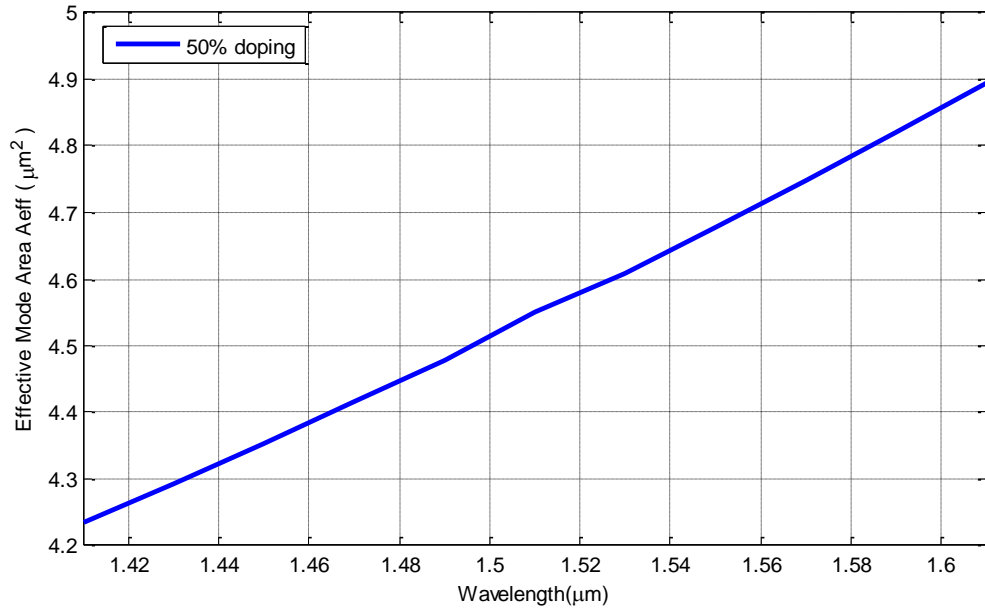
Fig. 4.37: Plot of Effective mode area as a function of wavelength for pitch, Λ =1.55 μm at 50% doping concentration of BaF$_2$-SiO$_2$.
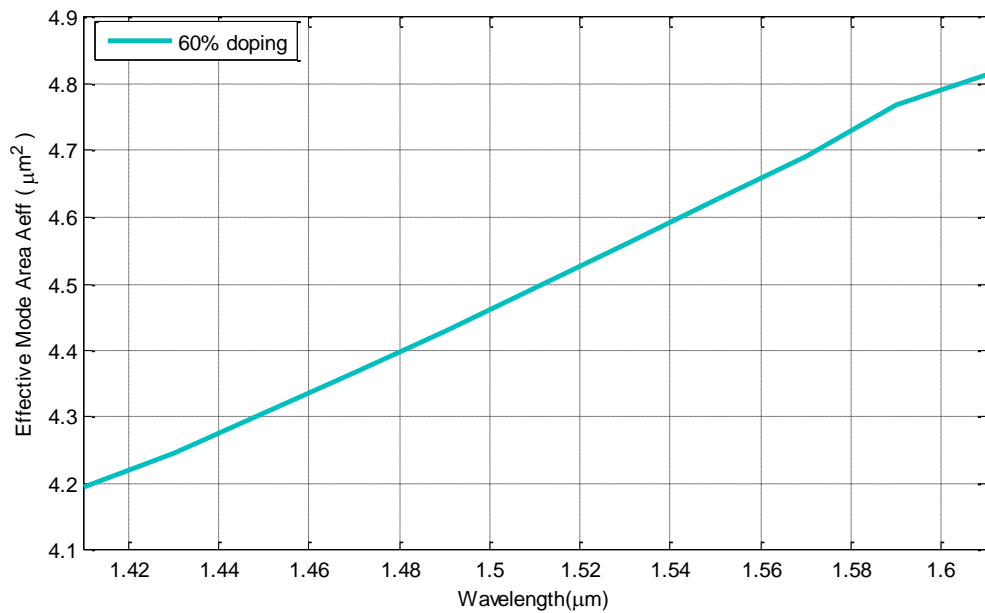
Fig. 4.38: Plot of Effective mode area as a function of wavelength for pitch, Λ =1.55 μm at 60% doping concentration of BaF$_2$-SiO$_2$

Fig 4.38 also shows the same characteristics like others. It shows effective mode area against wavelength for 60% doping concentration of BaF$_2$. At 1.55 μm wavelength effective mode area is 4.6266 μm^2 for 60% doping of BaF$_2$.

Fig. 4.39 shows combine plot of effective mode area for all doping percentage. Value of Effective mode area is 4.94293 μm^2, 4.77952 μm^2, 4.73297 μm^2, 4.67794 μm^2 and 4.62666 μm^2 at 1.55 μm wavelength for respectively 10%, 30%, 40%, 50% and 60% doping concentrations of BaF_2. So, effective mode area decreases with increasing doping concentration. Maximum value of effective area is found for 10% doping and minimum value is found for 60% doping. All doping percentage curve shows same characteristic that is with increasing wavelength effective mode area increases. Again, for GeO_2 effective mode area at 1.55 μm wavelength is 4.6292 μm^2, 3.9357 μm^2, 3.6598 μm^2, 3.4193 μm^2, 3.2081 μm^2 respectively for 10%, 30%, 40%, 50% and 60% doping concentrations. So, BaF_2 doping provides more effective area than GeO_2 doping.
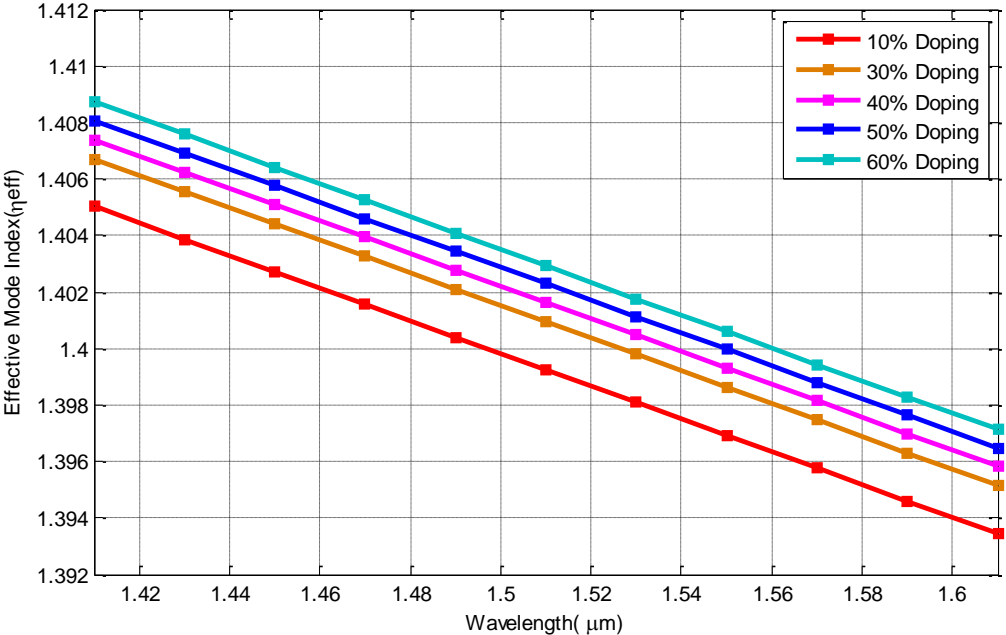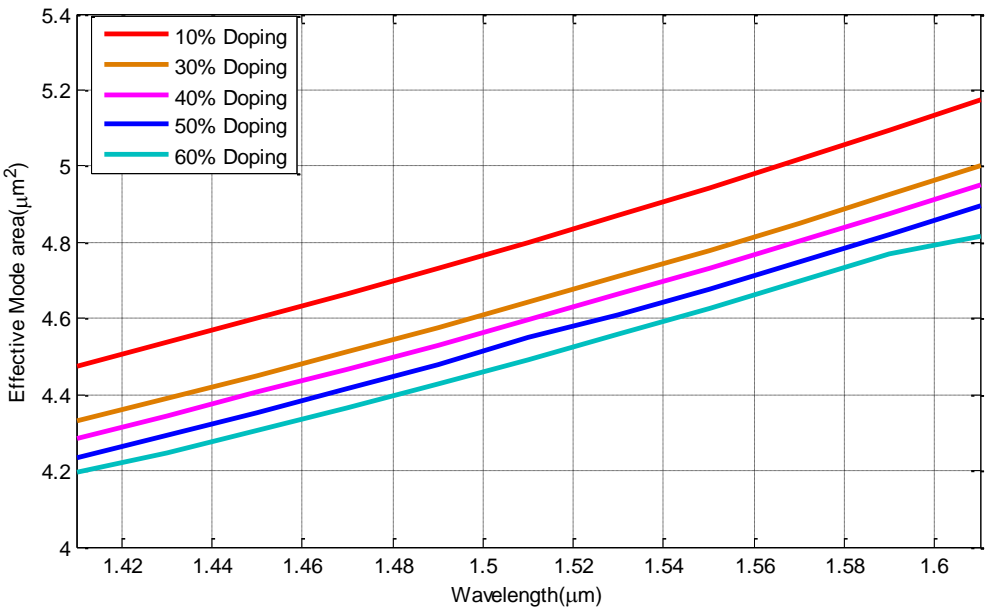

Fig. 4.39: Plot of Effective mode area as a function of wavelength for pitch, Λ =1.55 μm, at 10%, 30%, 40%, 50%, 60% doping concentrations of BaF_2-doped SiO_2.

4.4.3 Analysis of Dispersion for BaF₂-SiO₂ Doping

Dispersion is an important parameter for studying losses of PCF. Dispersion is also studied for BaF_2 doped SiO_2 doping. 10%, 30%, 40%, 50% and 60% doping concentrations are taken into consideration in calculating dispersion.

Fig. 4.40: Plot of Dispersion against wavelength for BaF_2-SiO_2 10% doping concentration at pitch, $\Lambda = 1.55$ μm.

Fig. 4.40 shows dispersion of Barium fluoride doped silica for 10% doping concentration. From curve it is seen that with increasing wavelength dispersion decreases. The dispersion curve starts at 1.37 μm wavelength. At 1.37 μm wavelength dispersion is 6.139×10^4 ps/(nm.km). Then the dispersion curve falls down. In the curve, fluctuation of dispersion is seen from 1.434 μm to 1.505 μm wavelength. Highest negative dispersion is seen at 1.45 μm wavelength which is -1672 ps/(nm.km). From 1.505 to 1.62 μm wavelength dispersion curve is almost flattened. In this range dispersion varies from -88.55 ps/(nm.km) to 5.672 ps/(nm.km). At 1.55 μm wavelength dispersion is 1.033 ps/(nm.km). For GeO_2 10% doping at 1.55 μm wavelength dispersion is -21.7 ps/(nm.km). So, GeO_2 doping gives more negative dispersion than BaF_2 doping at 1.55 μm wavelength.

Fig. 4.41 shows dispersion against wavelength for 30% doping concentration of BaF_2 doped SiO_2. In the curve small flattened dispersion range from 1.41 μm to 1.45μm and in this range dispersion varies from 0.968 ps/(nm.km) to 0.9667 ps/(nm.km). From curve it is seen that dispersion fluctuates at several wavelengths starting from 1.453 μm to 1.531 μm. Again, a flattened range is seen from 1.531 μm wavelength to 1.619 μm wavelength. In this range dispersion varies from 0.51 ps/(nm.km) to 0.5397 ps/(nm.km). It's maximum positive dispersion is 1.47 ps/(nm-km) at 1.47 μm wavelength. Minimum dispersion is 0.4967 ps/(nm-km) which is at 1.49 μm wavelength.

Also for 1.453 μm and 1.531 μm wavelength dispersion are respectively 1.0 ps/(nm-km) and 0.51 ps/(nm-km). At 1.55 μm wavelength dispersion is 0.5167 ps/(nm.km) for BaF_2 30% doping. For GeO_2 30% doping dispersion is -201 ps/(nm.km) at 1.55μm wavelength. Again, GeO_2 doping gives more negative dispersion than BaF_2 doping which is also seen for 10% doping.
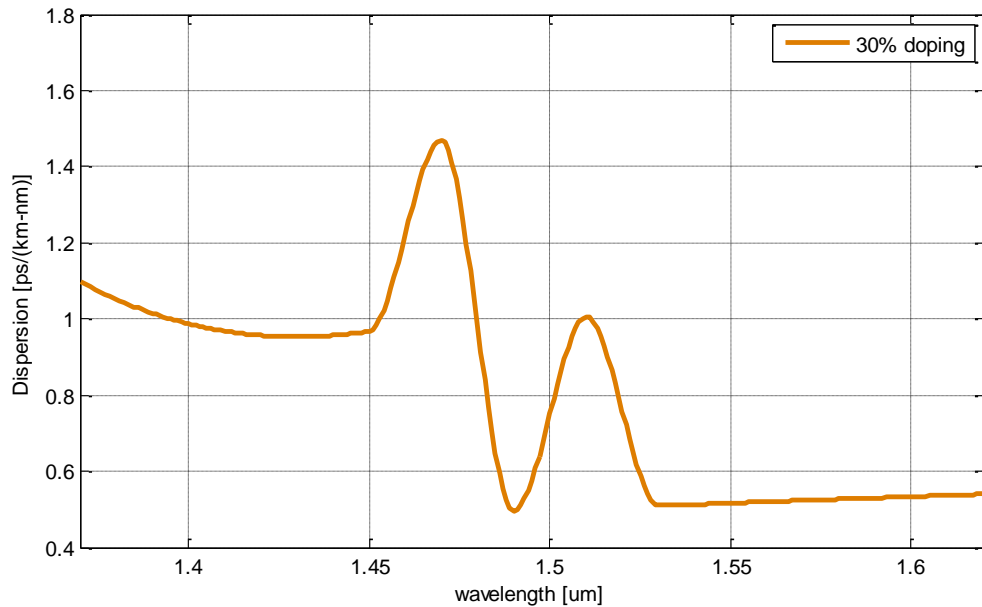
Fig. 4.41: Plot of Dispersion against wavelength for BaF_2-SiO_2 30% doping concentration at pitch, $\Lambda = 1.55$ μm

Fig. 4.42 shows dispersion against wavelength curve for 40% doping of BaF_2-SiO_2. Dispersion fluctuates from 1.45 μm wavelength to 1.573 μm wavelength then it decreases and becomes negative. It has flattened range from 1.4 to 1.449 μm and from 1.528 μm to 1.551 μm wavelength. As we can see the range is very small. It also has maximum positive dispersion 1.47 ps/(nm-km) at 1.47 μm wavelength. At 1.612 μm wavelength it shows minimum dispersion which is -2.316 ps/(nm-km).

For 1.4 μm, 1.449μm, 1.528 μm and 1.551μm wavelength dispersion are respectively 0.9872 ps/(nm-km), 0.9652 ps/(nm-km), 0.5239 ps/(nm-km) and 0.5211ps/(nm-km). After 1.584 μm wavelength dispersion curve becomes negative. At this wavelength dispersion is 0.4958 ps/(nm.km).

At 1.55 μm wavelength dispersion is 0.5167 ps/(nm.km). For GeO_2 40% doping dispersion at 1.55μm wavelength is -71.82 ps/(nm.km).

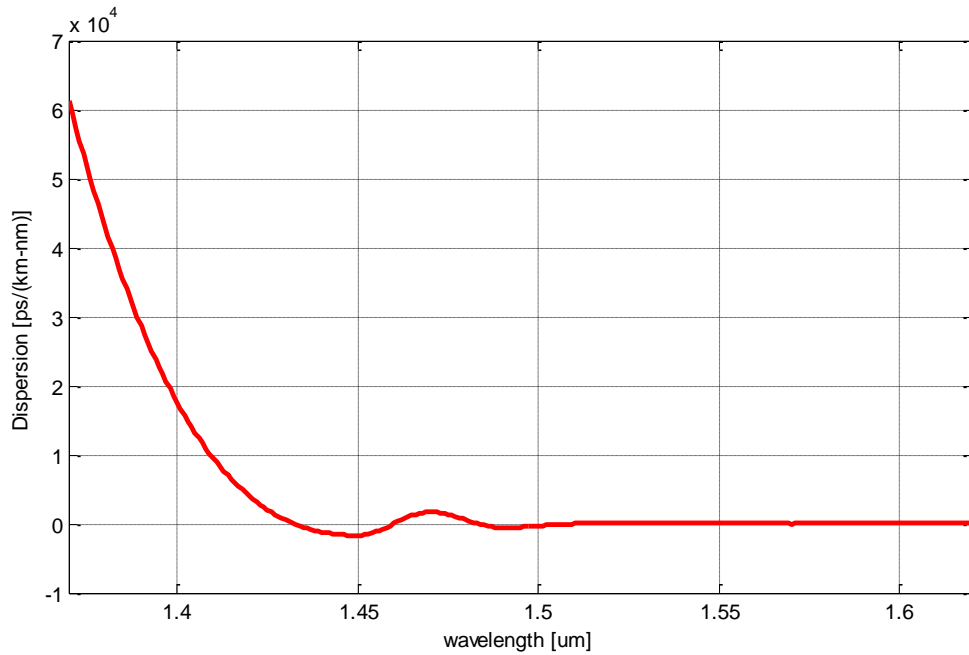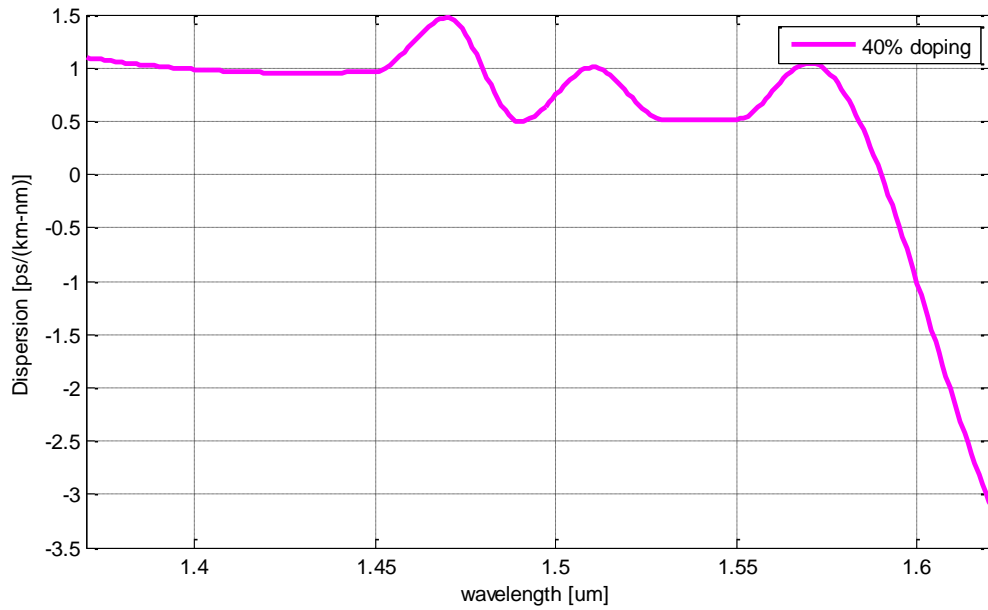**Fig. 4.42:** Plot of Dispersion against wavelength for BaF$_2$-SiO$_2$ 40% doping concentration at pitch, $\Lambda = 1.55$ μm.

Fig. 4.43 shows dispersion against wavelength for BaF$_2$ doped SiO$_2$ at 50% doping concentration. It is noticed that dispersion increases with wavelength and become stable at 1.55 μm wavelength. It has flattened range from 1.467 μm to 1.492 μm wavelength and from 1.549 μm and 1.612 μm wavelength.
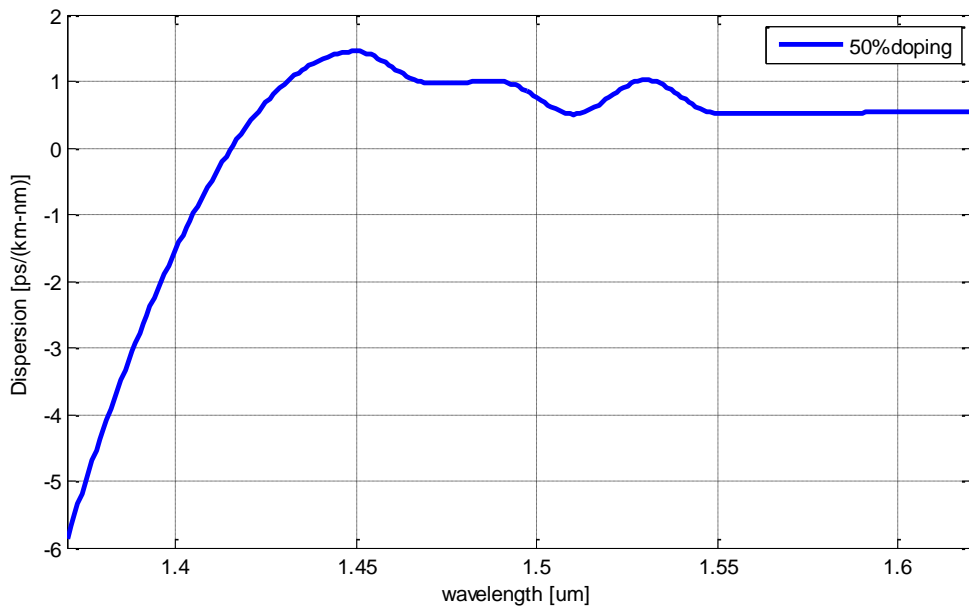
Fig. 4.43: Plot of Dispersion against wavelength for BaF$_2$-SiO$_2$ 50% doping concentration at pitch, $\Lambda = 1.55$ μm.

In Fig. 4.43 maximum positive dispersion is at 1.45 μm wavelength which is 1.45 ps/(nm-km). Also, maximum negative dispersion is -5.857 ps/(nm-km) which is at 1.37 μm

wavelength. Again at 1.467 μm, 1.492 μm, 1.549 μm, 1.612 μm dispersion are respectively 0.9932 ps/(nm-km), 0.9796 ps/(nm-km), 0.5203 ps/(nm-km), 0.5373 ps/(nm-km). At 1.55 μm wavelength dispersion is -1.11×10^{-16} ps/(nm.km) and 0.5167 ps/(nm.km) for respectively 50% doping of GeO_2 and 50% doping of BaF_2.
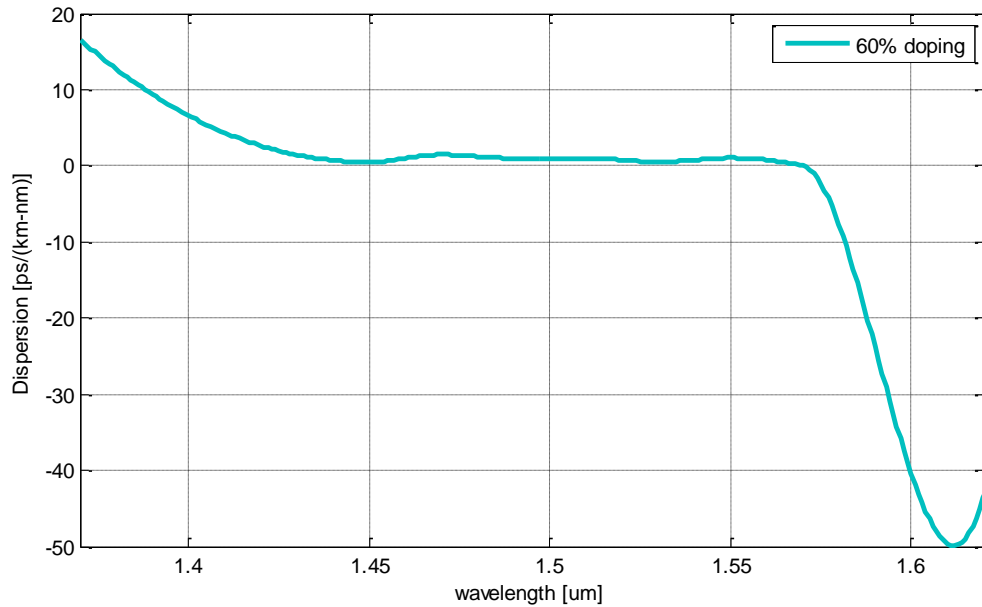
Fig. 4.44: Plot of Dispersion against wavelength for 60% doping concentration of BaF_2-SiO_2 doping at pitch, $\Lambda = 1.55$ μm

Fig. 4.44 shows dispersion against wavelength curve for 60% doping concentration of BaF_2-SiO_2. 60% dispersion curve starts at 1.37 μm wavelength. At this wavelength dispersion is 16.59 ps/(nm.km). Then the curve falls down up to 1.45 μm wavelength It has flattened range from 1.45 μm to 1.569 μm wavelength.

Also in Fig. 4.44, at 1.569 μm wavelength dispersion is 0.09688 ps/(nm-km) which is almost zero. Minimum dispersion is -49.86 ps/(nm-km) which is at 1.612 μm wavelength. At 1.45 μm and 1.569 μm wavelength dispersion is respectively 0.4833 ps/(nm-km), 0.06988 ps/(nm-km). At 1.55μm wavelength for BaF_2 60% doping dispersion is 1.033 ps/(nm.km). For GeO_2 60% doping at 1.55 μm wavelength dispersion is -1.033 ps/(nm.km).

Fig. 4.45 shows dispersion against wavelength curve for all doping concentrations of BaF_2-SiO_2. For 30%, 40%, 50%, 60% doping value of dispersion is very close to each other. This is the reason the four curves are very close to each other and the curves almost overlap. It has maximum dispersion of 6.139×10^4 ps/(nm-km) at 10% doping which is at

1.37 μm wavelength. Dispersion of -1672 ps/(nm-km) is seen for 10% doping at 1.45 μm wavelength.
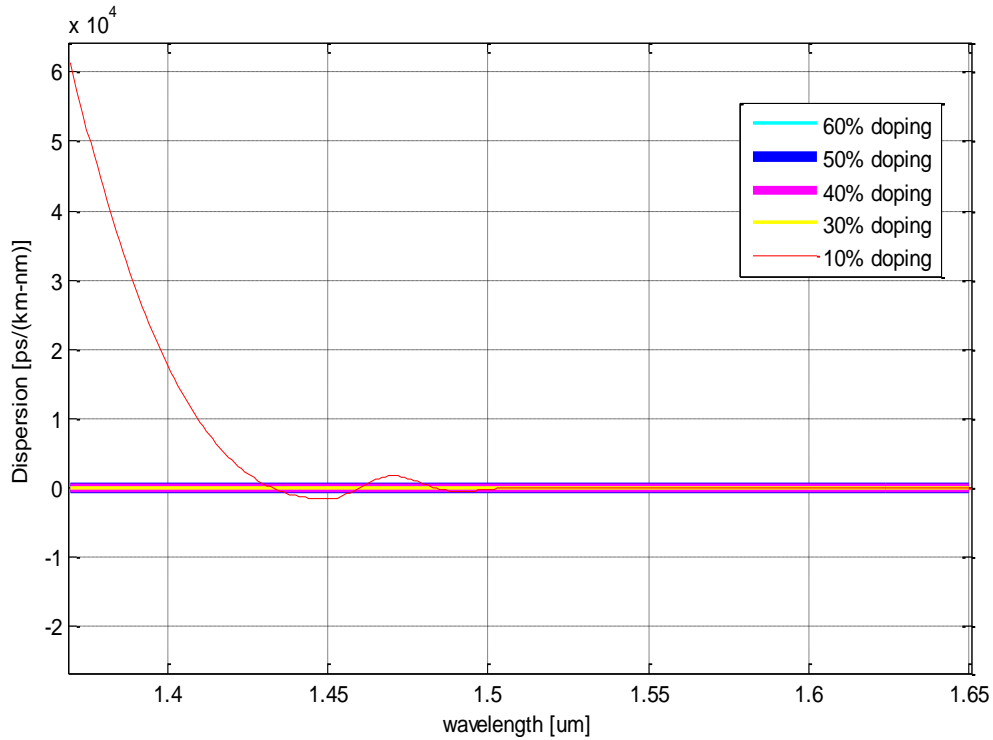
Fig. 4.45: Plot of Dispersion against wavelength for 10%, 30%, 40%, 50% and 60% doping concentrations of BaF_2-SiO_2 at pitch, $\Lambda = 1.55$ μm.

4.4.4 Analysis of Nonlinearity Parameter with BaF_2 Doped Silica Doping

Nonlinearity is another important parameter for measuring losses of photonic crystal fiber. 10%, 30%, 40%, 50% and 60% doping percentage have taken to consideration for our proposed H-PCF. Nonlinearity parameter is calculated using equation (2.8). Using effective mode area non-linear coefficient is calculated. All data for effective area calculation is taken from COMSOL.

Fig. 4.46 shows nonlinearity parameter against wavelength curve for 10% doping of BaF_2-SiO_2. At 1.49 μm, 1.51 μm and 1.53 μm nonlinearity parameter are respectively 15.9556 $W^{-1}Km^{-1}$, 15.5189 $W^{-1}Km^{-1}$ and 15.0936 $W^{-1}Km^{-1}$. So, Nonlinearity parameter decreases with wavelength. At 1.55 μm wavelength nonlinearity parameter is 14.6797 $W^{-1}Km^{-1}$ for 10% doping of BaF_2. For 10% doping of GeO_2 nonlinearity parameter is 15.5869 $W^{-1} Km^{-1}$ at 1.55 μm.

Fig. 4.46: Plot of Nonlinearity parameter as a function of wavelength for pitch, $\Lambda = 1.55$ μm at 10% doping concentration of BaF_2-SiO_2

Fig. 4.47: Plot of Nonlinearity parameter as a function of wavelength for pitch, $\Lambda = 1.55$ μm at 30% doping concentration of BaF_2-SiO_2

Fig. 4.47 shows nonlinearity parameter against wavelength curve for 30% doping concentration of BaF_2-SiO_2. At 1.47 μm, 1.49 μm and 1.51 μm nonlinearity parameter are respectively 16.9571 $W^{-1}Km^{-1}$, 16.4950 $W^{-1}Km^{-1}$ and 16.0452 $W^{-1}Km^{-1}$. From the result it is seen that nonlinearity parameter decreases with increasing wavelength.

At 1.55 µm nonlinearity parameter is 14.6797 $W^{-1}Km^{-1}$ and 15.1860 $W^{-1}Km^{-1}$ respectively for 10% and 30% doping of BaF_2. So, nonlinearity parameter increases with increasing doping percentage.

For 30% doping percentage of GeO_2 nonlinearity parameter is 18.333 $W^{-1}Km^{-1}$ at 1.55 µm wavelength. Comparing the result, it is seen that GeO_2 30% doping shows more nonlinearity than 30% doping of BaF_2.
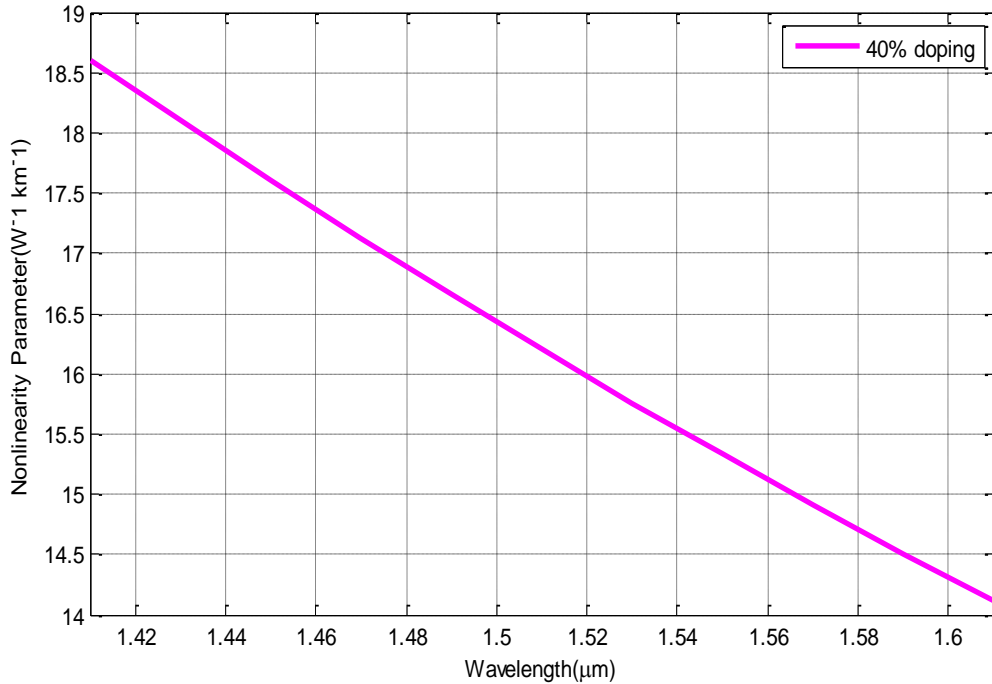
Fig. 4.48: Plot of Nonlinearity parameter as a function of wavelength for pitch, Λ =1.55 µm at 40% doping concentration of BaF_2-SiO_2

In Fig. 4.48 shows the Nonlinearity parameter is shown for 40% doping concentration of BaF_2. At 1.47 µm, 1.49 µm and 1.51 µm wavelength nonlinearity parameter are respectively 17.1256 $W^{-1}Km^{-1}$, 16.6583 $W^{-1}Km^{-1}$ and 16.2037 $W^{-1}Km^{-1}$.

Also in Fig. 4.48, at 1.55 µm wavelength nonlinearity parameter is 15.3309 $W^{-1}Km^{-1}$ and 19.6048 $W^{-1}Km^{-1}$ respectively for 40% doping of BaF_2 and GeO_2. Again, GeO_2 shows more nonlinearity than BaF_2.
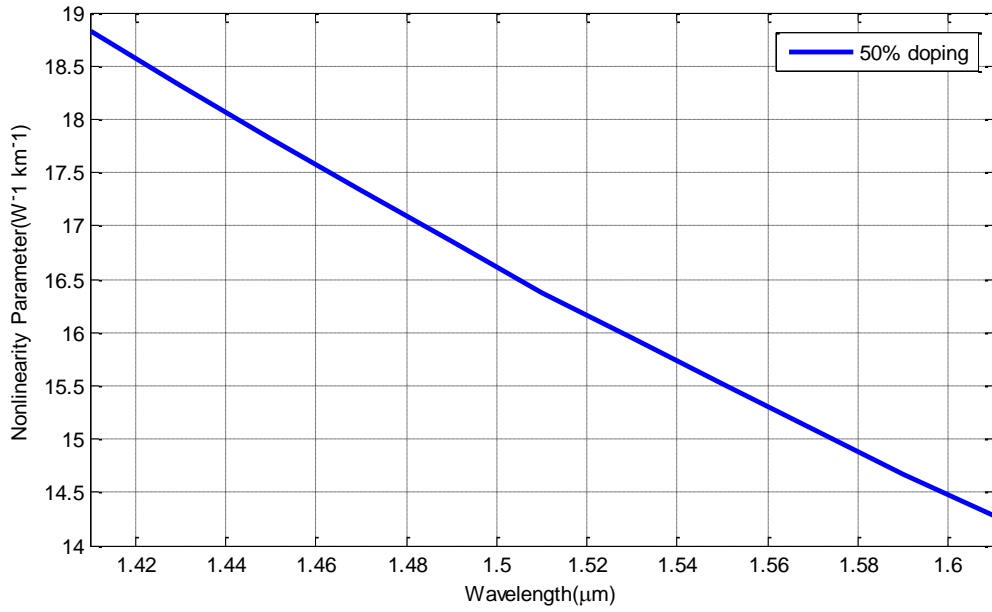
Fig. 4.49: Plot of Nonlinearity parameter against wavelength for pitch, $\Lambda = 1.55$ μm at 50% doping concentration of BaF_2-SiO_2

Fig 4.49 shows nonlinearity parameter against wavelength for 50% doping of BaF_2. At 1.55 μm wavelength nonlinearity parameter are respectively 15.5125 $W^{-1}Km^{-1}$ and 20.9833 $W^{-1}Km^{-1}$ respectively for 50% doping of BaF_2 and GeO_2.
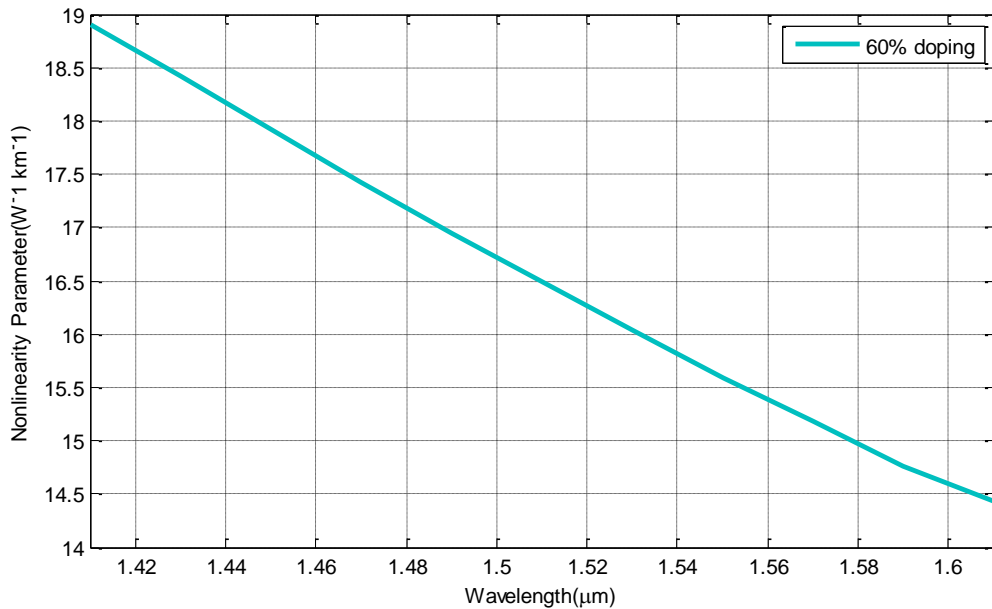
Fig. 4.50: Plot of Nonlinearity parameter against wavelength for pitch, $\Lambda = 1.55$ μm at 60% doping concentration of BaF_2-SiO_2

For 60% doping concentration the value of nonlinearity parameter is 22.3650 $W^{-1}Km^{-1}$ and 15.5955 $W^{-1}Km^{-1}$ respectively for GeO_2 and BaF_2 60% doping at 1.55 μm wavelength

which is shown in Fig. 4.50. So, more nonlinearity is seen for GeO_2 60% doping than BaF_2 60% doping.
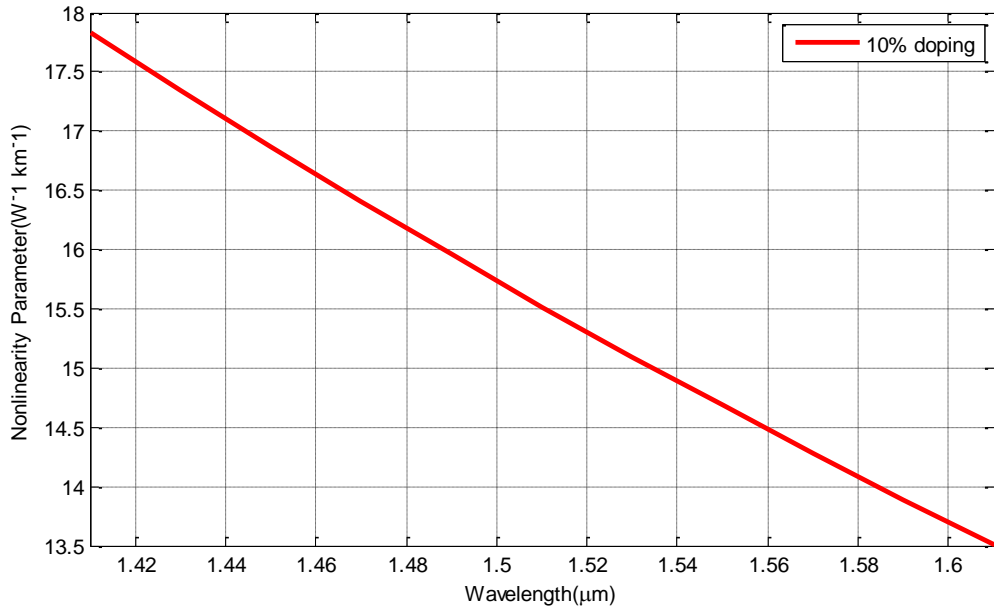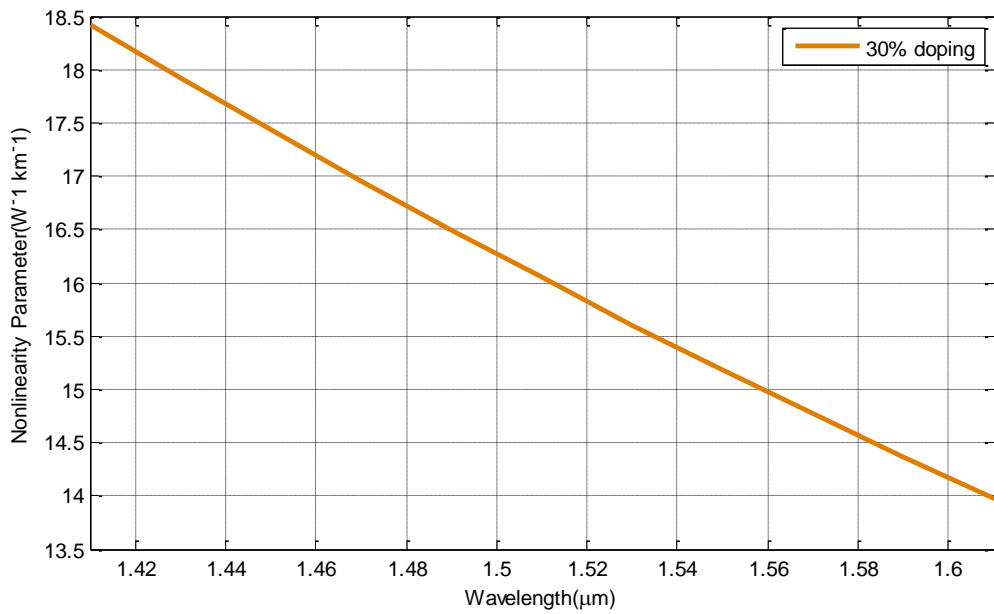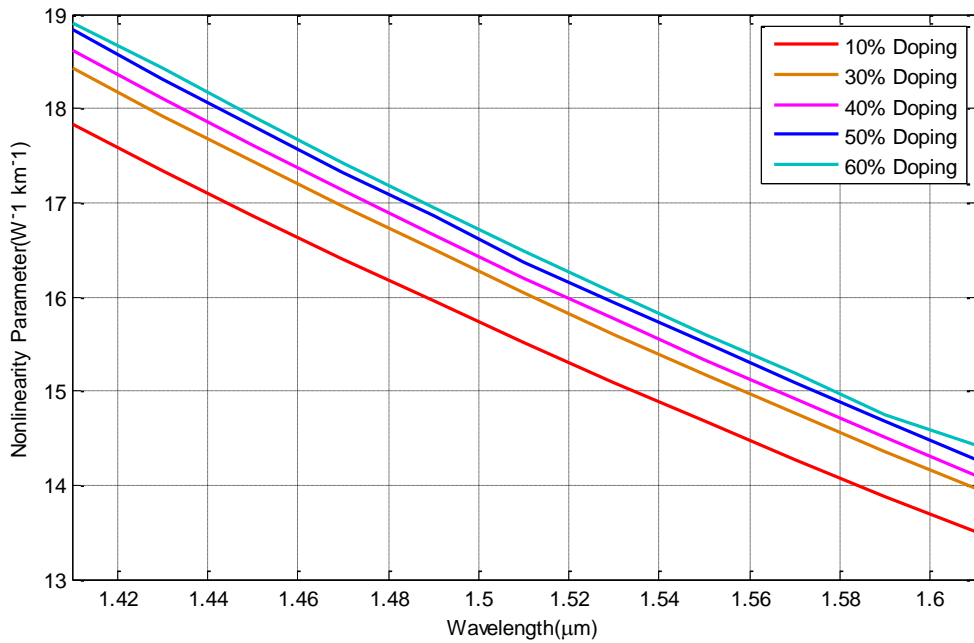

Fig. 4.51: Plot of Nonlinearity parameter against wavelength for 10%, 30%, 40%, 50% and 60% doping concentrations of BaF_2-SiO_2 doping at pitch, $\Lambda = 1.55$ µm

Fig. 4.51 shows combine plot of nonlinearity parameter for all doping percentage we have taken into consideration. Nonlinearity parameter is 14.679, 15.186, 15.330, 15.366, 15.595 $W^{-1}Km^{-1}$ at 1.55 µm wavelength for doping percentage 10%, 30%, 40%, 50% and 60% respectively. With increasing doping percentage nonlinearity parameter increases. Minimum nonlinearity is seen at 10% doping whereas maximum nonlinearity is found at 60% doping. At 1.55 µm wavelength for GeO_2 10%, 30%, 40%, 50% and 60% doping nonlinearity parameter are respectively 15.58699 $W^{-1}Km^{-1}$, 18.3334 $W^{-1}Km^{-1}$, 19.6048 $W^{-1}Km^{-1}$, 20.9833 $W^{-1}Km^{-1}$ and 22.3650 $W^{-1}Km^{-1}$. Comparing the results, it can be said that for all doping concentrations GeO_2 doping shows more nonlinearity than BaF_2 doping.

4.5 Comparison Between Without GeO_2-SiO_2 and BaF_2-SiO_2 Doping

The proposed H-PCF is separately doped with GeO_2 and BaF_2. The comparison of two doping materials and its effect on H-PCF's different parameters such as dispersion, nonlinearity parameter, effective mode area, effective mode index is discussed briefly.

From the previous discussion it is found that dispersion is not flattened at the time of 0% doping. When the proposed model is doped dispersion is flattened in various wavelengths.

That's why doped H-PCF is proposed. It is also noticed that GeO_2-SiO_2 doping gives almost flattened dispersion in a range of wavelength starting from 1.467 μm to 1.533 μm and high negative dispersion of -1017 ps/(nm.km) at 1.61 μm wavelength for 30% doping concentration. At 1.55μm wavelength dispersion is -21.7ps/(nm.km), -201 ps/(nm.km), -71.82 ps/(nm.km), -1.11×10^{-16} ps/(nm.km) and -1.033 ps/(nm.km) respectively for 10%, 30%, 40%, 50% and 60% doping concentration of GeO_2. After comparing 10%, 30%, 40%, 50%, 60% doping concentrations of GeO_2-SiO_2, it is observed that 30% doping concentration gives better result.

Again, the proposed design is doped with Barium fluoride which is a new approach. At 1.55 μm wavelength for BaF_2 10%, 30%, 40%, 50% and 60% dispersion are found respectively 1.033 ps/(nm.km), 0.5167 ps/(nm.km), 0.5167 ps/(nm.km), 0.5167 ps/(nm.km) and 1.033 ps/(nm.km). Though dispersion does not decrease in a large amount with increasing doping percentage but for 10% doping of BaF_2 high negative dispersion of -1672 ps/(nm.km) is seen at 1.45 μm wavelength. That's why 10% doping concentration of BaF_2 is considered more suitable in all doping concentrations (e.g. 10%, 30%, 40%, 50%, 60%) of BaF_2-SiO_2.

4.5.1 Comparison of Effective Mode Index Between Without Doping, GeO_2-SiO_2 Doping and BaF_2-SiO_2 Doping

Effective mode index for without doping, 30% GeO_2-SiO_2 and 10% BaF_2-SiO_2 are taken into consideration as these percentages gives better result.

From Fig. 4.52 it is observed that effective mode index of GeO_2-SiO_2 doping is greater than BaF_2-SiO_2 doping. Both the curves show same nature. Both curves start decreasing with increasing of wavelength. GeO_2 doping curve has highest effective mode index 1.42 then it starts falling. Values of effective mode index are 1.3956, 1.3969, 1.4112 at 1.55 μm wavelength for without doping, 10% BaF_2 and 30% GeO_2 doping respectively.

After doping with both the materials effective mode index increases. There is significant change for GeO_2 30% doping than BaF_2 10% doping. Fig. 4.52 shows effective mode index vs wavelength for GeO_2 doped silica, BaF_2 doped silica and without doping.
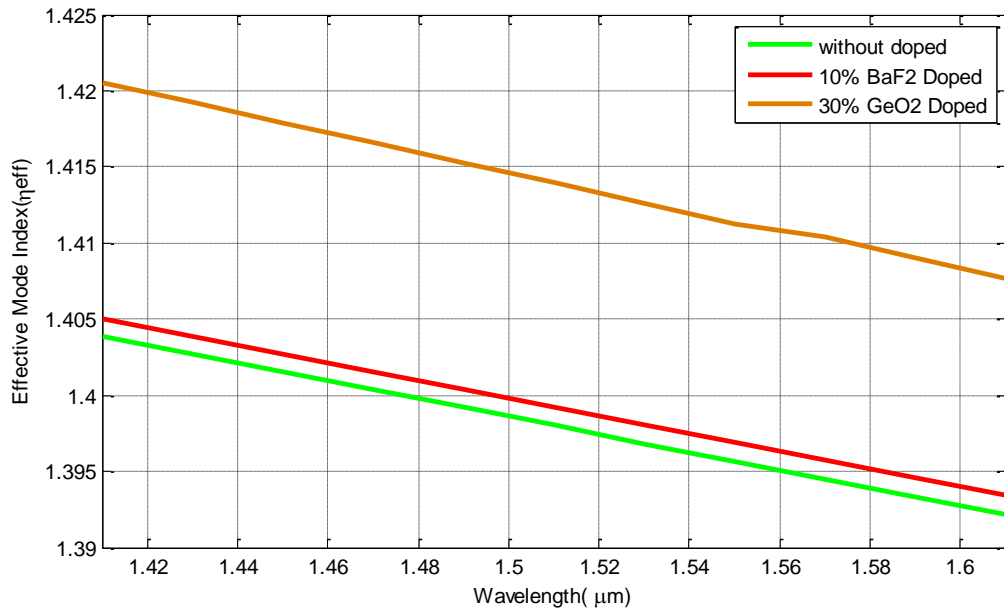
Fig. 4.52: Plot of Effective Mode Index against wavelength for 0% doing, 30% doping of GeO$_2$-SiO$_2$ and 10% doping of BaF$_2$-SiO$_2$ at pitch, Λ = 1.55 μm.

4.5.2 Comparison of Effective Mode Area Between Without Doping, GeO$_2$-SiO$_2$ and BaF$_2$-SiO$_2$ Doping

Effective mode area of GeO$_2$-SiO$_2$ 30% doping, BaF$_2$-SiO$_2$ 10% doping and 0% doping is compared and discussed below:
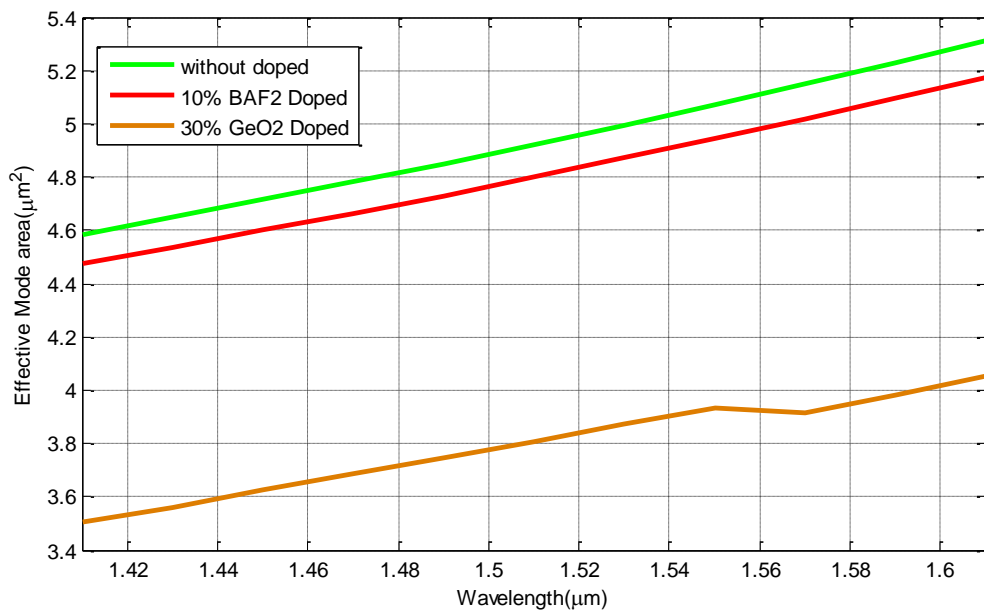
Fig. 4.53: Plot of Effective mode area vs wavelength for 0% doing, 30% doping of GeO$_2$-SiO$_2$ and 10% doping of BaF$_2$-SiO$_2$ at pitch, Λ = 1.55 μm

Fig. 4.53 shows effective mode area versus wavelength for 0% doping, 30% doping of GeO_2-SiO_2 and 10% doping of BaF_2-SiO_2. From curve it is seen that effective area decreases after doping. All curve shows same characteristic. With increasing wavelength effective area increases. Though after doping of H-PCF model effective area decreases, doping is suggested to minimize dispersion. Values of effective mode area are 5.0717 μm^2, 3.9357 μm^2, 4.9429 μm^2 at 1.55 μm wavelength for without doping, 10% BaF_2, 30% GeO_2 respectively. BaF_2-SiO_2 doping provides large effective mode area than GeO_2-SiO_2 doping.

4.5.3 Comparison of Dispersion Between Without, GeO₂-SiO₂ doping and BaF₂-SiO₂ doping

To compare between undoped, GeO_2-SiO_2 and BaF_2-SiO_2 model, dispersion is considered as the most important parameter. For GeO_2 30% doping and for BaF_2 10% doping dispersion is found more flattened and negative. Dispersion is considered as the most important parameter and all other parameters such as effective mode index, effective mode area, nonlinearity parameter is also compared on the basis of dispersion. At the time of without doping nonlinearity parameter can't be calculated. So, nonlinearity parameter for without doping is not included.
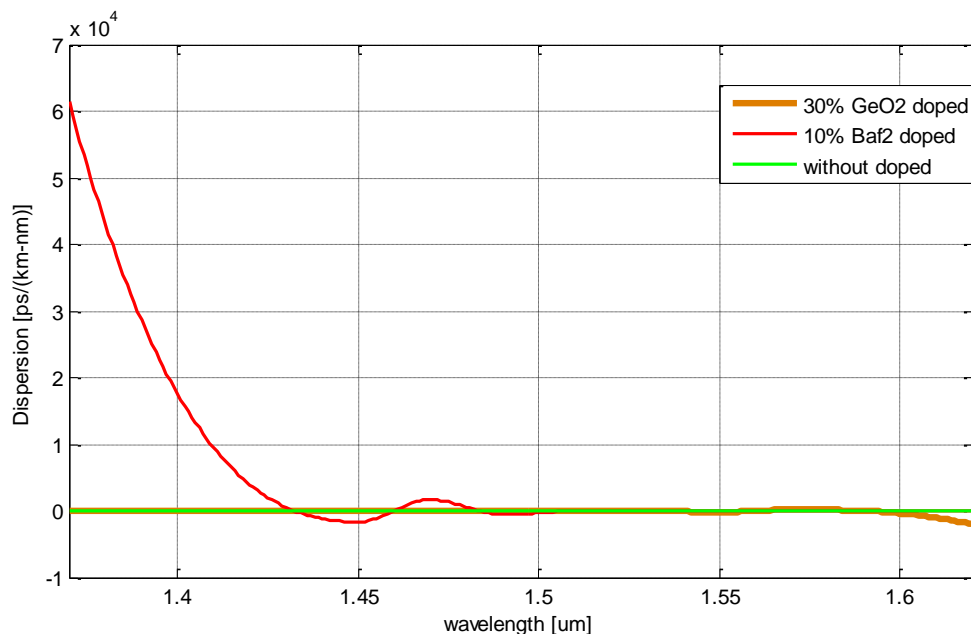
Fig. 4.54: Plot of Dispersion vs wavelength for 0% doing, 30% doping of GeO_2-SiO_2 and 10% doping of BaF_2-SiO_2 at pitch, $\Lambda = 1.55$ μm.

Fig. 4.54 shows dispersion against wavelength curve for 0% doing, 30% GeO_2-SiO_2 and 10% BaF_2-SiO_2 at pitch, $\Lambda = 1.55$ μm. From Fig. it is seen that 10% BaF_2-SiO_2 dispersion curve has high positive dispersion of 6.139×10^4 ps/(nm.km) at 1.37 μm wavelength. Positive dispersion is so high that for zero percentage doping and 30% GeO_2-SiO_2 plot seems almost flat. So, for more convenience illustrated curve of flattened region is shown separately.

From Fig. 4.55 it is seen that when the proposed model is not doped, it shows more dispersion. GeO_2-SiO_2 curve is almost zero and BaF_2-SiO_2 curve shows little dispersion. From Fig. 4.54 it is also noticed that 10% doping of BaF_2-SiO_2 has highest negative dispersion -1672 ps/(nm-km) at 1.45 μm wavelength. Flattened range is seen from 1.505 to 1.62 μm wavelength. At 1.575 μm wavelength almost zero dispersion of 0.02133 ps/(nm.km) is seen.

Again, 30% doping concentration of GeO_2-SiO_2 shows highest negative dispersion -1017 ps/(nm-km) which is at 1.61 μm wavelength. GeO_2-SiO_2 doping gives more flattened dispersion in a range of wavelengths starting from 1.371 μm to 1.533 μm wavelength and almost zero dispersion of 0.06035 ps/(nm.km) at 1.507 μm wavelength.
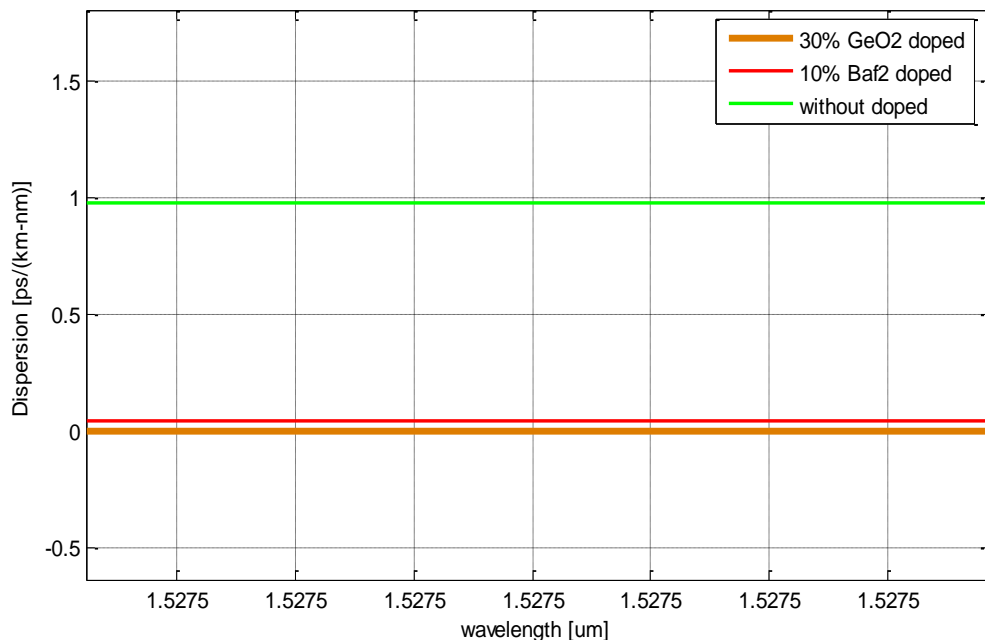
Fig. 4.55: Dispersion vs wavelength more illustrated curve for 0% doing, 30% doping of GeO_2-SiO_2 and 10% doping of BaF_2-SiO_2 at pitch, $\Lambda = 1.55$ μm.

4.5.4   Comparison of Nonlinearity Parameter Between GeO_2-SiO_2 and BaF_2-SiO_2 Doping

Nonlinearity parameter for GeO_2-SiO_2 and BaF_2-SiO_2 doping is studied separately. Comparison between nonlinearity for 30% doping of GeO_2-SiO_2 and 30% doping of BaF_2-SiO_2 is discussed briefly.

Fig. 4.56 shows nonlinearity parameter against wavelength curve for 30% doping of GeO_2-SiO_2 and 10% doping of BaF_2-SiO_2. It is noticed that with increasing wavelength nonlinearity parameter decreases but with increasing doping it decreases. From Fig. 4.56 it is again noticed that 10% doping of BaF_2-SiO_2 shows less nonlinearity then 30% doping of GeO_2-SiO_2. Again, 30% GeO_2-SiO_2 doping curve is not fully smooth. Value of nonlinearity parameter are 14.6797 and 18.3334 $W^{-1}Km^{-1}$ at 1.55 µm wavelength for 10% BaF_2, 30% GeO_2 respectively.
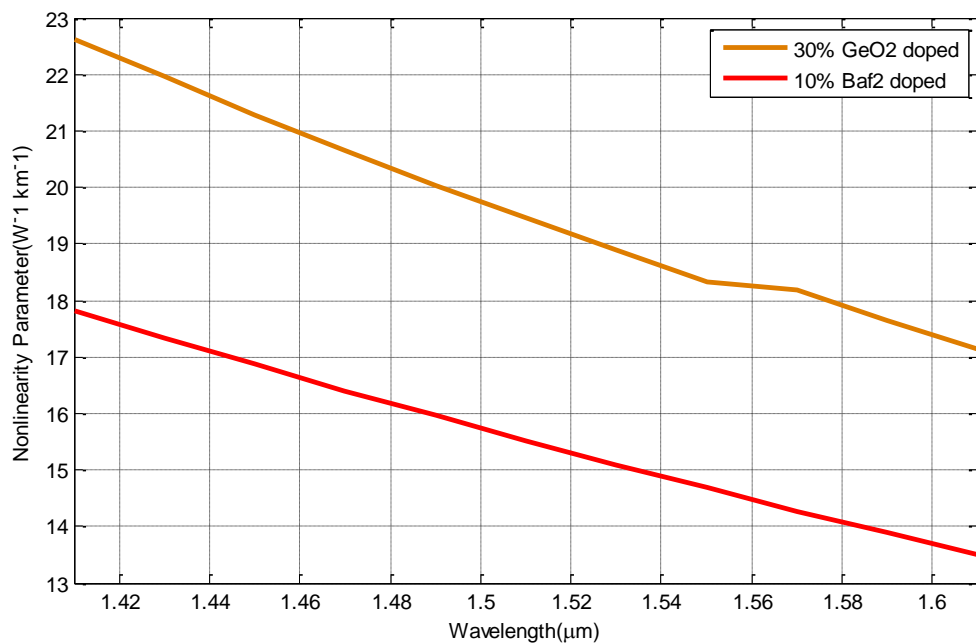
Fig. 4.56: Plot of Nonlinearity parameter vs wavelength for 30% doping of GeO_2-SiO_2 and 10% doping of BaF_2-SiO_2 at pitch, $\Lambda = 1.55$ µm.

4.6   Conclusion

In this chapter effective mode index, effective mode area, dispersion and nonlinear parameters are analyzed for the proposed H-PCF model for without doping, with GeO_2-SiO_2 doping and with BaF_2-SiO_2 doping. Comparison between without doping, GeO_2 doping and BaF_2 doping are also discussed.

CHAPTER 5

CONCLUSION AND FUTURE WORKS

5.1   Introduction

In this final chapter, we summarize the out-come of our intended research work to fulfill the desired objectives. Here, we also try to provide suggestions for future work.

5.2   Conclusion

The objectives of this thesis were to study structural properties of PCF to analyze and propose a suitable model, to compensate the dispersion by varying doping parameters of the core and to study other characteristics of the designed H-PCF over a broadband range. In light of these objectives, losses and characteristics of the proposed model are analyzed. From the simulation results and the plots, it can be assumed that the objectives are fulfilled.

30% doping of GeO_2 gives highest negative dispersion of -1017 ps/(nm.km) at 1.61 μm. A flattened range is seen from 1.371 μm to 1.533 μm wavelength and almost zero dispersion of 0.0635 ps/(nm.km) at 1.507 μm wavelength.

10% doping of BaF_2 gives highest negative dispersion of -1672 ps/(nm.km) at 1.45 μm wavelength. From 1.505 to 1.62 μm wavelength dispersion curve is almost flattened. In this range dispersion varies from -88.55 ps/(nm.km) to 5.672 ps/(nm.km). **BaF_2 doping in H-PCF is certainly a new approach.**

Both 10% BaF_2 doping and 30% GeO_2 doping shows high nonlinearity and suitable effective mode area.

Validating the obtained results with published works it is seen that 10% BaF_2 doping shows higher effective area than paper [9], slightly larger effective area than paper [11], high negative dispersion than paper [19, 20] providing flattened range from 1.505 to 1.62 μm wavelength.

When the model is undoped it gives better effective area than paper [13]. At 1.51 μm wavelength for 0% doping, 0.00 ps/(nm.km) dispersion is found. Comparing with [15], the

proposed model at 30% doping gives more flattened and zero dispersion and moderate nonlinearity than [9, 11].

So, it can be deducted from the above discussion that our proposed H-PCF for BaF_2 doped SiO_2 gives large effective area and zero flattened dispersion for broad range with suitable mode index and non-linear coefficient.

The proposed model shows very low dispersion for 0% doping or without doping but it doesn't provide any flattened range which is needed in most optical applications. That's why doping of H-PCF is suggested. After doping with GeO_2 and BaF_2 nearly zero flattened and high negative dispersion is found. Proposed model can be used to control chromatic dispersion and nonlinear optical applications. It is also seen from our proposed model that effective area decreases as doping percentage increases. This problem may be solved by increasing number of air hole rings of PCF. Dispersion is not constant for all doping percentage. So, experimenting other doping materials this problem may be solved.

5.3   Future Works

PCF has much application in fiber optic communications, fiber lasers, non-linear devices, high power transmission, highly sensitive gas sensors, and other areas. In this thesis paper, an insight of the characteristics of fiber is given which is desirable for fiber optic communication. More works on the related topic can be done in future by applying following guidelines:

(i)   Shape of the rings of air holes may be varied for each ring to confine the light beam further.

(ii)   Shape of the PCF may be changed to Octagonal, Decagonal and other Hybrid structure to minimize all other losses.

(iii)   Study of multi-core fiber can be taken to increase bandwidth and data rates of the transmission.

References

[1]   B.P.Lathi and Z.Ding, "Modern Digital and Analog Communication Systems", 4th Edition, New York Oxford,2010.

[2]   J.M.Senior, "Optical Fiber Communication, Principles and Practice", 3rd Edition, Pearson, 2009.

[3]   Gerd Keiser "Optical Fiber Communication Springer", 5th Edition, 2008.

[4]   M. Abrams, P.C. Becker, Y. Fujimoto, V. O'Byrne, and D. Piehler, "FTTP deployments in the United States and Japan-equipment choices and service provider imperatives", Light wave Technology, Journal of, 23(1):236-246, 2005.

[5]   W. A. Gambling, "The rise and rise of optical fibers", IEEE J. Sel. Top. Quantum Electron, 6(6), pp. 1084–1093, 2000.

[6]   T.A. Birks, J. C. Knight, and P. S. J. Russell, "Endlessly single-mode photonic crystal fiber," Optics Letters, vol. 22, no. 13, pp. 961–963, 1997.

[7]   R. Ramsay, "Photonic-crystal fiber characteristics benefit numerous applications", 17 November 2008, Society of Photo-Optical Instrumentation Engineers (SPIE) Newsroom. DOI: 10.1117/2.1200811.1371.

[8]   R. Buczynski, "Photonic Crystal Fibers", Proceedings of the XXXIII International School of Semiconducting Compound, vol. 106, no. 2, January 2004.

[9]   U.A. Siddika, M.S Rahman, "Design of an ultra-high nonlinear dispersion compensating Hybrid Hexagonal Photonic Crystal fiber'', 5th International Conference on Informatics, Electronics and Vision (ICIEV),2016.

[10]   M.I. Hasan, M. Selim Habib, M. Samiul Habib, S.M. Abdur Razzak, "Highly nonlinear and highly birefringent dispersion compensating photonic crystal fiber'', Optical Fiber Technology 20 (2014) 32–38.

[11]   M.S. Hossain, K.Neupane, M.S.B Hafiz, and S.P Majumder , "Dispersion and Nonlinear Characteristics of a Photonic Crystal Fiber (PCF) with Defected Core and Various Doping Concentration", 8th International Conference on Electrical and Computer Engineering, December-2014.

[12] K. Saitoh and M. Koshiba, T. Hasegawa and E. Sasaoka, "Chromatic dispersion control in photonic crystal fibers: application to ultra-flattened dispersion'', Optical Society of America, Vol. 11, No. 8 / Optics Express 843 (2003).

[13] M. Samiul Habib, M. Selim Habib, M.I. Hasan, S.M.A.Razzak, "A single mode ultra flat high negative residual dispersion compensating photonic crystal fiber" , Optical Fiber Technology (2014).

[14] S.Kabir, G.K.M Hasanuzzaman , M.A.G Khan, "Design of a Dispersion Flattened Germanium Doped Silica Modified Hexagonal Photonic Crystal Fiber with Ultra Low Confinement Losses" , International Conference on Electrical & Electronic Engineering (ICEEE), 2015 .

[15] R.R. Mahmud, S.M.A. Razzak, M.S. Salman, M.I. Hasan, "Design of a Photonic Crystal Fiber with Negative Flat Dispersion for Residual Dispersion Compensation", International Conference on Electrical & Electronic Engineering (ICEEE), 2015 .

[16] J. Mondal, M.S. Hossain and M.S. Rahman, "Analysis of Dispersion and Nonlinear Property in Doping Defected Core Spiral Photonic Crystal Fiber", British Journal of Applied Science & Technology, 19(2): 1-10, 2017; Article no. BJAST.31212, ISSN: 2231-0843, NLM ID: 101664541.

[17] M.A. Islam and M. S. Alam, "Design of a Polarization-Maintaining Equiangular Spiral Photonic Crystal Fiber for Residual Dispersion Compensation Over E+S+C+L+U Wavelength Bands", IEEE Photonics Technology Letters, VOL. 24, NO. 11, June 1, 2012.

[18] M.S. Habib, R. Ahmad, M. S Habib, and M. I. Hasan, "Residual dispersion compensation over the S+C+ L +U wavelength bands using highly birefringent octagonal photonic crystal fiber", Optical Society of America, Vol. 53, No. 14 / Applied Optics, May-2014.

[19] J.P. Silva, Diego S. Bezerra, V.F. Rodriguez-Esquerre, I.E da Fonseca, and Hugo E. Hernández-Figueroa, "Ge-Doped Defect-Core Micro Structured Fiber Design by Genetic Algorithm for Residual Dispersion Compensation", IEEE Photonics Technology Letters, VOL. 22, NO. 18, September 15, 2010

[20]   D.C. Tee, M. H. Abu Bakar, N. Tamchek and F. R. Mahamd Adikan, "Photonic Crystal Fiber in Photonic Crystal Fiber for Residual Dispersion Compensation Over E+S+C+L+U Wavelength Bands", IEEE Photonics Journal, Vol. 5, No. 3, June 2013.

[21]   C.C. Wang. M. H. Wang and J. WuA, "Heavily Germanium-Doped Silica Fiber with a Flat Normal Dispersion Profile", IEEE Photonics Society, Vol. 7, No. 2, April 2015.

[22]   M. Lucki, R. Zeleny, "Broadband submicron flattened dispersion compensating fiber with asymmetrical fluoride doped core", Society of Photo-Optical Instrumentation Engineers (SPIE), Vol. 8775, 87750M, doi: 10.1117/12.2017554 (2013).

[23]   S.Olyaee and F. Taghipour, "A new design of photonic crystal fiber with ultra-flattened dispersion to simultaneously minimize the dispersion and confinement loss", 3rd International Photonics & Opto Electronics Meetings (POEM 2010), doi:10.1088/1742-6596/276/1/012080.

APPENDIX 1

MATLAB CODES

Sample code for measuring Effective Mode Index

```
clc;
clearall;
closeall;

% wavelength
lam10=[1.41
       1.43
       1.45
       1.47
       1.49
       1.51
       1.53
       1.55
       1.57
       1.59
       1.61];

% effective mode index for GeO2 10% doping
Eta10=[1.403829
       1.40267
       1.401509
       1.400346
       1.399182
       1.398015
       1.396848
       1.395679
       1.39451
       1.39334
       1.39217];

plot(lam10,Eta10,'g');
xlabel('Wavelength( \mum)');
ylabel('Effective Mode Index(\etaeff)');
```

Sample code for measuring Effective Mode Area

```
clc;
clearall;
closeall;

% wavelength
lam10=[1.41
```

```
      1.43
      1.45
      1.47
      1.49
      1.51
      1.53
      1.55
      1.57
      1.59
      1.61];

% effective mode area for GeO₂ 10% doping

aeff=[4.165404163
      4.226602377
      4.289388432
      4.353820136
      4.419958145
      4.487866678
      4.557594627
      4.629210203
      4.702765213
      4.778312107
      4.855902628];
plot(lam10,aeff,'r');
xlabel('Wavelength(\mum)');
ylabel('Effective Mode Area Aeff(\mum^2)');
```

Sample code for measuring Dispersion Coefficient

```
%GeO₂ doped SiO₂H-PCF with doping concentration, X=0%
Eta10=[1.403829
      1.40267
      1.401509
      1.400346
      1.399182
      1.398015
      1.396848
      1.395679
      1.39451
      1.39334
      1.39217];
%GeO₂ doped SiO₂ H-PCF with doping concentration, X=10%
 Eta11=[1.409038
      1.407835
      1.406629
      1.40542
      1.404212
      1.403001
      1.401831
```

```matlab
            1.400574
            1.399359
            1.398144
            1.396928];
%GeO₂ doped SiO₂ H-PCF with doping concentration, X=50%
  Eta12=[1.433343
            1.433035
            1.430419
            1.428959
            1.427499
            1.42604
            1.424582
            1.423125
            1.421668
            1.420214
            1.419866];
%GeO₂ doped SiO₂ H-PCF with doping concentration, X=60%
  Eta13=[1.440196
            1.438651
            1.437108
            1.435568
            1.43403
            1.432494
            1.43096
            1.429428
            1.427898
            1.433262
            1.424845];
%GeO₂ doped SiO₂ H-PCF with doping concentration, X=40%
   Eta14=[1.426783
            1.426127
            1.42401
            1.422623
            1.421236
            1.419848
            1.4186
            1.417073
            1.415685
            1.414298
            1.412912];
%GeO₂ doped SiO₂ H-PCF with doping concentration,X=30%
    Eta15=[1.420534
            1.419216
            1.417897
            1.416577
            1.415256
            1.413933
            1.41261
            1.411287
            1.410353
            1.409027
            1.407701];
```

```matlab
ita=Eta10';
lamb=1.41:.02:1.61;
del=0.1;
%dd1(1)=(ita(1)-2*ita(end)+ita(end-1))/(del)^2;
for i=2:length(ita)-1
    dd1(i)=(ita(i-1)-2*ita(i)+ita(i+1))/(del)^2;
end

 dd1=dd1*10^12;
lambda=lamb(2:end-1);
dd=dd1(2:end);

for a=1:length(lambda)
dd(a)= -dd(a)*(lambda(a)/(3e8));
end
 lambda1=(1.37:.001:1.65);

ddd=interp1(lambda,dd,lambda1,'cubic');
plot(lambda1,ddd,'c');
xlabel('wavelength [um]');
ylabel('Dispersion [ps/(km-nm)]');
grid on
hold on
```

Sample code for measuring Nonlinear Coefficient

```matlab
clc;
clear all;
close all;
% wavelength
lam30=[1.41
       1.43
       1.45
       1.47
       1.49
       1.51
       1.53
       1.55
       1.57
       1.59
       1.61];

%nonlinearity for 10% GeO2 doping
  y2=[22.60858853
      18.50433387
      17.9819799
      17.47483436
      16.98229814
      16.50380153
      16.03886977
```

```
        15.58699106
        15.1477433
        14.72072666
        14.30556586];

plot(lam30,y2,'r');
xlabel('Wavelength(\mum)');
ylabel('Nonlinearity Parameter(W^-1 km^-1)');
```